MICROPOROUS COORDINATION POLYMERS:

EXPLORING HETEROGENEITY WITH AN ANTIMATTER PROBE

by

Jeremy Ian Feldblyum

A dissertation submitted in partial fulfillment
of the requirements for the degree of
Doctor of Philosophy
(Macromolecular Science and Engineering)
in The University of Michigan
2013

Doctoral Committee:

   Professor Adam J. Matzger, Chair
   Professor David W. Gidley
   Associate Professor Anne J. McNeil
   Assistant Professor Stephen Maldonado

"It's life that matters, nothing but life – the process of discovering, the everlasting and perpetual process, not the discovery itself, at all."

– F. Dostoevsky

Acknowledgements

I would first like to thank my mentor throughout my time at the University of Michigan, Professor Adam J. Matzger (colloquially, "Matzger"). Whatever success I attained during graduate school is in large part simply a reflection of Matzger's always keeping a few steps ahead of me, ready with an answer whenever I had a question. There aren't words for the gratitude I have; my future accomplishments, whether many or few, are my way of saying thanks to an incomparable mentor.

Professor David W. Gidley served as a mentor to me as well, giving me an introduction to positron annihilation lifetime spectroscopy and even letting me try my hand at it myself. He was always available and ready to talk for far longer than his schedule probably allowed, and through our many conversations I've come away with at least a glimpse of the way a physicist thinks. Finally, without Prof. Gidley, I would not have been able to put "antimatter" in my talk and poster titles, a word that undoubtedly doubled and tripled the audiences I attracted on those occasions.

While she may not remember it, Professor Anne J. McNeil was the first professor to give me her own perspective on what being a professor entails, discussing what it was like to start out at Michigan while on our way back to the chemistry building from North campus. I am grateful for her constant willingness to share her thoughts and experiences. In addition, her incredible thoroughness as a teacher and as an advisor is something that I will spend my life striving to achieve.

Professor Stephen Maldonado stuck with a project that I at many turns had little hope for. I learned a great deal from his perseverance and ability to focus on the silver lining, and with his guidance, was able to publish what turned out to be a detailed and conclusive study on a subset of materials that had up to that point been the subject of a great deal of conflicting research.

And for my family. To you I owe the most. You taught me to be me.

Table of Contents

List of Figures

Abstract

Microporous coordination polymers (MCPs) are a rapidly growing class of porous, crystalline materials derived from alternating organic and inorganic building blocks. While some MCPs exhibit exceptional sorption properties, many others do not show the performance expected based on their crystallographic models. Realizing the full potential of these materials requires a thorough understanding of why many fall short of such expectation. Obtaining such insight is hampered by a lack of methods to examine localized defects and heterogeneity within these materials. This dissertation focuses on the use of positron annihilation lifetime spectroscopy (PALS) to elucidate the reasons for low porosity in two well-known MCPs, Zn-HKUST-1 ($Zn_2(btc)_3$, btc = 1,3,5-benzene tricarboxylate) and IRMOF-8 ($Zn_4O(ndc)_3$, ndc = 2,6-naphthalene dicarboxylate). PALS is used to show that while the Zn-HKUST-1 interior contains empty pores of diameter commensurate with the corresponding crystallographic model, the pores near the surface of Zn-HKUST-1 are inaccessible, thereby precluding access to the porous interior. The porosity of the material before solvent removal is confirmed by the facile diffusion of solution-phase guest species into the crystal interior. IRMOF-8, despite having been first reported more than a decade ago, has until now shown surface areas at best only half of that expected based on its crystallographic model. A combination of PXRD, gas sorption, and PALS are used to show that typical preparations of IRMOF-8 in fact produce an interpenetrated analogue. A route to synthesize and activate non-interpenetrated IRMOF-8 is developed. The material has high gravimetric adsorption capacities for gaseous fuels such as hydrogen and methane; however, *in situ* PALS reveals that even at high pressures, only monolayer sorption is achievable with light gases above their critical temperatures. Hence, to maximize *volumetric* adsorption, linker functionalization is necessary. The use of PALS to analyze MCPs also resulted in the serendipitous discovery that positronium assumes a quantum mechanical Bloch state in highly ordered and porous

MCPs such as IRMOF-1 (Zn$_4$O(bdc)$_3$, bdc = 1,4-benzene dicarboxylate) and non-interpenetrated IRMOF-8.

Chapter 1

Porous Materials: Their Properties and Characterization

1.1   Charcoal and Activated Carbon

Porous carbonaceous materials have existed since fire first came into contact with organic matter. The result of such a union, charcoal, is a material having pores (internal voids) of sizes ranging from mm all the way down to sub-nm length scales, depending on the nature and conditions of the combustion of the precursor material(s).[1] The first recorded uses of charcoal as an adsorbent date back as early as ~1500 B.C.E.,[2] where the material was used in Egypt for drying wounds. Medicinal uses for charcoal were also recorded by Greek and Roman physicians,[2] and its uses for water purification and preservation were known to both Western and Eastern civilizations of the time.[2]

As an industrial sorbent, the first uses of porous carbon were described by Lowitz in the late 1700s. These uses included tartaric acid purification and as a decolorizing agent during sugar refining.[2-4] Around the same time, researchers were beginning to take interest in the properties of charcoal as a gas sorbent. Fontana[5] and Scheele[6] independently reported the reversible uptake of large volumes of gas by charcoal, suggesting that high *internal* space was available to store gas within the exterior of individual grains. Not long after, in the early 1800s, emphasis on the importance of surface area and porosity was introduced by de Saussure[7] and Mitscherlich,[8] respectively. By the beginning of the 20th century, activated carbon (the term for charcoal produced to maximize pore accessibility, volume, and surface area) was in widespread use for industrial applications.[2,9-12]

1

High surface area carbons are obtained through a variety of means to obtain a sorbent with the desired properties. Typically, a precursor carbon source is treated with acid or base and pyrolyzed at ~700-1000 °C. These materials can come from sources as diverse as peach pits[13] and coconut shells[14] to coal or petroleum coke.[15] Current industrial applications for these materials include water[16] and gas[17] purification, catalyst supports,[18] and medical adsorbents.[19] They are also being studied for potential use in adsorption-based fuel storage and delivery.[20]

1.2   Zeolites, Silica, and Alumina

Historically, porous metal oxides were the only known sorbent alternatives to activated carbon. Zeolites (**Figure 1.1**), crystalline, porous metal oxides composed of aluminum, silicon, oxygen, and other cations typically from groups 1A and 2A, occur naturally; however, their study only began in earnest near the end of the 1700s.[21,22] The reversible water uptake properties of these materials were recognized by Damour in 1857;[23] the following year saw the first report on the synthesis of a zeolite.[24] Commercialization of zeolites came at the beginning of the 1900s, when their utility in removing divalent cations from water was described by Gans.[25] However, zeolites did not enjoy widespread attention in the scientific community until the pioneering work of Richard Barrer,[21] who developed hydrothermal synthesis techniques for a number of naturally occurring[26] and previously unknown[27] zeolites. The field matured rapidly during the subsequent decades, with a number of both industrial[28-30] and academic[31,32] researchers expanding upon earlier work to synthesize many new zeolites. This influx of new materials led to the expansion of the capabilities of zeolites in separation science. Zeolites are widely used in industry today, especially for catalysis, ion exchange, and both gas and liquid phase separations.[33]

Silica gel, a porous form of SiO_2, was known as early as 1640, although it was not commercialized[34] until World War I where it was used as an adsorbent in gas masks.[35] The use for silica as sorbent for chromatography (perhaps its most notable use in laboratories today) dates back to the early 1940s;[36] the speed and efficiency with which

such separations could be carried out popularized silica rapidly. Currently, silica finds uses for applications of a variety of complexities, from air drying[37] to ultra high-performance liquid chromatography.[38]

The history of alumina dates back to Roman times, and knowledge of its composition began to grow in the early 1700s.[39] It is possible that alumina was used as a sorbent well before the 20th century (reliable documentation appears lacking); it is certain that by the early 1900s, a number of preparations of alumina were known to yield porous material.[40-42] In the earlier half of the 1900s, activated alumina was used for laboratory-scale chromatography and as a desiccant ("activated" here refers to the process of rendering pores empty and accessible to molecular guests).[43] Large-scale separations using activated alumina gained popularity in the latter half of the 20th century; its use as a heterogeneous catalyst support is also now widespread.[37]

1.3   Microporous Coordination Polymers

Until 1989, microporous materials consisted primarily of carbons, zeolites, silica, and alumina. In that year, Hoskins and Robson published their seminal communication enumerating the defining concepts of what would soon become the field[44] of microporous coordination polymers (MCPs). They hypothesized that by using the rigid, tetrahedral, tetratopic ligand 4,4′,4′′,4′′′-tetracyanotetraphenylmethane and the tetrahedrally coordinating cation Cu^+, a coordination polymer with a diamondoid network could be formed (Figure 1.2). Slow evaporation of a solution containing the appropriate precursors indeed led to crystals of the expected structure. This approach was demonstrated over the next few years to be applicable to numerous materials, and many other research groups began examining MCPs and expanding the chemistries available for their synthesis. Accessible porosity and maintenance of crystallinity in these materials after guest removal was demonstrated by Rosseinsky,[45] Kitagawa,[46] and Mori[47] (it should also be noted that the Prussian blue and analogues were shown to maintain structural integrity after guest removal many years earlier[48]). In 1999, separate reports by Yaghi[49] and Williams[50] demonstrated that activated MCPs could exhibit surface areas on par with

those typically observed in only zeolites and activated carbons. The materials in these papers, MOF-5 ($Zn_4O(bdc)_3$, bdc = 1,4-benzene dicarboxylate) and HKUST-1 ($Cu_3(btc)_2$, btc = 1,3,5-benzene tricarboxylate) were both constructed using rigid carboxylate ligands connecting metal clusters; the use of anionic ligands coupled to cationic clusters imparted robustness towards guest removal, and the chosen linker/metal cluster combinations allowed formation of 3-dimensional frameworks with large void fractions. After the publication of MOF-5 and HKUST-1, the field of coordination polymers gained a tremendous amount of popularity due to the versatility of these materials for applications as diverse as gas sorption[51] and separation,[52] catalysis,[53] and non-linear optics[54].

1.4   Characterization of Microporous Coordination Polymers by X-ray Diffraction and Gas Sorption Methods

By far the two most widely used techniques for assessing the characteristics and quality of synthesized MCPs are X-ray diffraction (both powder and single crystal methods) and gas sorption analysis. Since MCPs are crystalline materials, obtaining a crystal structure model (typically via single crystal X-ray diffraction, SXRD) and then comparing bulk powder X-ray diffraction (PXRD) data to PXRD data simulated from the single crystal structural model provides strong evidence for the bulk atomic arrangement of the material being analyzed. Using computational methods (vide infra), a theoretical surface area can then be obtained from the (guest-free) structural model. The theoretical surface area is compared with that estimated from gas sorption. Gas sorption analysis is then used to obtain an experimental surface area via the BET method (see below), which is finally compared with the expected theoretical surface area to verify that the material's pores are empty and accessible. This is the typical workflow used to analyze new MCPs. In cases where single crystals are easily obtained and the MCP can be fully activated without altering or eliminating structural order, PXRD and gas sorption data can lend confidence to the correspondence between crystallographic models and experimentally obtained materials.

Single crystals of MCPs are most commonly obtained through solvothermal techniques. Screening synthesis conditions (temperature, solvent, pH, concentration, etc.) can lead to crystals of quality high enough for reliable structure solution. Solvent diffusion or solvent evaporation are also used, although these were more commonly employed in the earlier stages of the field, before solvothermal methods came into common use. In many cases, however, single crystals are not easily obtained. In cases where a hypothetical structure can be modeled based on precursor components, Rietveld refinement can be used to quantify agreement between experimental PXRD patterns and PXRD simulated from hypothetical structures. Good agreement lends confidence to the proposed structural model. Further solid-state analysis (thermogravimetric analysis, elemental analysis, IR spectroscopy, Raman spectroscopy, solid-state NMR spectroscopy, etc.) can be used to corroborate the proposed structural model. In the case where a structural model is not easily predicted based purely on linker and cluster geometry, more sophisticated methods are required. Férey and coworkers developed an approach[55] coined the "Automated Assembly of Secondary Building Units" (AASBU) whereby geometrically defined building blocks are assembled *in silico* to form energy-minimized extended framework structures. The first example of this method applied to MCPs was demonstrated in 2004, where the compound MIL-100 ($Cr_3F(H_2O)_3(btc)_2$, Figure 1.3), having a cubic unit cell dimension of ~7 nm, was obtainable only as a microcrystalline powder.[56] Three candidate structures were obtained computationally using the AASBU approach, and subsequent Rietveld refinement of the experimental PXRD pattern against the computational models was used to determine the correct structure for the material. It should be emphasized that a synchrotron X-ray source was used to obtain PXRD data; an intense X-ray source is often a prerequisite to accurately obtaining a crystallographic model using PXRD data.

Ab initio structure solution from PXRD data using synchrotron-based X-ray sources has been reported in a few instances for MCPs. Routes to solving structures from PXRD data include the maximum-entropy method,[57] simulated annealing,[58-60] a direct-space genetic algorithm,[61] and others.[62,63] Notably, a laboratory X-ray source was recently used to solve the structures of triazolate-based MCPs using the charge-flipping method.[64]

Gas sorption as a structural characterization technique is used to demonstrate accessible porosity and can further quantify surface area, pore volume, and pore size distribution. Given a crystallographic model, a theoretical surface area can be calculated based on the Connolly[65] or geometric accessible methods. The geometric accessible surface area[66] is generally preferred, as it accounts for the differences in accessibility between concave and convex surfaces. A surface area obtained by gas sorption methods can then be compared with the theoretical surface area; good agreement supports the accuracy of the crystallographic model used to obtain the theoretical surface area. To obtain an experimental surface area, solvent and other volatile molecular guests must first be removed from the sample. The sample is typically prepared by subjecting it to reduced pressure, or more recently, supercritical CO_2,[67] a process termed "activation." During activation under reduced pressure, capillary forces of the evaporating occluded solvent are thought to be responsible for pore collapse.[67] In supercritical CO_2 activation, occluded solvent in an MCP is replaced by liquid CO_2 at room temperature and subsequently heated beyond the critical temperature (31°C for CO_2). Pressure is then slowly reduced, inducing the supercritical fluid-gas phase transition. As supercritical fluids lack surface tension, capillary forces are avoided as CO_2 leaves the MCP, reducing the chances of pore collapse on guest removal. While supercritical CO_2 activation has been necessary to reveal accessible porosity in the highest surface area MCPs known,[68] it must be emphasized that a molecular level understanding of activation (whether via reduced pressure, supercritical CO_2, or otherwise) in these materials is currently unknown, especially for materials of pore diameter only a few guest molecules wide. Nitrogen sorption isotherms obtained from activated materials at 77 K are typically used to obtain experimental surface area values. Nitrogen gas is a weakly-interacting gas such that only physisorption (no chemisorption) is expected to occur with the adsorbent. Surface areas are obtained using the BET method,[69] a model that calculates surface area based on the number of molecules of known diameter adsorbed to a surface (the number of adsorbed molecules is derived from nitrogen isotherm data). The BET method accounts for multilayer adsorption. The applicability of the BET method in surface area analysis of MCPs was explored extensively by Snurr and co-workers,[70] who determined that by careful choice of the pressure range used to apply the BET method, good agreement

6

between theoretical[66] and experimental surface area values can be obtained. The use of the Langmuir method of surface area determination for MCPs is not uncommon, but should be avoided, as it is very well known to overestimate surface area due to the unfounded and typically inaccurate assumption that adsorption occurs in just one monolayer.[71]

Pore volumes are calculated from nitrogen isotherms obtained at 77 K as well. Given the assumption that nitrogen packs in pores as a condensed (liquid) phase, the uptake at pressures near the saturation vapor pressure (in cm^3/g) is first converted to moles by the ideal gas law, and then multiplied by the molar volume of liquid nitrogen (34.7 cm^3/mol) to obtain the volume of the pores in which (presumably) condensed nitrogen resides.

While numerous mathematical methods for determining pore size distributions (PSDs) are available, including the Horvath-Kawazoe,[72] Dubinin-Radushkevich,[73] and Dubinin-Astakhov[74] methods, non-local density functional theory (NLDFT) fitting of experimental isotherms can show excellent agreement between PSDs obtained from experimental data and crystallographic models. NLDFT requires kernels for the adsorbate-adsorbent combination of interest; kernels for specific MCPs are currently unavailable, but assuming zeolite-like properties still leads to data in good agreement with crystallographic models in most cases. NLDFT models for fitting Ar isotherms obtained at 87 K are readily available; for this reason, researchers in the field often obtain PSDs from Ar isotherms.

1.5   Disorder and Defects in Crystalline Porous Materials

While X-ray diffraction and gas sorption are the most commonly employed techniques used for analyzing crystalline porous materials, they do present significant limitations in examining disorder and defects in these materials. X-ray diffraction provides only space-averaged structural information, and is generally not well-suited to elucidating structural disorder. Hence, crystalline domains in an otherwise amorphous material will contribute significantly to the X-ray diffraction pattern, potentially misleading the researcher into believing the entire material is crystalline. If the material

possesses local defects despite bulk crystallinity, these defects will go undetected by X-ray diffraction. Gas sorption suffers similar drawbacks. Furthermore, the presence of occluded guests or isolated pores can lead to observation of an apparently reduced or a complete lack of porosity. While limited porosity by gas adsorption can be used to infer pore collapse, interpenetration, or the presence of occluded guests, none of these phenomena can be addressed directly by gas sorption alone. In these cases, complementary techniques such as solid-state NMR spectroscopy, Raman spectroscopy, etc. are needed to elucidate the cause of low surface area.

Although the vast majority of the MCP literature deals solely with the synthesis and functionality of new materials, a small number of groups have turned their attention to examining non-ideal behavior in MCPs – that is, those occasions where a material simply does not behave as the crystallographic model might suggest. Single crystal X-ray diffraction was used to detect both interpenetration and occluded $Zn(OH)_2$ in MOF-5 synthesized by rapid precipitation methods.[75] This study was especially important at the time because many research groups were synthesizing a material claimed to be MOF-5 that possessed BET surface areas around 1000 m^2/g or less. The detection of interpenetration and occluded guests in these materials accounts for the data observed in many previous studies, and clearly demonstrated the effects of utilizing synthetic protocols not optimized to achieve the maximum possible surface area. X-ray scattering was used in a subsequent paper to characterize such impure MOF-5 further.[76] The pore structure of the material examined by SAXS suggested a micropore structure less ordered than that which would be expected for a pure material. Furthermore, mesopores of ~3 nm diameter were detected.

Other approaches to examine pore structure and highlight defects in MCPs have involved the tracking of guest molecules in these materials. Gas permeation measurements employing interference and infrared microscopy were used to show that the surface of an otherwise porous MCP, Zn(tbip) (tbip = 5-*tert*-butyl isophthalate), is almost completely blocked.[77,78] Gas diffusion into the pores of this material occurs through only a small number of open sites at the surface. Fluorescent guests have also lent insight into the pore structure of MCPs. Single-molecule fluorescence microscopy was performed on UMCM-1 ($Zn_4O(bdc)(btb)_{4/3}$, btb = 1,3,5-benzene tribenzoate),

UMCM-2, $(Zn_4O(t^2dc)(btb)_{4/3}$, t^2dc = thieno[3,2-*bis*]thiophene-2,5-dicarboxylate) and UMCM-4 $(Zn4O(bdc)(tpa)$, tpa = 4,4′,4″-tricarboxytriphenylamine) using Nile Red as the fluorescent guest. While the ensemble diffusion characteristics of Nile Red in these materials followed those expected based on the pore structures of these materials (confined, 1D, or 2D diffusion), individual molecules showed behavior inconsistent with that expected from ideal crystallographic models. Defects sites appeared to arrest the motion of Nile Red in some cases, while in other cases, open defects seem to allow facile diffusion over large distances.[79] In a study by Ameloot et al.,[80] furfuryl alcohol (FFA) was used as a probe to detect free acidic sites in HKUST-1, MOF-5, and MIL-53(Ga) (Figure 1.4). FFA polymerizes in the presence of an acid. Poly(FFA) is fluorescent, so defect sites could be spatially resolved within single crystals. Furthermore, α-pinene was used to distinguish between Lewis vs. Brønstead acid sites.

An XPS and computational study of HKUST-1 grown as a multilayer film showed that the film possessed both Cu^{2+} and Cu^+. This suggested the presence of both tetracarboxylate and tricarboxylate paddlewheel clusters, despite a PXRD pattern that indicated phase-pure HKUST-1, which should have only tetracarboxylate clusters.

Finally, AFM has been used to analyze microscopic defects such as dislocation growth spirals in a number of MCPs including MOF-5,[81] HKUST-1,[82] and ZIF-8.[83]

1.6   Positron annihilation lifetime spectroscopy

Positron annihilation lifetime spectroscopy (PALS) is a technique operating on the principle that positronium (Ps), the bound state of an electron and a positron, spontaneously annihilates in an amount of time depending on the size of the void space in which it annihilates.[84,85] In PALS, a radioactive positron source (typically a salt containing ^{22}Na) is placed near the material being analyzed. On the emission of a positron, a 1270 keV γ-ray is emitted concomitantly and serves as the "start" signal. Emitted positrons assume an energy distribution between 0 and 511 keV and hence are implanted with a depth of ~0.5-1 mm. Positrons lose energy through inelastic, ionizing collisions with electrons in the target material, eventually losing enough energy to bind to one of these ionized electrons to form Ps. Positrons can also annihilate directly with

electrons, a process generally occurring within a few hundred picoseconds after positron emission. Formed Ps can take on parallel (*ortho*) or antiparallel (*para*) spins. The *para* species (*p*-Ps) has a lifetime in vacuum of 0.125 ns while the *ortho* species (*o*-Ps) has a longer lifetime in vacuum of 142 ns. The longer-lived species diffuses throughout the porous material, annihilating more rapidly in smaller pores. Annihilation yields γ-rays of energies at or below 511 keV; these photons provide the "stop" signal. The Ps lifetime is then the difference between the start and stop γ quanta, the average lifetime being determined from an exponential decay fitted to a histogram built from ~10^5-10^7 annihilation events. The size of the pore in which *o*-Ps annihilates can be determined from the average lifetime(s) of *o*-Ps annihilation in a sample using an extended Tau-Eldrup model.[86-89]

PALS holds a number of advantages over more traditional porosimetry techniques. First, PALS can provide information on buried or otherwise inaccessible pores. For non-interconnected pores, PALS provides lifetimes reflecting local pore structure. PALS depth-profiling, a technique where positrons are implanted at controlled energies (typically in the 0.1-10 keV range), allows probing the pore structure as a function of depth from the material's surface with nanometer resolution.[90] These characteristics make PALS ideally suited to examining disorder and defects in MCPs where methods such as X-ray diffraction and gas sorption fall short.

Prior to the work described in this dissertation, our group published the first paper using PALS to examine an MCP.[91] We examined MOF-5 during thermal degradation and CO_2 adsorption, proving the utility of PALS for *in situ*, time-resolved measurements of porous materials.

1.7   Organization of Thesis

This thesis focuses on the use of PALS to examine MCPs. In Chapter 2,[92] the study of a long-known but little-studied MCP Zn-HKUST-1 ($Zn_3(btc)_2$) is described. Zn-HKUST-1 is a material isostructural to Cu-HKUST-1. However, despite retention of bulk crystallinity after activation, Zn-HKUST-1 exhibits no measurable porosity by gas

adsorption. PALS reveals that, while the interior pores of Zn-HKUST-1 are empty, the surface of the material is collapsed, prohibiting the entry of molecular guests. Chapter 3 describes the discovery that IRMOF-8 ($Zn_4O(ndc)_3$, ndc = 2,6-naphthalene dicarboxylate), which typically exhibits BET surface areas between 1000-2000 m^2/g, can be synthesized and activated in a manner to maximize its surface area.[93] A surface area of 4400 m^2/g was achieved, a result made possible using activation by our recently developed flowing supercritical CO_2 system.[94] Following this work, Chapter 4 describes in detail the cause for low surface area in solvothermally synthesized IRMOF-8.[95] Interpenetration occurs in this material when synthesized at elevated temperatures (>70 °C), as revealed by a combination of PALS and PXRD analysis. PALS is then used to examine methane uptake in high surface area IRMOF-8 *in situ*. Surprisingly, monolayer sorption seems to be operative at room temperature irrespective of pressure, suggesting that above the critical temperature, a gas will only adsorb in an MCP in a single monolayer.

Our studies of heterogeneity and defect structure in MCPs also led to the remarkable discovery that *o*-Ps in an MCP assumes a delocalized Bloch state, allowing *o*-Ps to travel hundreds of times greater distances in MCP channels than would be expected for a classical particle.[96] These results are detailed in Appendix A.

Chapter 5 concludes the thesis with a perspective on the consequences of this work and the developments stemming from it that are hoped to follow.

1.8   Figures
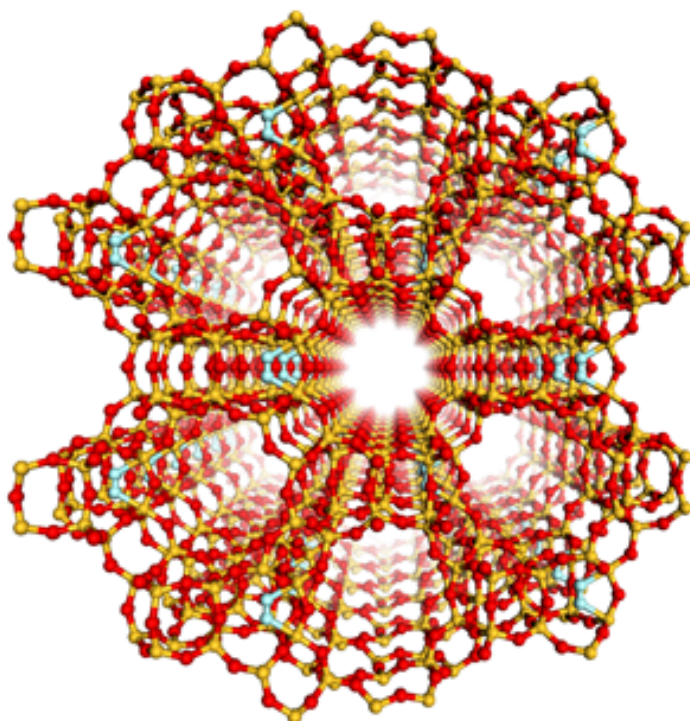
Figure 1.1. Example structure of a zeolite (IFT zeolite from ref. 95)
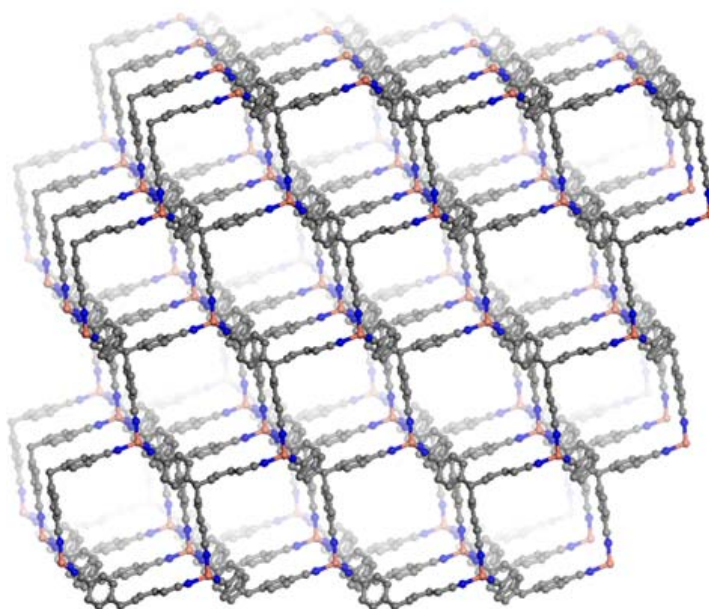
Figure   1.2.   Structure   of   Cu(4,4′,4′′,4′′′-tetracyanotetraphenylmethane)BF$_4$ discovered by Hoskins and Robson.[96]
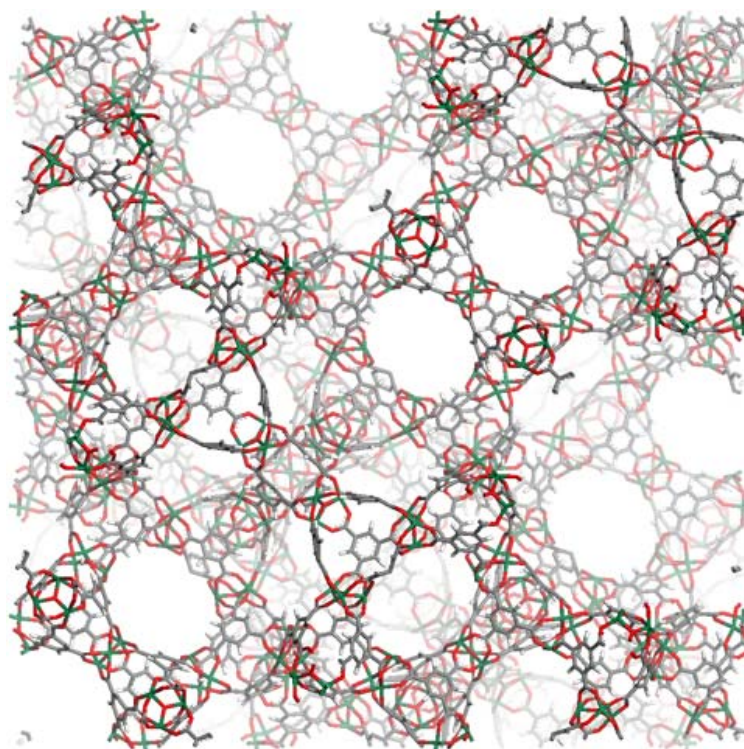
Figure 1.3. Structure of MIL-100 $(Cr_3F(H_2O)_3(btc)_2)$[56] as determined by PXRD and computational methods.
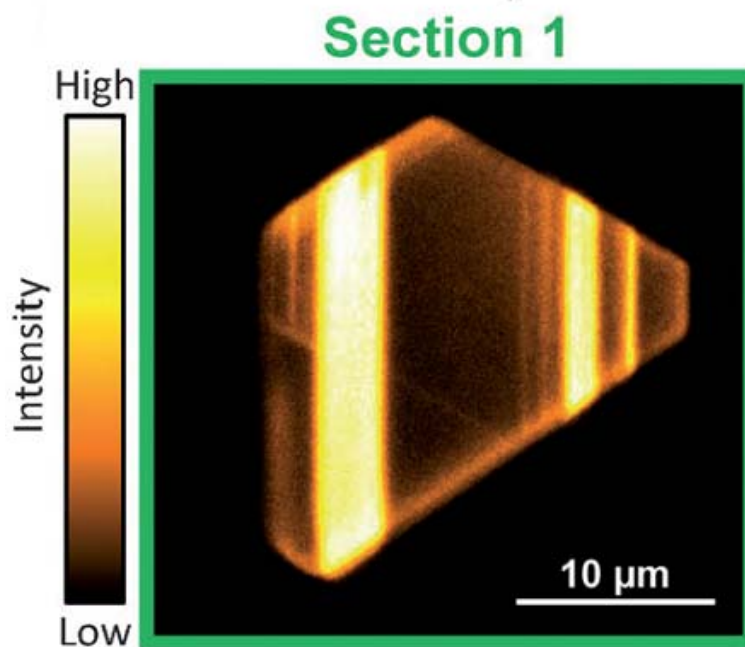
Figure 1.4. Defect structure in HKUST-1 revealed by fluorescence microscopy. Reproduced with permission from ref. 80.

1.9   References

(1)   Ioannidou, O.; Zabaniotou, A. *Renewable and Sustainable Energy Reviews* **2007**, *11*, 1966.

(2)   Robens, E. *Chem. Ing. Tech.* **2010**, *82*, 763.

(3)   Lowitz, J. T. *Crell's Chemische Annalen* **1788**, 36.

(4)   Lowitz, J. T. *Crell's Chemische Annalen* **1786**, *1*, 679.

(5)   Fontana, F. *Memorie di Matematica e Fisica della Società Italiana* **1777**, *1*, 679.

(6)   Scheele, C. W. *Chemical Observations and Experiments on Air and Fire* Uppsala and Leipzig, 1780.

(7)   Saussure, N.-T. d. *Gilbert's Ann. Phys.* **1814**, *47*, 113.

(8)   Mitscherlich, E. *Pogg. Ann.* **1843**, *59*, 94.

(9)   McKeever, E. A. Recovery of Spirit from Spent Charcoal of Rectifying Filters. United States of America Patent 194,256, August 14, 1877.

(10)   Knöpflmacher, A. Process for Producing a Highly-Active Decolorizing Carbon. United States of America Patent 1,358,162, November 9, 1920.

(11)   Baggaley, R. Method of Arresting Arsenic Fumes. United States of America Patent 746,251, December 8, 1903.

(12)   Somes, D. E. Improved Mode of Securing Pure and Wholesome Air in Dwellings. United States of America Patent 44,671, October 11, 1864.

(13)   Molina-Sabio, M.; RodRíguez-Reinoso, F.; Caturla, F.; Sellés, M. J. *Carbon* **1995**, *33*, 1105.

(14)   Laine, J.; Calafat, A.; Labady, M. *Carbon* **1989**, *27*, 191.

(15)   O'Grady, T. M.; Wennerberg, A. N. Active carbon process and composition. United States of America Patent 4,082,694, April 4, 1978.

(16)   Ahmedna, M.; Marshall, W. E.; Husseiny, A. A.; Rao, R. M.; Goktepe, I. *Water Res.* **2004**, *38*, 1062.

(17)   Sircar, S.; Golden, T. C.; Rao, M. B. *Carbon* **1996**, *34*, 1.

(18)   Joo, S. H.; Choi, S. J.; Oh, I.; Kwak, J.; Liu, Z.; Terasaki, O.; Ryoo, R. *Nature* **2001**, *412*, 169.

(19)   Bond, G. R. *Ann. Emerg. Med.* **2002**, *39*, 273.

(20)   Voskuilen, T. G.; Pourpoint, T. L.; Dailly, A. M. *Adsorption* **2012**, *18*, 239.

(21)   Masters, A. F.; Maschmeyer, T. *Microporous Mesoporous Mater.* **2011**, *142*, 423.

(22)   A.F. Cronstedt, An Essay Toward a System of Mineralogy (Gustave von Engestrom, Trans.), second ed., Charles Dilly and Sons, London, 1788 (Original work published in Additions of Modern Discoveries by John Hyacinth de Magellan)

(23)   The citation for this article is given in ref. 21 as "Damour, A. *Ann. Mines* **1840**, *17*, 191." However, the text in ref. 21 describes the discovery of reversible water uptake in a zeolite as having occurred in 1857, seventeen years after the reference

provided. While Damour published in *Annales des Mines* throughout the 1840's and 1850's, access to individual articles is currently unavailable, so the date of Damour's discovery cannot be independently confirmed.

(24)   Eichorn, H. *Ann. Phys. Chem.* **1858**, *105*, 126.

(25)   Gans, R. *Jahrb. Preuss. Geol. Landesanstalt* **1905**, *26*, 179.

(26)   Barrer, R. M. *J. Chem. Soc.* **1948**, 2158.

(27)   Barrer, R. M. *J. Chem. Soc.* **1948**, 127.

(28)   Milton, R. M. Crystalline Zeolite F. United States of America Patent 2,996,358, August 15, 1961.

(29)   Breck, D. W. Crystalline Zeolite Q. United States of America Patent 2,991,151, July 4, 1961.

(30)   Breck, D. W.; Acara, N. A. Crystalline Zeolite M. United States of America Patent 2,995,423,

(31)   Kerr, G. T.; Kokotailo, G. T. *J. Am. Chem. Soc.* **1961**, *83*, 4675.

(32)   Eulenberger, G. R.; Shoemaker, D. P.; Keil, J. G. *The Journal of Physical Chemistry* **1967**, *71*, 1812.

(33)   Broach, R. W.; Jan, D.-Y.; Lesch, D. A.; Kulprathipanja, S.; Roland, E.; Kleinschmit, P. In *Ullmann's Encyclopedia of Industrial Chemistry*; Wiley-VCH Verlag GmbH & Co. KGaA: 2000.

(34)   Patrick, W. A. Silica gel and process of making same. United States of America Patent 1,297,724, March 18, 1919.

(35)   Feldman, M.; Desrochers, P. *Industry and Innovation* **2003**, *10*, 5.

(36)   Martin, A. J. P.; Synge, R. L. M. *Biochem. J.* **1941**, *35*, 1358.

(37)   Flörke, O. W.; Graetsch, H. A.; Brunk, F.; Benda, L.; Paschen, S.; Bergna, H. E.; Roberts, W. O.; Welsh, W. A.; Libanati, C.; Ettlinger, M.; Kerner, D.; Maier, M.; Meon, W.; Schmoll, R.; Gies, H.; Schiffmann, D. In *Ullmann's Encyclopedia of Industrial Chemistry*; Wiley-VCH Verlag GmbH & Co. KGaA: 2000.

(38)   Chester, T. L. *Anal. Chem.* **2012**, *85*, 579.

(39)   Wefers, K.; Misra, C. Oxides and Hydroxides of Aluminum, Alcoa Technical Paper no. 19, revised, Pittsburgh, 1987.

(40)   Melloer, J. W. *Modern Inorganic Chemistry*; Longmans, Green and Co.: London, 1925.

(41)   Bancroft, W. D.; Ackerman, J. W. *The Journal of Physical Chemistry* **1930**, *35*, 2568.

(42)   Taylor, H. S.; Gould, A. J. *J. Am. Chem. Soc.* **1934**, *56*, 1685.

(43)   Goodboy, K. P.; Fleming, H. L. *Chem. Eng. Prog.* **1984**, *80*, 63.

(44)   Coordination polymers, including crystalline coordination polymers, had been known well before Robson's work. However, Robson was the first to emphasize aspects of "design," where precursor geometry could lead to crystals of predictable net structure. Furthermore, Robson highlighted porosity as a defining characteristic of these materials, even predicting their utility in separations and catalysis, and the posibility of modifying the interior of these crystals after their synthesis (post-synthetic modification).

(45)   Kepert, C. J.; Rosseinsky, M. J. *Chem. Commun.* **1999**, 375.

(46)   Kondo, M.; Yoshitomi, T.; Matsuzaka, H.; Kitagawa, S.; Seki, K. *Angewandte Chemie International Edition in English* **1997**, *36*, 1725.

(47)   Mori, W.; Inoue, F.; Yoshida, K.; Nakayama, H.; Takamizawa, S.; Kishita, M. *Chem. Lett.* **1997**, *26*, 1219.

(48)   Boxhoorn, G.; Moolhuysen, J.; Coolegem, J. G. F.; van Santen, R. A. *J. Chem. Soc., Chem. Commun.* **1985**, 1305, and references therein.

(49)   Li, H.; Eddaoudi, M.; O'Keeffe, M.; Yaghi, O. M. *Nature* **1999**, *402*, 276.

(50)   Chui, S. S.-Y.; Lo, S. M. F.; Charmant, J. P. H.; Orpen, A. G.; Williams, I. D. *Science* **1999**, *283*, 1148.

(51)   Suh, M. P.; Park, H. J.; Prasad, T. K.; Lim, D.-W. *Chem. Rev.* **2012**, *112*, 782.

(52)   Li, J.-R.; Sculley, J.; Zhou, H.-C. *Chem. Rev.* **2011**, *112*, 869.

(53)   Lee, J.; Farha, O. K.; Roberts, J.; Scheidt, K. A.; Nguyen, S. T.; Hupp, J. T. *Chem. Soc. Rev.* **2009**, *38*, 1450.

(54)   Wang, C.; Zhang, T.; Lin, W. *Chem. Rev.* **2011**, *112*, 1084.

(55)   Mellot Draznieks, C.; Newsam, J. M.; Gorman, A. M.; Freeman, C. M.; Férey, G. *Angew. Chem., Int. Ed.* **2000**, *39*, 2270.

(56)   Férey, G.; Serre, C.; Mellot-Draznieks, C.; Millange, F.; Surblé, S.; Dutour, J.; Margiolaki, I. *Angew. Chem., Int. Ed.* **2004**, *43*, 6296.

(57)   Matsuda, R.; Kitaura, R.; Kitagawa, S.; Kubota, Y.; Belosludov, R. V.; Kobayashi, T. C.; Sakamoto, H.; Chiba, T.; Takata, M.; Kawazoe, Y.; Mita, Y. *Nature* **2005**, *436*, 238.

(58)   Kawano, M.; Haneda, T.; Hashizume, D.; Izumi, F.; Fujita, M. *Angew. Chem., Int. Ed.* **2008**, *47*, 1269.

(59)   Martí-Rujas , J.; Islam, N.; Hashizume, D.; Izumi, F.; Fujita, M.; Song, H. J.; Choi, H. C.; Kawano, M. *Angew. Chem., Int. Ed.* **2011**, *50*, 6105.

(60)   Marti-Rujas, J.; Matsushita, Y.; Izumi, F.; Fujita, M.; Kawano, M. *Chem. Commun.* **2010**, *46*, 6515.

(61)   Fujii, K.; Garay, A. L.; Hill, J.; Sbircea, E.; Pan, Z.; Xu, M.; Apperley, D. C.; James, S. L.; Harris, K. D. M. *Chem. Commun.* **2010**, *46*, 7572.

(62)   Friščić, T.; Meštrović, E.; Škalec Šamec, D.; Kaitner, B.; Fábián, L. *Chem.–Eur. J.* **2009**, *15*, 12644.

(63)   Yakovenko, A. A.; Reibenspies, J. H.; Bhuvanesh, N.; Zhou, H.-C. *J. Appl. Crystallogr.* **2013**, *46*, 346.

(64)   Gándara, F.; Uribe-Romo, F. J.; Britt, D. K.; Furukawa, H.; Lei, L.; Cheng, R.; Duan, X.; O'Keeffe, M.; Yaghi, O. M. *Chem.–Eur. J.* **2012**, *18*, 10595.

(65)   Connolly, M. L. *J. Appl. Crystallogr.* **1983**, *16*, 548.

(66)   Düren, T.; Millange, F.; Férey, G.; Walton, K. S.; Snurr, R. Q. *J. Phys. Chem. C* **2007**, *111*, 15350.

(67)   Nelson, A. P.; Farha, O. K.; Mulfort, K. L.; Hupp, J. T. *J. Am. Chem. Soc.* **2009**, *131*, 458.

(68)   Farha, O. K.; Eryazici, I.; Jeong, N. C.; Hauser, B. G.; Wilmer, C. E.; Sarjeant, A. A.; Snurr, R. Q.; Nguyen, S. T.; Yazaydın, A. Ö.; Hupp, J. T. *J. Am. Chem. Soc.* **2012**, *134*, 15016.

(69)   Brunauer, S.; Emmett, P. H.; Teller, E. *J. Am. Chem. Soc.* **1938**, *60*, 309.

(70)   Walton, K. S.; Snurr, R. Q. *J. Am. Chem. Soc.* **2007**, *129*, 8552.

(71)   Langmuir, I. *J. Am. Chem. Soc.* **1918**, *40*, 1361.

(72)   Horváth, G.; Kawazoe, K. *J. Chem. Eng. Jpn.* **1983**, *16*, 470.

(73)   Dubinin, M. M.; Radushkevich, L. V. *Dokl. Akad. Nauk SSSR* **1947**, *55*, 331.

(74)   Stoeckli, H. F. *Carbon* **1990**, *28*, 1.

(75)   Hafizovic, J.; Bjørgen, M.; Olsbye, U.; Dietzel, P. D. C.; Bordiga, S.; Prestipino, C.; Lamberti, C.; Lillerud, K. P. *J. Am. Chem. Soc.* **2007**, *129*, 3612.

(76)   Tsao, C.-S.; Yu, M.-S.; Chung, T.-Y.; Wu, H.-C.; Wang, C.-Y.; Chang, K.-S.; Chen, H.-L. *J. Am. Chem. Soc.* **2007**, *129*, 15997.

(77)   Hibbe, F.; Chmelik, C.; Heinke, L.; Pramanik, S.; Li, J.; Ruthven, D. M.; Tzoulaki, D.; Kärger, J. *J. Am. Chem. Soc.* **2011**, *133*, 2804.

(78)   Heinke, L.; Kärger, J. *Phys. Rev. Lett.* **2011**, *106*.

(79)   Liao, Y.; Yang, S. K.; Koh, K.; Matzger, A. J.; Biteen, J. S. *Nano Lett.* **2012**, *12*, 3080.

(80)   Ameloot, R.; Vermoortele, F.; Hofkens, J.; De Schryver, F. C.; De Vos, D. E.; Roeffaers, M. B. J. *Angew. Chem., Int. Ed.* **2013**, *52*, 401.

(81)   Cubillas, P.; Anderson, M. W.; Attfield, M. P. *Chem.–Eur. J.* **2012**, *18*, 15406.

(82)   Shöâeè, M.; Agger, J. R.; Anderson, M. W.; Attfield, M. P. *CrystEngComm* **2008**, *10*, 646.

(83)   Moh, P. Y.; Cubillas, P.; Anderson, M. W.; Attfield, M. P. *J. Am. Chem. Soc.* **2011**, *133*, 13304.

(84)   Gidley, D. W.; Peng, H. G.; Vallery, R. S. *Ann. Rev. Mater. Res.* **2006**, *36*, 49.

(85)   An excellent web resource providing clear, technical descriptions of positron and positronium-based analysis techniques can be found at http://www.positronannihilation.net/.

(86)   Tao, S. J. *J. Chem. Phys.* **1972**, *56*, 5499.

(87)   Eldrup, M.; Lightbody, D.; Sherwood, J. N. *Chem. Phys.* **1981**, *63*, 51.

(88)   Dull, T. L.; Frieze, W. E.; Gidley, D. W.; Sun, J. N.; Yee, A. F. *J. Phys. Chem. B* **2001**, *105*, 4657.

(89)   Jasińska, B.; Dawidowicz, A. L.; Goworek, T.; Wawryszczuk, J. *Opt. Appl.* **2003**, *33*, 7.

(90)   While the distribution of positron stopping in a material has an easily controlled center (or in other words, an easily controlled average depth), the width of the distribution increases with increasing implantation energy. Furthermore, while Ps is formed where positrons stop in a material, for materials having highly interconnected and open pores, Ps can diffuse long distances before annhilation (see Appendix A), thereby limiting the ability of depth-profiling measurements to give accurate data on depth-dependent pore characteristics.

(91)   Liu, M.; Wong-Foy, A. G.; Vallery, R. S.; Frieze, W. E.; Schnobrich, J. K.; Gidley, D. W.; Matzger, A. J. *Adv. Mater.* **2010**, *22*, 1598.

(92)   Feldblyum, J. I.; Liu, M.; Gidley, D. W.; Matzger, A. J. *J. Am. Chem. Soc.* **2011**, *133*, 18257.

(93)   Feldblyum, J. I.; Wong-Foy, A. G.; Matzger, A. J. *Chem. Commun.* **2012**, *48*, 9828.

(94)   Liu, B.; Wong-Foy, A. G.; Matzger, A. J. *Chem. Commun.* **2013**, *49*, 1419.

(95)   Feldblyum, J. I.; Dutta, D.; Wong-Foy, A. G.; Dailly, A.; Imirzian, J.; Gidley, D. W.; Matzger, A. J. *Langmuir* **2013**.

(96)   Dutta, D.; Feldblyum, J. I.; Gidley, D. W.; Imirzian, J.; Liu, M.; Matzger, A. J.; Vallery, R. S.; Wong-Foy, A. G. *Phys. Rev. Lett.* **2013**, *110*, 197403.

(97)   Villaescusa, L. A.; Wheatley, P. S.; Bull, I.; Lightfoot, P.; Morris, R. E. *J. Am. Chem. Soc.* **2001**, *123*, 8797.

(98)   Hoskins, B. F.; Robson, R. *J. Am. Chem. Soc.* **1989**, *111*, 5962.

Chapter 2

Reconciling the Discrepancies between Crystallographic Porosity and Guest Access as Exemplified by Zn-HKUST-1[†]

2.1   Introduction

The myriad and tunable chemistries and pore structures of microporous coordination polymers (MCPs) have significantly expanded the potential capabilities of porous materials.[1] MCPs have shown great promise for applications such as gas separation[2] and storage,[3] catalysis,[4] and selective adsorption from the liquid phase.[5] However, for many MCPs there is a discrepancy between the theoretical surface area predicted by crystallographic considerations and experimentally determined porosity.[6-8] Although underperformance in MCPs has been attributed to interpenetration,[9] incomplete removal of guests from pores,[10] and pore collapse,[11] and various methodologies have been employed to achieve higher porosity,[11,12] direct detection and analysis of these failure modes remains difficult and can yield ambiguous results. The structural purity of MCPs is most often analyzed by X-ray diffraction and gas sorption techniques. Powder X-ray diffraction (PXRD) can yield information about crystallinity, but is less well suited for examining disorder. Gas sorption techniques provide quantitative measurements of accessible internal surface area but are subject to kinetic limitations and do not probe closed pores.

In this study, we describe investigations on an MCP that, despite promising structural data, fails to yield substantial gas uptake by conventional gas sorption techniques. A strategy for improving the performance of MCPs for specific applications

is the discovery and employment of isostructural analogues where one metal is replaced with another or different metals are mixed in the same structure.[13] Lighter metals can be used in this manner to improve surface area,[14-16] and selection of metal can be used to enhance and control catalytic and photocatalytic activity.[17,18] $Cu_3(btc)_2$ (commonly "HKUST-1," hereafter "Cu-HKUST-1") was one of the first MCPs demonstrated to retain its crystal structure and exhibit permanent porosity upon removal of guest molecules.[19] In addition, it is one of the few commercially marketed MCPs[20] and a great deal of effort has been spent on making it an industrially viable and useful material.[21-24] The prevalence of zinc paddlewheels[25] in a variety of MCPs suggests that Zn is a promising metal with which to construct an isostructural analogue to Cu-HKUST-1 ($Zn_3(btc)_2$, hereafter "Zn-HKUST-1"); however, zinc paddlewheel MCPs frequently exhibit lower-than-expected surface areas or complete collapse upon removal of axial ligands.[26,27] Although the failure of these materials to exhibit theoretically achievable porosity has not been explored in detail, their underperformance may be due to structural rearrangement or distortion of the Zn-paddlewheel under dry conditions.[28,29] Although Zn-HKUST-1 was synthesized previously,[30] no evidence of permanent porosity was reported.

Our group recently applied positron annihilation lifetime spectroscopy (PALS)[31,32] to investigate the porosity, thermal stability, and CO_2 gas adsorption of the prototypical MCP MOF-5.[33] Positron interaction with dielectric materials can form positronium, the atom-like bound state of a positron and an electron. The electron and positron comprising a positronium atom can have either parallel or antiparallel spins. The species with parallel spins, *ortho*-positronium (*o*-Ps), has a characteristic lifetime in vacuum of 142 ns. In a porous dielectric material, the lifetime of *o*-Ps is reduced in a manner directly related to the size of pores within that material. By bombarding a sample with positrons and detecting γ-rays emitted from *o*-Ps decay, a *o*-Ps lifetime (or a distribution of lifetimes) can be determined and correlated to a precise pore size (or pore size distribution) for the analyzed material. PALS has inherent advantages over gas sorption techniques as an analytical tool to study porous materials. Most importantly, an accessible, interconnected pore space is not required to yield pore size and occurrence data, as energetic positrons will pass directly through insulating material until losing

enough energy to form positronium or annihilate directly via positron-electron interaction.[31] In addition, by tuning the energy of implanted positrons, the bulk and surface of a material can be studied separately.

Using a combination of PXRD, gas sorption analysis, PALS, depth-profiled PALS, optical microscopy, and NMR spectroscopy, a thorough analysis of the failure mode of Zn-HKUST-1 is provided. Crystallinity after evacuation is maintained, yet no observable porosity by gas sorption analysis is found. PALS provides an explanation for these results and is able to demonstrate that the surface of Zn-HKUST-1 is unstable after drying.

2.2   Results and Discussion

The crystallinity of Zn-HKUST-1 was probed by PXRD (Figure 2.2) immediately after crystal growth and after evacuation under reduced pressure (~20 mTorr). Zn-HKUST-1 appears isostructural to Cu-HKUST-1, with a slightly larger unit cell (Cu-HKUST-1 $a = 26.343 \pm 0.005$ Å,[19] Zn-HKUST-1 $a = 26.520 \pm 0.001$ Å, determined from indexing PXRD data obtained at room temperature). Differences in peak intensities between simulated and experimental diffractograms can be attributed to coordinated guest molecules. Such differences in peak intensity have previously been attributed to pore occlusion by molecular guests.[9] Despite retention of crystallinity after attempted activation, no condition was found for which Zn-HKUST-1 exhibited significant porosity by N_2 adsorption surface area measurements. Attempted activation methods included evacuation at both room temperature and at 170 °C, use of DMF, $CHCl_3$, and benzene[11] as activation solvents, activation by flowing dry nitrogen at atmospheric pressure, and activation using supercritical CO_2.[12] Furthermore, attempts at accessing the pores of dry Zn-HKUST-1 crystals by adsorption of Ar at 87 K or CO_2 at 298 K yielded no indication of porosity in the material (see Figure 2.3 for representative isotherms).

Reasonable hypotheses for the failure of Zn-HKUST-1 to exhibit porosity include complete or partial structural collapse upon drying, interpenetration, an inability to remove molecular guests trapped in the framework, and/or the presence of a surface layer[34,35] blocking entry of gases into the crystal. Powder X-ray diffraction data (Figure

2.2) were used to rule out complete structural collapse. Computational modeling of a hypothetical interpenetrated material having the framework structure of Cu-HKUST-1 (HKUST-1_int) showed that interpenetration was unlikely due to steric hindrance between interpenetrating frameworks (Figure 2.4). Furthermore, a simulated powder X-ray diffractogram of HKUST-1_int lacked peaks at 6.7° and 11.55° that are present in the simulated and experimentally determined powder X-ray diffractograms of Cu-HKUST-1 and Zn-HKUST-1 (Figure 2.5). Upon ^{1}H NMR analysis of Zn-HKUST-1 dried under dynamic vacuum at 170 °C (see Experimental Methods), DMF was found to be present at a ratio of 2.19:1 DMF:btc (Figure 2.6). The NMR data corroborates the sorption data that indicates a closed structure, but cannot be used to rule out one or another hypothesis, as DMF might reasonably be found trapped in the MCP framework considering any of the failure models enumerated above.

Given its proven utility in probing buried pores[32] and MCP pore systems,[33] PALS was used to determine whether empty pores remained within activated Zn-HKUST-1 crystals. *O*-Ps annihilation lifetimes were determined by fitting the raw lifetime data (Figure 2.7) to multiple, superimposed exponential decays. Two separate *o*-Ps decay components were found corresponding to lifetimes of 2.13 ± 0.13 ns and 5.24 ± 0.17 ns, as would be expected were *o*-Ps trapped in either the small or the large pores present in the Zn-HKUST-1 crystal structure (Figure 2.1). The fitting of these two distinct lifetimes indicates that *o*-Ps does not freely diffuse through the Zn-HKUST-1 pore space because a freely-diffusing *o*-Ps atom would sample all voids and thus only a single average *o*-Ps lifetime would be fit in the spectrum (beam PALS results below will confirm this claim of trapping). Using quantum mechanical models[36-39] to correlate calculated lifetimes to pore sizes, pore diameters of 0.59 ± 0.02 nm and 0.97 ± 0.02 nm were deduced. Pore sizes were determined from the crystal structure using the diameters of the inscribed sphere (Figure 2.1) of each pore (taking into account neutral van der Waals radii of relevant atoms at the pore walls). Idealized pore sizes for the small and large pores determined in this manner are 0.56 nm and 1.10 nm, respectively, in good agreement with PALS-derived values. The fractional contributions from each lifetime component, provided as intensities relative to the total number of all positrons emitted from the ^{22}Na source, were 5.1 ± 0.2% and 4.5 ± 0.3% for the small and large pores, respectively (note

that since in our PALS apparatus only half the positrons from the ^{22}Na source can stop in the sample, these intensities should be doubled when comparing with beam PALS results below). In the ideal crystal structure, the number of small pores is equal to the number of large pores. However, the larger pores, having nearly four times the surface area and eight times the volume of the smaller pores, will preferentially trap positronium. Hence, these initial PALS data hint at a deficit in the number of empty large pores compared with that expected from the ideal Zn-HKUST-1 crystal structure. For a pristine crystal, an intensity significantly greater than 5.1% would be expected for the large pore annihilation component. The depth dependence of this deviation is explored and discussed below. The small apertures between large and small pores, possibly constricted further by the presence of residual solvent (as evidenced by solution ^{1}H NMR of dissolved Zn-HKUST-1; see Experimental Methods), may account for *o*-Ps trapping in individual voids. As such *o*-Ps trapping on time scales of 5-10 ns does not rule out gas uptake into interconnected 1 nanometer voids on a time scale 10^9 times longer, these data solely demonstrate the presence of empty pores generally consistent with the crystallographic structure of Zn-HKUST-1.

As experimental PALS data describes a structure in which at least a significant fraction of pores in the *bulk* are present and accessible by positrons and *o*-Ps, depth-profiled beam PALS[32] was used to examine the pore structure at the surface of Zn-HKUST-1. By moderating the energy of positrons directed toward the sample, the positron mean implantation depth, and hence, the depth of *o*-Ps formation, was controlled. The depth profiling results (Figure 2.8) are very revealing. First, no *o*-Ps diffuses through interconnected pores back to the sample surface where it would escape into vacuum. This is consistent with *o*-Ps trapping in the pores and/or with pores sealed at the surface to prevent any escape. Additionally, fitting the lifetime spectrum at each implantation depth requires two *o*-Ps lifetimes corresponding to two pore sizes similar to those found by bulk fitting (Figure 2.8a), for which the intensity of *o*-Ps annihilating in the larger pore is a factor of five lower in the region within 500 nm of the crystal surface than in the bulk (Figure 2.8b). At the shallowest mean implantation depth (16 nm), there is *virtually no* o-*Ps annihilation in the larger pores*. Throughout the surface region the intensity of *o*-Ps annihilating in the larger pores gradually increases with depth, but is still

much lower than that in the bulk of the crystal. Moreover, the top 30-40 nm may be largely devoid of the larger pores due to complete collapse of the structure, leaving only microvoids from debris (as a result, the fitted values of the short and long o-Ps lifetimes could well deviate from those of the bulk crystal). This clearly indicates that the surface of the Zn-HKUST-1 crystal is densified, presumably due to pore collapse. As the large pores are necessary for interconnection between all pore space within the framework, a blocking or complete collapse of large pores at the surface effectively inhibits the ability of adsorbates such as N_2 gas from entering the bulk structure.

To further explore the instability of the large pores in Zn-HKUST-1, a bulk sample was heated to 50 °C for 30 minutes, cooled to room temperature, and subsequently analyzed by PALS (Figure 2.9). This procedure was then repeated on the same sample at 100 °C, 150 °C, and 200 °C. After the initial period of heating, the pore characteristics remained largely unchanged. However, at 100 °C, the intensity of o-Ps annihilation in the large pores dropped by a factor of about two to 2.47 ± 0.23%, and on further heating at higher temperatures, o-Ps annihilation in the large pores dropped to 0.51 ± 0.29%, accounting for only a small fraction of the open pore space left in the material (Figure 2.9b). At higher temperatures, a concomitant decrease in the size of the large pores was observed (Figure 2.9a). In contrast, the intensities and pore sizes of the small pores showed little change over successive heating and cooling cycles. The slight increase in o-Ps annihilation intensity in the small pores at higher temperatures can be attributed to reduced o-Ps formation in large pores, limiting annihilation to the small pores of the material. Both the reduced occurrence and reduced pore size indicate collapse solely of the larger pores after heating at higher temperatures. These trends are consistent with degradation of the bulk material and indicate that the larger pores responsible for gas transport exhibit comparatively poorer durability. Presumably, the surface of the crystal is even less durable to pore collapse than the interior, even without heating.

Having confirmed the nature of structural failure in Zn-HKUST-1, a sample of activated Zn-HKUST-1 was mechanically crushed under a nitrogen atmosphere to determine whether the surface layer was due to the presence of dense guest-filled layer or collapse of the crystal itself. No porosity was observed by measuring N_2 uptake (Figure

24

2.10) of the crushed Zn-HKUST-1 at 77 K, indicating that the surface collapse is apparently due to inherent instability of the dry material (Figure 2.11). This instability suggests that further attempts at activation, barring post-synthetic chemical modification, are unlikely to yield a dry, stable, porous material.

Although the surface of Zn-HKUST-1 appears to be unstable, highly ordered crystals grow to sizes of up to 100 μm when solvothermally synthesized in DMF (Figure 2.12a). To examine whether molecular guests could enter the pores of Zn-HKUST-1 in solvent, MCP crystals were immersed in saturated solutions of strongly-colored species including Nile red, methylene blue, azobenzene, and elemental iodine. Only iodine was found to diffuse slowly into Zn-HKUST-1 crystals, as evidenced by a color change from colorless to dark orange-brown over a period of 7 days (Figure 2.12b). The small pore aperture of the larger pores (0.66 nm after complete removal of axially coordinated ligands) precluded adsorption of the organic dyes. The lack of organic dye uptake also eliminates the possibility that iodine uptake was due to mesopore or macropore defects. To examine the diffusion of iodine in the HKUST-1 structure further, a layer of Zn-HKUST-1 was grown on crystals of Cu-HKUST-1 in a core-shell configuration[40,41] (Zn-HKUST-1@Cu-HKUST-1, Figure 2.12c, Figure 2.13). Such a configuration provided a more rapid means to confirm the diffusion of iodine into the crystal due to the strong color contrast between iodine in $CHCl_3$ and Cu-HKUST-1. After immersion in saturated iodine/$CHCl_3$ for a single day, substantial diffusion of iodine into the copper portion of Zn-HKUST-1@Cu-HKUST-1 was observed (Figure 2.12d). These results show that in solution, both bulk Zn-HKUST-1 crystals and Zn-HKUST-1 shells bound to Cu-HKUST-1 cores are stable and exhibit accessible, interconnected pore space before the removal of solvents. In contrast, crystals of Zn-HKUST-1 soaked in saturated iodine/$CHCl_3$ after evacuation exhibited no observable iodine uptake after 7 days (Figure 2.14). This behavior is consistent with the other observations in this study, suggesting that after surface densification on evacuation, re-immersion of Zn-HKUST-1 in solvent does not re-stabilize the surface open it to guest inclusion.

2.3   Conclusions

A detailed description of the mode of failure in the MCP Zn-HKUST-1 has been presented. Retention of crystallinity after activation juxtaposed with a demonstrated lack of accessible porosity can be explained by combining bulk and depth-profiled PALS data. Analysis by these techniques reveals the preservation of an ordered and open pore network in the bulk of the Zn-HKUST-1 crystals made inaccessible by a densified layer at the surface. The instability of the Zn-HKUST-1 surface was shown to be characteristic of the material in dry environments, as dry, crushed crystals exhibited no significant uptake of N_2 gas despite an interior shown to have open pore space. In contrast, the material exhibited accessible porosity before removal of solvent by the infusion of iodine both throughout bulk Zn-HKUST-1 crystals and through Zn-HKUST-1 layers encapsulating Cu-HKUST-1 crystals immersed in $CHCl_3$.

These results deepen the understanding of a previously unknown[42] mode of failure in MCPs and suggest that a lack of observable gas uptake in dried crystals should not be taken as conclusive evidence for complete structural collapse or pore filling by guests. Although some MCPs may require specialized activation techniques[11,12] to maintain stability in the dry state, it has been shown that instability of specific structural features (for example, the largest pores) within an MCP may fundamentally limit porosity for solvent-free applications. Porous materials exhibiting a lack of accessible internal surface area after solvent removal may still be useful for liquid-phase adsorption applications,[43-45] where pores may remain open and interconnected.

2.4   Experimental Methods

Synthesis of $Zn_3(btc)_2$ (Zn-HKUST-1). A mixture of 1,3,5-benzene tricarboxylic acid (H_3BTC, 39.5 mg, 0.188 mmol, Acros Organics) and $Zn(NO_3)_2 \bullet 6H_2O$ (170.7 mg, 0.574 mmol, Fisher Scientific) was dissolved in 10 mL N,N-dimethylformamide (DMF, Fisher Scientific), aided by sonication. The resultant solution was filtered through P5 filter paper (Fisher Scientific) into a 20 mL scintillation vial and subsequently incubated at 85 °C for ~16 hours. Incubation yielded colorless, transparent cubic crystals. Note that longer incubation times yielded opaque white crystals exhibiting poorer crystallinity

26

when analyzed by PXRD. After incubation, solvent was decanted and replaced with ~10 mL pure DMF three times. The solvent was then decanted and replaced with chloroform four times over the next 48 hours, during which the sample was stored in a tightly capped vial in a desiccator. The sample was then held under dynamic vacuum (20 mTorr) at room temperature for ~10 h and transferred to a N_2 glove box for storage and further analysis.

Synthesis of Zn-HKUST-1@Cu-HKUST-1. 5 mL >18.2 MΩ cm^{-1} H_2O, 5 mL ethanol (Decon Labs), and 5 mL DMF were added to a mixture of 0.30 g H_3btc (1.43 mmol) and 0.60 g $Cu(NO_3)_2$•$2.5H_2O$ (2.58 mmol, Fisher Scientific) in a 20 mL scintillation vial. The resultant solution was sonicated until it became a uniform cloudy blue color (~5 minutes). Concentrated HCl was then added dropwise until the solution became a transparent blue (~12 drops from a glass pipet). The clear solution was incubated at 85 °C for ~20 hours, after which a thick layer of blue Cu-HKUST-1 crystals formed at the bottom of the vial. The vial was removed and allowed to cool to room temperature. The solvent was subsequently decanted and replaced three times with ~10 mL fresh DMF.

In a separate 20 mL scintillation vial, a precursor solution of Zn-HKUST-1 was prepared by adding 0.228 g $Zn(NO_3)_2$•$6H_2O$ (0.765 mmol), 0.0526 g H_3btc (0.250 mmol), and 10 mL DMF and sonicating until complete dissolution of the solid. The solvent from the vial containing the Cu-HKUST-1 was decanted and replaced with the Zn-HKUST-1 precursor solution. The crystals in the precursor solution were incubated at 85 °C for ~20 hours and subsequently cooled to room temperature. The solvent was immediately exchanged three times with pure DMF and analyzed by PXRD. Upon further examination by optical microscopy, a heterogeneous mixture of Cu-HKUST-1 and Zn-HKUST-1@Cu-HKUST-1 was observed.

Infusion of iodine in Zn-HKUST-1 and Zn-HKUST-1@Cu-HKUST-1. Zn-HKUST-1 was synthesized in DMF as described above. After crystals formed, the solvent was decanted and replaced with ~10 mL pure DMF three times. The solvent was then decanted and replaced with chloroform, after which crystals were analyzed by PXRD. Crystals were then transferred to a 4 mL vial containing a minimum amount of chloroform (~0.5 mL) to keep samples submerged for one week. Elemental iodine (Fisher

Scientific) was added liberally until the solution reached saturation. The vial containing Zn-HKUST-1, solvated iodine, and solid iodine was placed on a shaker (IKA KS 260) and agitated at 120 rpm for 7 days. Crystals were then analyzed by PXRD and optical microscopy. To visualize cross sections, a single crystal was isolated and carefully sliced on opposite sides with a razor to obtain a cross section from the center of the crystal (Figure 2.12). Crystals of Zn-HKUST-1@Cu-HKUST-1 were synthesized as described above. The sample was then treated similarly as described for Zn-HKUST-1, but immersion in saturated iodine/CHCl$_3$ was limited to 24 h. Crystals of Zn-HKUST-1 after evacuation were transferred from a N$_2$ glove box into a vial containing chloroform under ambient atmosphere. These crystals were soaked in saturated iodine for 7 days and imaged as described above.

Positron annihilation lifetime spectroscopy. The dry sample was loaded in a N$_2$ glove box into a well-type sample holder with a 4 μCi ^{22}Na positron source deposited on the bottom of the well. The sample holder was placed between two plastic scintillators to detect gamma rays signaling positron emission from the ^{22}Na formation and *o*-Ps annihilation. Before measurement of *o*-Ps lifetimes within the sample, the sample holder was evacuated to 10 mTorr to eliminate significant interaction between *o*-Ps and residual gas. A histogram of the lifetimes of discrete annihilation events was obtained at a rate of 60 counts per second (representative histogram in Figure 2.7). Pore sizes were determined from lifetime data with an extended Tao-Eldrup model[36-39] using in-house software. Samples remained in the PALS apparatus under dynamic vacuum (10^{-3} Torr) during sample heating and cooling, and measurements of heated samples were taken at room temperature after heating and subsequent cooling.

Depth-profiled positron annihilation lifetime spectroscopy. An optically thick layer of analyte was deposited on a piece of conductive tape attached to a sample holder. The sample holder was inserted into a depth-profiled PALS apparatus, in which monoenergetic positrons are focused on the sample under high vacuum conditions.[32] The energy of positrons impinging upon the sample was varied between 1-6 keV, controlling the depth at which *o*-Ps formed and annihilated within the sample. In this manner, information regarding pore size and relative porosity was obtained, as well as information about the ability of *o*-Ps to diffuse out of the structure before annihilation.

Surface area determination by N$_2$ gas sorption. Volumetric N$_2$ sorption isotherms were obtained on a Quantachrome NOVA 4200e, using 99.999% purity N$_2$ (Cryogenic Gases). Samples (~30 mg) were transferred to sample cells in a N$_2$ glove box and rapidly attached to the surface area analyzer to avoid exposure to air. Sample cells were immediately subject to dynamic vacuum, after which surface area analysis was performed.

Determination of CO$_2$ and Ar gas sorption. Volumetric CO$_2$ and Ar isotherms were obtained on a Quantachrome Autosorb-1C at room temperature and 87 K, respectively. Samples were treated identically as in N$_2$ gas sorption experiments described above. Gases used were of 99.999% purity (Cryogenic Gases).

Powder X-ray diffraction analysis. Analyte crystals were coated in Paratone N oil (Hampton Research), mounted on a Nylon loop, and placed in a goniometer head. Samples were then analyzed with a Rigaku R-Axis Spider diffractometer equipped with a CuKα X-ray source (λ = 1.5406 Å) operating at 50 kV and 40 mA. An image plate detector was used to collect images in 10 minute scans by transmission with χ = 45°, ϕ rotating at 10°/min, and ω oscillating between 80° and 140°. Integration of images was carried out using the AreaMax 2.0 software package with a step size of 0.2° in 2θ.

^{1}H Nuclear Magnetic Resonance Spectroscopy. Crystals of Zn-HKUST-1 were synthesized and washed with DMF and chloroform as described above. The Zn-HKUST-1 was then dried under dynamic vacuum (~20 mTorr) at 170 °C for ~10 h. After sorption analysis, the crystals were transferred rapidly from a nitrogen glove box atmosphere to a 1 M solution of NaOD in D$_2$O. The solution was agitated for ~5 minutes, after which time the crystals were completely dissolved. The resultant solution was characterized by ^{1}H NMR spectroscopy.

Simulation of hypothetical interpenetrated material having the framework structure of Cu-HKUST-1 (HKUST-1_int). Optimization of geometry and lattice parameters was performed in Materials Studio 4.3[46] using the Forcite module. The Universal force field[47] was employed using the Smart algorithm. Space group: *R*-3*m*; *a* = 33.166679 Å, *c* = 83.583213 Å.

2.5   Figures
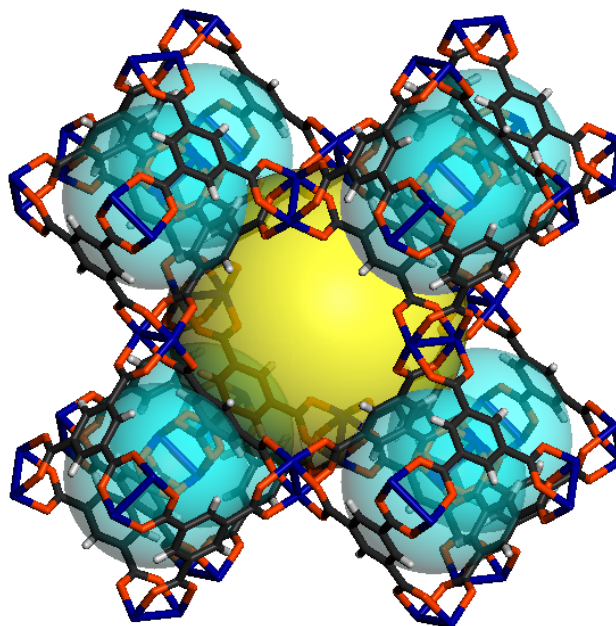
Figure 2.1. HKUST-1 structure as viewed down the [100] direction, angled slightly to show 3-dimensional structure (Cu, blue; C, black; O, red; H, light grey). The void spaces of the large and small pores present within the structure are depicted by yellow and blue spheres, respectively.
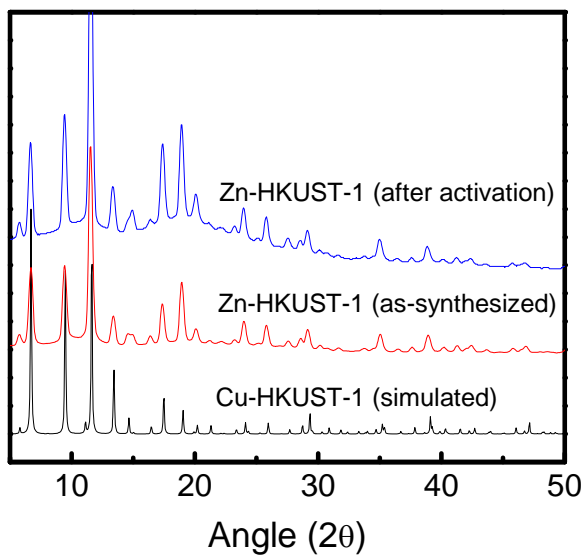
Figure 2.2. Powder X-ray diffractograms of Zn-HKUST-1 immediately after synthesis and after evacuation under reduced pressure (~20 mTorr) compared with simulated diffractogram of Cu-HKUST-1.
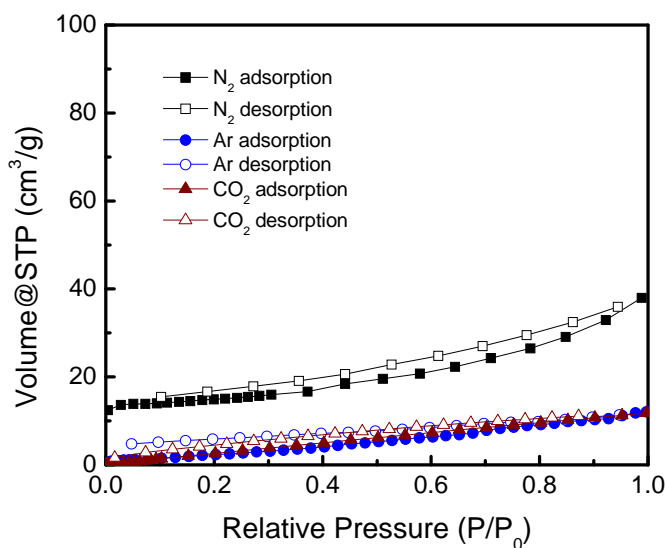
Figure 2.3. N_2 (77 K), Ar (87 K), and CO_2 (298 K) sorption isotherms of activated Zn-HKUST-1. The N_2 isotherm shown is that of the highest BET surface area (55 m^2/g) material obtained, and hence provides an upper bound for the samples analyzed (15 total). The majority of samples exhibited BET surface areas less than 10 m^2/g.
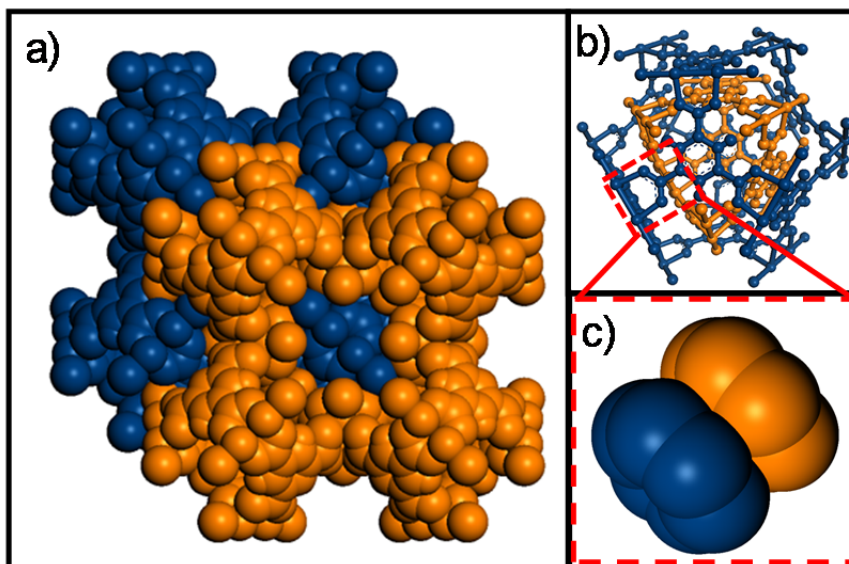
Figure 2.4. a) Space-filling model of HKUST-1_int. The centroid of the small pore of one framework is centered at the centroid of the large pore of the other framework to minimize steric hindrance. Axial oxygen atoms of copper paddlewheel clusters still overlap with carboxylate groups of the interpenetrating structure. b) Ball-and-stick model showing enclosed small cage of one framework in the larger cage of the other. c) Space-filling model of facing benzene rings of HKUST-1_int pore walls. Benzene rings are 2.85 Å apart.
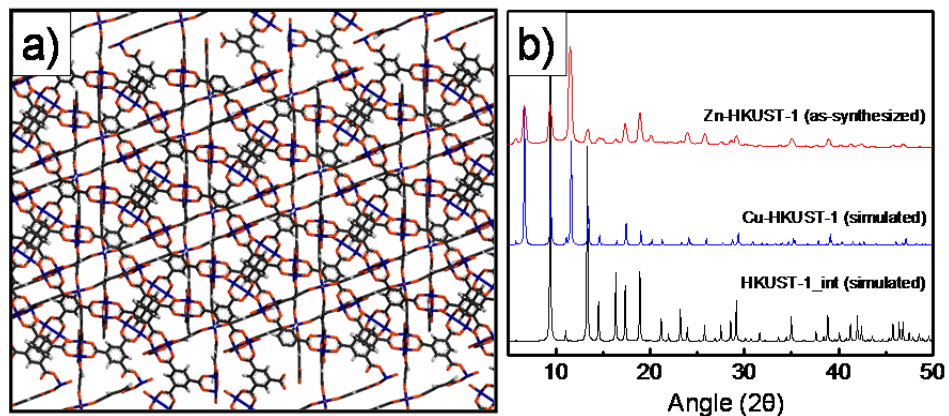
Figure 2.5. a) Crystal structure of HKUST-1_int viewed along the *a* axis. b) Simulated powder X-ray diffraction pattern of HKUST-1_int compared with powder patterns of Cu-HKUST-1 (simulated) and Zn-HKUST-1 (experimentally measured).
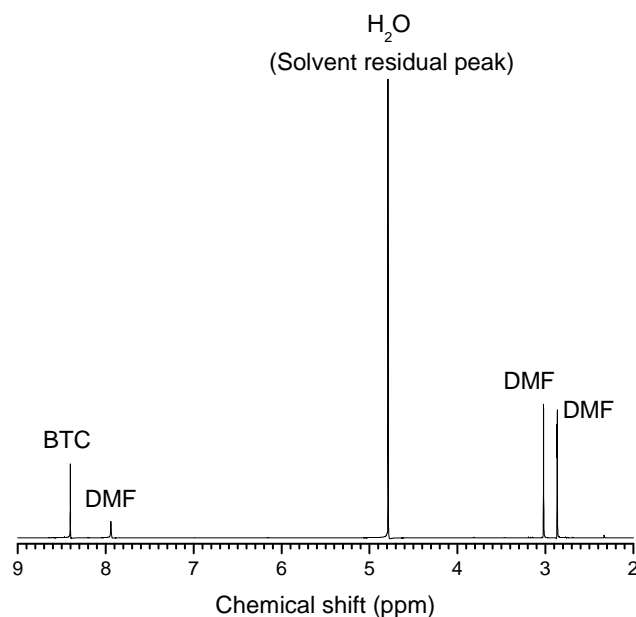
Figure 2.6. ^{1}H NMR spectrum of activated Zn-HKUST-1 dissolved in ~1 M NaOD/D_2O. The MCP was activated by repeated solvent exchange with chloroform (4 times over 3 days) followed by heating at 170 °C under dynamic vacuum (~20 mTorr). Peak identification shows significant presence of DMF within the framework even after evacuation. The ratio of btc:DMF was determined to be 1:2.19.
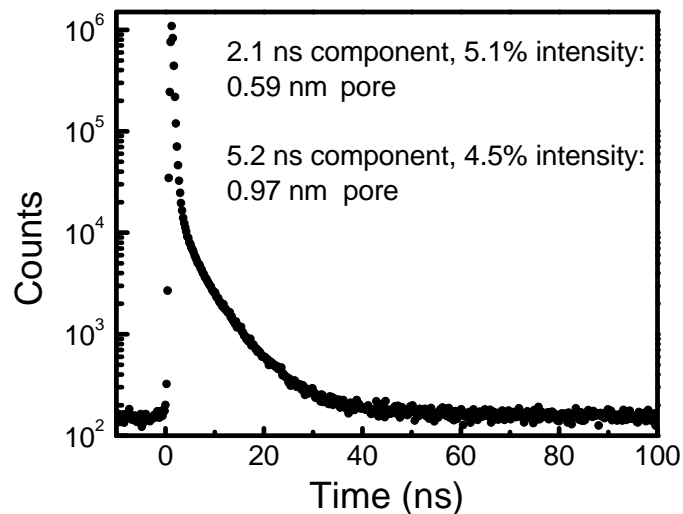
Figure 2.7. PALS spectrum of Zn-HKUST-1 after evacuation under reduced pressure (~20 mTorr). Lifetimes, relative intensities, and corresponding cubic pore lengths are provided.
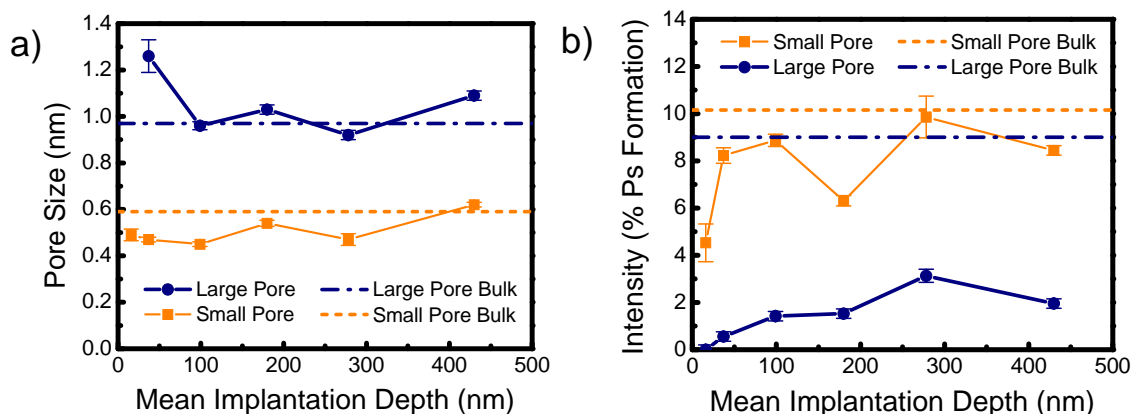
Figure 2.8. Beam PALS of Zn-HKUST-1 after evacuation under reduced pressure (~20 mTorr) showing a) pore size and b) annihilation intensity at controlled depths. Two pores were detected corresponding to the small and large pores expected from the Zn-HKUST-1 crystal structure. Values obtained at room temperature for small (dotted line) and large (dash-dotted line) pores by PALS measurements of crystal bulk from Figure 2.7 are shown for reference. Note that reference intensity values are doubled to account for differences in sample holder positioning between bulk and beam measurements. As no large pore component was detected at the shallowest depth (16 nm), no pore size was obtainable.
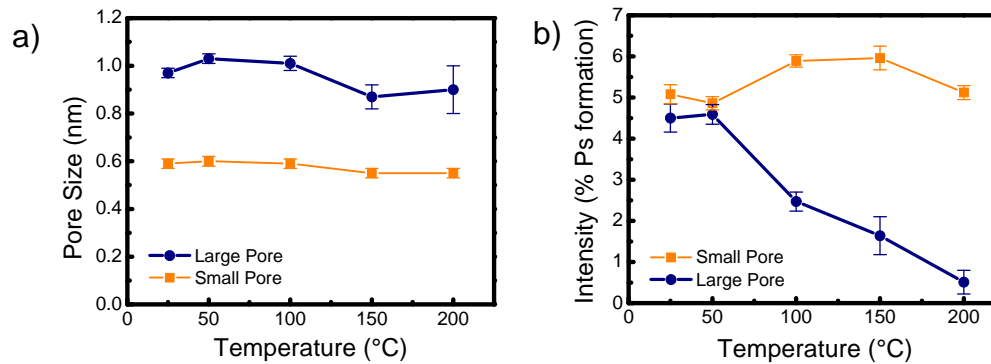
Figure 2.9. PALS measurements of small and large pores of Zn-HKUST-1 at room temperature (~25 °C) and after successive 30 minute heating/cooling cycles at temperatures up to 200 °C. a) Pore size and b) annihilation intensity of small pores remains largely unchanged, but large pore intensity vanishes as temperature increases.
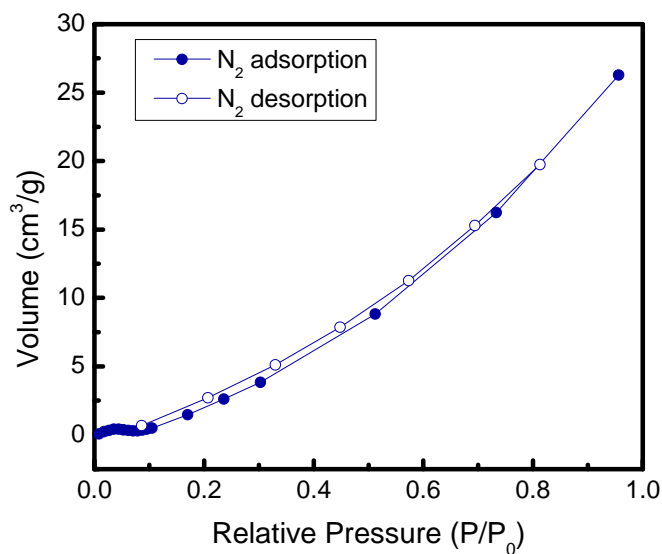
Figure 2.10. N_2 sorption isotherm at 77 K of activated Zn-HKUST-1 mechanically crushed under a nitrogen atmosphere. Lack of evidence for pore structure suggests spontaneous collapse of the crystal surface.
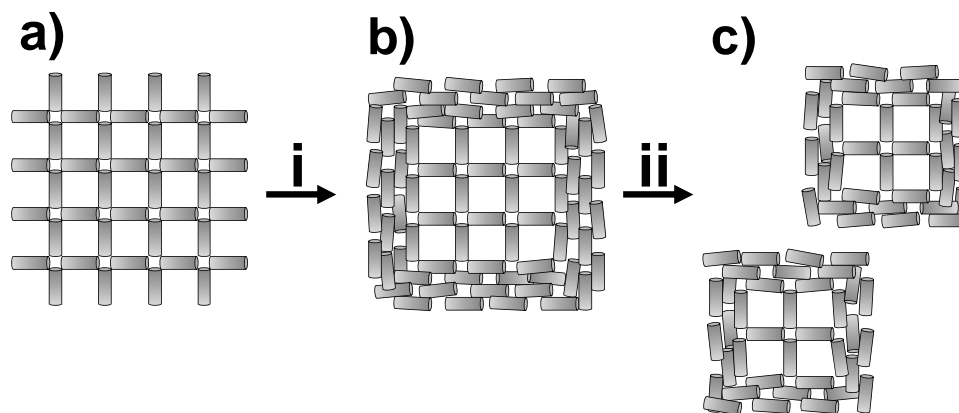
Figure 2.11. Schematic representation of material failure of Zn-HKUST-1. a) Solvent-filled material is open to guest exchange. After drying under vacuum (i), b) the surface of Zn-HKUST-1 collapses, leaving only small pores at the surface. Mechanically grinding the material into a fine powder (ii) leads to c) surface collapse of smaller Zn-HKUST-1 fragments.
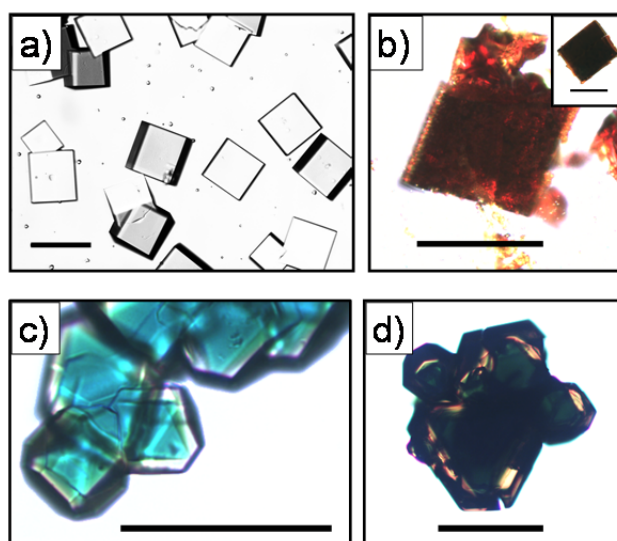
Figure 2.12. a) Optical micrograph of Zn-HKUST-1 examined immediately after crystallization. b) Optical micrograph of a cross section of Zn-HKUST-1 after immersion in saturated iodine/$CHCl_3$ solution for 7 days. Inset: crystal before cross section. c) Optical micrograph of Zn-HKUST-1@Cu-HKUST-1. d) Optical micrograph of Zn-HKUST-1@Cu-HKUST-1 after immersion in saturated iodine/$CHCl_3$ for 24 hours. Scale bars, 100 μm.
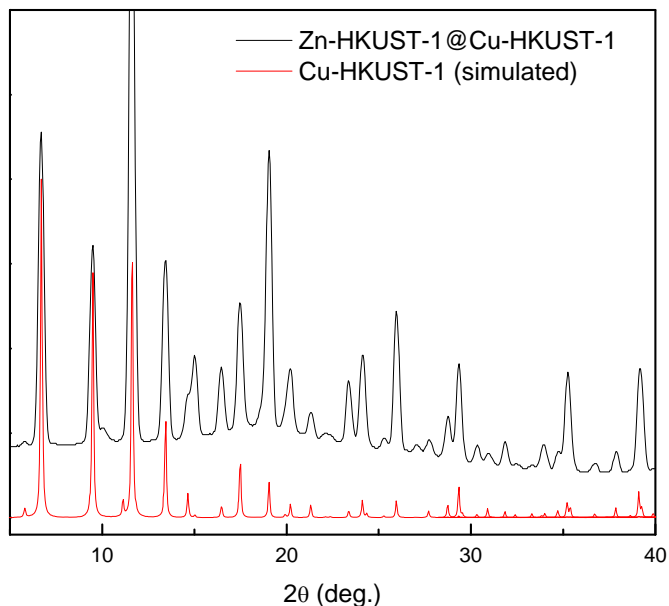
Figure 2.13. Powder X-ray diffractogram of Zn-HKUST-1@Cu-HKUST-1 immediately after synthesis and solvent replacement with fresh DMF.
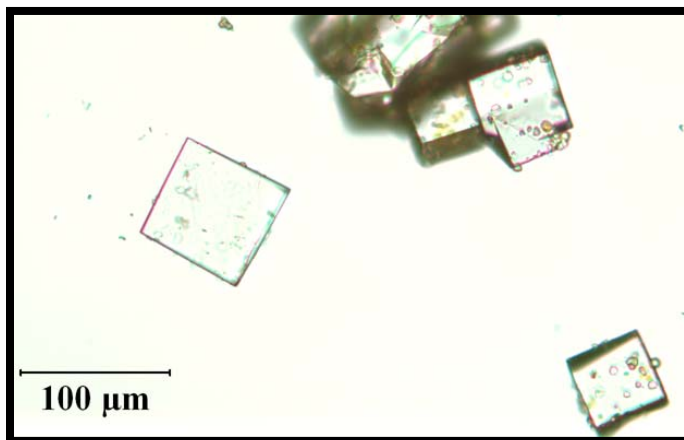
Figure 2.14. Optical micrograph of Zn-HKUST-1 crystals after drying under reduced pressure (~20 mTorr) and subsequently immersing in saturated iodine/CHCl$_3$ solution for 7 days. Crystals were rapidly rinsed with clean CHCl$_3$ to remove iodine adsorbed at the surface. In contrast to Zn-HKUST-1 immersed in saturated iodine/CHCl$_3$ solution before drying (Figure 2.12), no iodine uptake was observed.

2.6   References

(1)   Férey, G. *Chem. Soc. Rev.* **2008**, *37*, 191.
(2)   Li, J.-R.; Kuppler, R. J.; Zhou, H.-C. *Chem. Soc. Rev.* **2009**, *38*, 1477.
(3)   Murray, L. J.; Dincă, M.; Long, J. R. *Chem. Soc. Rev.* **2009**, *38*, 1294.
(4)   Lee, J.; Farha, O. K.; Roberts, J.; Scheidt, K. A.; Nguyen, S. T.; Hupp, J. T. *Chem. Soc. Rev.* **2009**, *38*, 1450.

(5)   Cychosz, K. A.; Ahmad, R.; Matzger, A. J. *Chem. Sci.* **2010**, *1*, 293.

(6)   Walton, K. S.; Snurr, R. Q. *J. Am. Chem. Soc.* **2007**, *129*, 8552.

(7)   Düren, T.; Bae, Y. S.; Snurr, R. Q. *Chem. Soc. Rev.* **2009**, *38*, 1237.

(8)   Schnobrich, J. K.; Koh, K.; Sura, K. N.; Matzger, A. J. *Langmuir* **2010**, *26*, 5808.

(9)   Hafizovic, J.; Bjørgen, M.; Olsbye, U.; Dietzel, P. D. C.; Bordiga, S.; Prestipino, C.; Lamberti, C.; Lillerud, K. P. *J. Am. Chem. Soc.* **2007**, *129*, 3612.

(10)   Barthelet, K.; Marrot, J.; Férey, G.; Riou, D. *Chem. Commun.* **2004**, 520.

(11)   Ma, L. Q.; Jin, A.; Xie, Z. G.; Lin, W. B. *Angew. Chem. Int. Ed.* **2009**, *48*, 9905.

(12)   Nelson, A. P.; Farha, O. K.; Mulfort, K. L.; Hupp, J. T. *J. Am. Chem. Soc.* **2009**, *131*, 458.

(13)   Lim, C. S.; Schnobrich, J. K.; Wong-Foy, A. G.; Matzger, A. J. *Inorg. Chem.* **2010**, *49*, 5271.

(14)   Caskey, S. R.; Wong-Foy, A. G.; Matzger, A. J. *J. Am. Chem. Soc.* **2008**, *130*, 10870.

(15)   Porter, W. W.; Wong-Foy, A.; Dailly, A.; Matzger, A. J. *J. Mater. Chem.* **2009**, *19*, 6489.

(16)   Hausdorf, S.; Baitalow, F.; Böhle, T.; Rafaja, D.; Mertens, F. O. R. L. *J. Am. Chem. Soc.* **2010**, *132*, 10978.

(17)   Wen, L.-L.; Wang, F.; Feng, J.; Lv, K.-L.; Wang, C.-G.; Li, D.-F. *Cryst. Growth Des.* **2009**, *9*, 3581.

(18)   Song, Y. J.; Kwak, H.; Lee, Y. M.; Kim, S. H.; Lee, S. H.; Park, B. K.; Jun, J. Y.; Yu, S. M.; Kim, C.; Kim, S.-J.; Kim, Y. *Polyhedron* **2009**, *28*, 1241.

(19)   Chui, S. S.-Y.; Lo, S. M. F.; Charmant, J. P. H.; Orpen, A. G.; Williams, I. D. *Science* **1999**, *283*, 1148.

(20)   McCoy, M. *Chem. Eng. News* **2010**, *88*, 18.

(21)   Ahmad, R.; Wong-Foy, A. G.; Matzger, A. J. *Langmuir* **2009**, 11977.

(22)   Mueller, U.; Schubert, M.; Teich, F.; Puetter, H.; Schierle-Arndt, K.; Pastré, J. *J. Mater. Chem.* **2006**, *16*, 626.

(23)   Czaja, A. U.; Trukhan, N.; Müller, U. *Chem. Soc. Rev.* **2009**, *38*, 1284.

(24)   Ameloot, R.; Stappers, L.; Fransaer, J.; Alaerts, L.; Sels, B. F.; De Vos, D. E. *Chem. Mater.* **2009**, *21*, 2580.

(25)   Vagin, S. I.; Ott, A. K.; Rieger, B. *Chem. Ing. Tech.* **2007**, *79*, 767.

(26)   Lee, Y.-G.; Moon, H. R.; Cheon, Y. E.; Suh, M. P. *Angew. Chem. Int. Ed.* **2008**, *47*, 7741.

(27)   Edgar, M.; Mitchell, R.; Slawin, A. M. Z.; Lightfoot, P.; Wright, P. A. *Chem. Eur. J.* **2001**, *7*, 5168.

(28)   Seo, J.; Bonneau, C.; Matsuda, R.; Takata, M.; Kitagawa, S. *J. Am. Chem. Soc.* **2011**, *133*, 9005.

(29)   Chen, B.; Liang, C.; Yang, J.; Contreras, D. S.; Clancy, Y. L.; Lobkovsky, E. B.; Yaghi, O. M.; Dai, S. *Angew. Chem. Int. Ed.* **2006**, *45*, 1390.

(30)   Fang, Q.-R.; Zhu, G.-S.; Xin, M.-H.; Zhang, D.-L.; Shi, X.; Wu, G.; Tian, G.; Tang, L.-L.; Xue, M.; Qiu, S.-L. *Chem. J. Chin. Univ.-Chin.* **2004**, *25*, 1016.

(31)   Charlton, M.; Humberston, J. W. *Positron Physics*; Cambridge University Press: Cambridge, 2001.

(32)   Gidley, D. W.; Peng, H. G.; Vallery, R. S. *Ann. Rev. Mater. Res.* **2006**, *36*, 49.

(33)   Liu, M.; Wong-Foy, A. G.; Vallery, R. S.; Frieze, W. E.; Schnobrich, J. K.; Gidley, D. W.; Matzger, A. J. *Adv. Mater.* **2010**, *22*, 1598.

(34)   Knipp, D.; Street, R. A.; Völkel, A.; Ho, J. *J. Appl. Phys.* **2003**, *93*, 347.

(35)   Xiao, K.; Liu, Y.; Qi, T.; Zhang, W.; Wang, F.; Gao, J.; Qiu, W.; Ma, Y.; Cui, G.; Chen, S.; Zhan, X.; Yu, G.; Qin, J.; Hu, W.; Zhu, D. *J. Am. Chem. Soc.* **2005**, *127*, 13281.

(36)   Tao, S. J. *J. Chem. Phys.* **1972**, *56*, 5499.

(37)   Eldrup, M.; Lightbody, D.; Sherwood, J. N. *Chem. Phys.* **1981**, *63*, 51.

(38)   Jasińska, B.; Dawidowicz, A. L.; Goworek, T.; Wawryszczuk, J. *Opt. Appl.* **2003**, *33*, 7.

(39)   Dull, T. L.; Frieze, W. E.; Gidley, D. W.; Sun, J. N.; Yee, A. F. *J. Phys. Chem. B* **2001**, *105*, 4657.

(40)   Koh, K.; Wong-Foy, A. G.; Matzger, A. J. *Chem. Commun.* **2009**, 6162.

(41)   Yoo, Y.; Jeong, H.-K. *Cryst. Growth Des.* **2010**, *10*, 1283.

(42)   The surface barrier phenomenon has been investigated previously in zeolites (for example, Micke, A.; Bülow, M.; Kočirík, M. *J. Phys Chem.* **1994**, *98*, 924-929) and very recently in a model MCP (see refs 48 and 49). In the more recent studies, the surface was characterized as having a heterogeneous mixture of completely blocked (zero-permeability) and completely open (infinite permeability) sites. A logical extension of this concept may be applicable to our material, where the surface is characterized solely by sites of zero-permeability. This contrasts with earlier work since pore blockage in Zn-HKUST-1 is found to be complete by gas sorption experiments.

(43)   Maes, M.; Vermoortele, F.; Alaerts, L.; Couck, S.; Kirschhock, C. E. A.; Denayer, J. F. M.; De Vos, D. E. *J. Am. Chem. Soc.* **2010**, *132*, 15277.

(44)   Ameloot, R.; Liekens, A.; Alaerts, L.; Maes, M.; Galarneau, A.; Coq, B.; Desmet, G.; Sels, B. F.; Denayer, J. F. M.; De Vos, D. E. *Eur. J. Inorg. Chem.* **2010**, 3735.

(45)   Park, T. H.; Cychosz, K. A.; Wong-Foy, A. G.; Dailly, A.; Matzger, A. J. *Chem. Commun.* **2011**, *47*, 1452.

(46)   Accelrys Materials Studio, version 4.3; Accelrys Inc.: San Diego, CA. 2008.

(47)   Rappe, A. K.; Casewit, C. J.; Colwell, K. S.; Goddard, W. A.; Skiff, W. M. *J. Am. Chem. Soc.* **1992**, *114*, 10024.

(48)   Hibbe, F.; Chmelik, C.; Heinke, L.; Pramanik, S.; Li, J.; Ruthven, D. M.; Tzoulaki, D.; Kärger, J. *J. Am. Chem. Soc.* **2011**, *133*, 2804.

(49)   Heinke, L.; Kärger, J. *Phys. Rev. Lett.* **2011**, *106*.

Chapter 3

Non-interpenetrated IRMOF-8: synthesis, activation, and gas sorption[†]

3.1   Introduction

Despite surface areas exceeding 5000 m^2/g in microporous coordination polymers (MCPs),[1-4] many difficulties still exist in achieving sorption properties commensurate with theoretical expectations. Reasons cited for experimental surface areas falling short of values computed from ideal, guest-free crystallographic models include incomplete guest removal,[5,6] structural amorphitization[7,8] or transformation[9] upon guest removal, and interpenetration.[10] With the tremendous growth of the field, the need to understand and overcome these obstacles has become imperative. Our group[11,12] and others[10,13,14] have begun to analyze non-ideal behavior in MCPs in detail. In this work, we focus on IRMOF-8 ($Zn_4O(ndc)_3$, ndc = naphthalene-2,6-dicarboxylate),[15] one of the earliest examples of a material which, though expected to have an outstanding surface area based on its guest-free crystal structure, has yet to exhibit predicted gas sorption properties.

IRMOF-8 has a cubic structure constructed from the linkage of basic zinc acetate clusters and ndc ligands (Figure 3.1a). Soon after the initial report, it was scrutinized as a H_2 storage material.[16-20] However, the maximum excess H_2 uptake in this material is exceeded by the topologically identical materials IRMOF-1 and IRMOF-20,[21] a result at odds with that expected from their shorter linker lengths.[22] Researchers have proposed a number of reasons for the curious sorption behavior of IRMOF-8 including extra-framework zinc species,[17] incomplete activation,[18] and interpenetration.[19,23,24] Indeed, a number of interpenetrated phases of Zn_4O/ndc-based systems have been discovered,[25-27]

---

the syntheses of which are similar to that of IRMOF-8, lending credence to the possibility that typical solvothermally synthesized IRMOF-8 contains at least a significant amount of an interpenetrated phase. In this work, we report fully activated, non-interpenetrated IRMOF-8 and examine its sorption properties.

3.2   Results and Discussion

Initially, we synthesized IRMOF-8 using common solvothermal routes (hereafter denoted IRMOF-8-HT).[15,18] After activation by solvent exchange with CH_2Cl_2 and subsequent evacuation under reduced pressure (~10^{-2} Torr), a BET surface area of 1671 m^2/g was obtained (Figure 3.2a). Materials synthesized with dimethylformamide (DMF) or diethylformamide (DEF), as well as those activated using supercritical CO_2, exhibited similar surface areas. Thermogravimetric analysis (TGA) (Figure 3.3) of the activated samples revealed minimal mass loss, suggesting thorough removal of solvent on evacuation (though not discounting occluded non-volatile guests[10,28]). X-ray diffraction of the material before and after evacuation (Figure 3.4) indicates that bulk crystallinity is maintained; however, reflections in addition to those expected for phase-pure IRMOF-8 are observed (Figure 3.5). Previous reports[19,23,24] have suggested framework interpenetration as the primary cause for low surface area arising from these synthetic procedures. Indeed, comparison with a hypothetical ndc-based framework derived from the structure of IRMOF-9[23] (Figure 3.1b) shows only modest agreement with our experimental data. Although comparison with recently reported interpenetrated Zn/ndc-based systems[25-27] did not yield better agreement, it stands to reason that the low surface area of IRMOF-8-HT is due, at least in part, to the presence of one or more interpenetrated phases.

Incubation of ndc and $Zn(NO_3)_2 \cdot 4H_2O$ at room temperature in DEF[29] for one week afforded colorless ~100 micron truncated cubic crystals of high optical quality (hereafter denoted IRMOF-8-RT, Figure 3.6a). Analysis by powder X-ray diffraction (PXRD) showed excellent agreement with that simulated from the original crystal structure (Figure 3.6b).[15] However, upon solvent exchange with CH_2Cl_2 and subsequent evacuation, a relatively low BET surface area of 773 m^2/g was obtained. PXRD data of

the evacuated material are consistent with partial structural collapse, accounting for a surface area significantly lower than the calculated geometric accessible surface area[30] of 4350 m^2/g. Activation using supercritical CO_2[31] applied in a flow apparatus[32] yielded a BET surface area of 4461 m^2/g, an unusually high value for a material with simple cubic symmetry.[33] Characterization of IRMOF-8- RT by Ar sorption and subsequent NLDFT fitting (Figure 3.2b) yielded a surface area-weighted average pore size of 17.1 Å, closely matching the crystal structure pore size of 17.5 Å.[34] In contrast, IRMOF-8-HT Ar sorption data yielded a lower surface area-weighted average pore size of 11.0 Å, consistent with an interpenetrated material.

Given the consistency in N_2 and Ar sorption properties with theory, we elected to compare the hydrogen sorption properties of IRMOF-8-RT with previous reports on related materials.[16,18,35,36] The H_2 uptake at cryogenic temperatures between 0 and 1 bar is given in Figure 3.7a. The gravimetric uptake at 1 bar and 77 K is 12.3 mg/g (1.23 wt%), lower than previously reported values ranging from 14.5-15.2 mg/g under identical conditions; because the surface area of IRMOF-8-RT is dramatically greater than those of these other materials, the low uptake at 1 bar must be coupled with a lower isosteric heat of adsorption (Q_{st}). The Q_{st} for IRMOF-8-RT was determined using a modified Clausius-Clapeyron equation[37] (Figure 3.7b) by fitting the isotherms collected at 77 and 87 K to the Langmuir-Freundlich equation (Figure 3.8). Fits yielded values of 5.5 kJ/mol and 4.6 kJ/mol at low H_2 uptake and averaged over the examined pressure range, respectively (Figure 3.7b). These values are significantly lower than that previously determined for IRMOF-8 (6.1 kJ/mol),[18] a discrepancy that can be explained by the less constricted pores of IRMOF-8-RT. In this context, it is worth noting that other non-interpenetrated Zn_4O MCPs exhibit similarly low Q_{st} values: IRMOF-1, ~4-5 kJ/mol,[18,38] and UMCM-2, ~4.2 kJ/mol.[2]

The known isosteric heats of adsorption for all Zn_4O-based MCPs (including IRMOF-8-RT) are well below the range needed for optimal H_2 sorption at room temperature.[39,40] However, at 77 K the optimal range for Q_{st} is significantly lower as well. Too high a Q_{st} at cryogenic temperatures is detrimental for sorbate release due to significant uptake below the lowest operating pressure (~1-1.5 bar) of the pressure swing cycle.[39] In slit-pore carbons, a Q_{st} of ~6 kJ/mol leads to an ideal operating temperature of

41

115 K. Theory predicts that for a Q_{st} of ~4 kJ/mol for the same class of materials, an operating temperature of 77 K is ideal.[39] Hence, for H_2 storage and *delivery* at 77 K, physisorbents such as IRMOF-8-RT are in fact better suited than lower surface area, higher affinity materials.

3.3   Conclusions

In summary, the gap between experimental and theoretical porosity in IRMOF-8 has been bridged. A high surface area in excess of 4400 m^2/g was obtained, and the pore size distribution and powder diffraction data are in excellent agreement with expectations based on crystallography. Cryogenic H_2 sorption data between 0 and 1 bar yields a modest heat of adsorption consistent with that obtained for other Zn_4O-based MCPs, which may in fact be advantageous for *deliverable* hydrogen at cryogenic temperatures.

3.4   Experimental Methods

Starting reagents. Zinc nitrate hexahydrate (Fisher Scientific, ACS grade), naphthalene-2,6-dicarboxylic acid (H_2ndc, TCI, >98%), dichloromethane (Fisher Scientific, >99.9%), and dimethylformamide (DMF, Fisher Scientific, >99.5%) were used as-received without further purification. Diethylformamide (DEF, TCI, >99.0%) was purified by storing over activated carbon for ~1 month and subsequently passing through a column containing silica gel. DEF was used within one month of purification in this manner.

Zinc nitrate tetrahydrate, $Zn(NO_3)_2 \bullet 4H_2O$. Zinc nitrate hexahydrate (~25 g) was placed in a Schlenk flask and exposed to dynamic vacuum (10^{-2} Torr) for 24 h, collected, and stored in a desiccator. Water content was assessed periodically by thermogravimetric analysis and maintained at a mol ratio below 4.5:1 H_2O:Zn.

IRMOF-8-HT. A mixture of 0.21 g (0.80 mmol) $Zn(NO_3)_2 \bullet 4H_2O$ and 0.050 g (0.23 mmol) H_2ndc was dissolved in 10 mL DEF by sonication in a 20 mL scintillation vial. The solution was then incubated at 85 °C for ~36 h, after which time pale yellow crystal clusters formed. The vial was cooled to room temperature, and the solid was

rinsed three times over 24 h with fresh DMF and subsequently four times over two days with CH_2Cl_2. The solid was finally dried under reduced pressure (10^{-2} Torr) and stored in a N_2 glovebox until analysis. Materials made with DMF were produced identically, but replacing DEF with an equal volume of DMF. The yield of the dry, activated sample is 33%, based on H_2ndc.

IRMOF-8-RT. A procedure modified from a previous preparation[29] was used. A mixture of 2.18 g (8.83 mmol) $Zn(NO_3)_2\cdot4H_2O$ and 0.240 g H_2ndc (1.11 mmol) was dissolved in 200 mL DEF by sonication in a 400 mL jar. Ten microscope slides were placed upright in a home-built holder in solution to afford additional sites for crystal growth and simplify collection of strongly adherent crystals. The solution was incubated at room temperature for 7 days, after which time ~100 μm diameter clear, truncated cubic crystals had grown on the slides and walls of the jar. The crystals were collected and rinsed four times with fresh DMF over 24 h. The material was activated using supercritical CO_2[31] with a flow-through apparatus (see below) and stored in a N_2 glovebox until analysis. The average yield as determined from six preparations of the dry, activated sample is 20%, based on H_2ndc.

Supercritical CO_2 activation. Samples were activated by flowing supercritical CO_2. The method has been described in detail elsewhere.[41]

Powder X-ray diffraction. Powder X-ray diffraction data were collected with a Bruker D8 Advance diffractometer having a Bragg-Brentano geometry. The Cu-Kα (1.5406 Å) X-ray radiation source was operated at 40 V and 40 mA. Samples were ground in a mortar and pestle and evenly dispersed on a low-background quartz plate with a cavity depth of 0.3 mm (The Gem Dugout, State College, Pennsylvania, USA) in a N_2 glovebox. Samples were then transferred to the diffractometer and analyzed under ambient conditions and low relative humidity (<25%). Stability of the analyte under measurement conditions was confirmed by comparing rapid (0.1 sec./step) scans obtained immediately after exposure of the analyte to ambient conditions and comparing them with data obtained with slower, higher resolution scans (2-3 sec./step).

Gas sorption measurements. Sorption experiments were carried out using an Autosorb 1C (Quantachrome Instruments, Boynton Beach, Florida, USA). He (99.999%, used to determine void volumes), N_2 (99.999%), Ar (99.999%), and H_2 (99.999%) were

purchased from Cryogenic Gases and used as received. For N_2 and Ar measurements, a glass sample cell was charged with 20 mg sample and analyzed at 77 and 87 K, respectively. For analysis of H_2 uptake, 103 mg of sample was added to a glass sample cell. A glass rod of diameter slightly smaller than the inner diameter of the sample cell was inserted into the cell to minimize dead volume. The sample was then analyzed at 77 and 87 K.

Surface areas were obtained using the BET method following the consistency criteria introduced by Rouquerol[42] and applied to MCPs by Snurr.[43] Consistency criteria plots and BET plots are given in Figure 3.9 and Figure 3.10, respectively.

Ar pore size distributions were using NLDFT methods available in NovaWin 9.0 (Quantachrome Instruments). It is noted that the fit for IRMOF-8-RT showed poor fitting between 0.02 and 0.08 P/P_0 (Figure 3.11).

Thermogravimetric Analysis. A TA Instruments Q50 TGA was used to obtain thermogravimetric data. Activated analyte (5 mg) was heated and analyzed in a platinum pan under a dry nitrogen atmosphere.

3.5   Figures
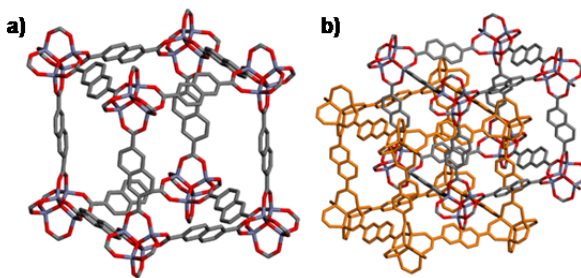
Figure 3.1. Structures of a) IRMOF-8 and b) interpenetrated IRMOF-8 analogue. Blue = Zn, red = O, grey = C. Hydrogen atoms omitted for clarity.
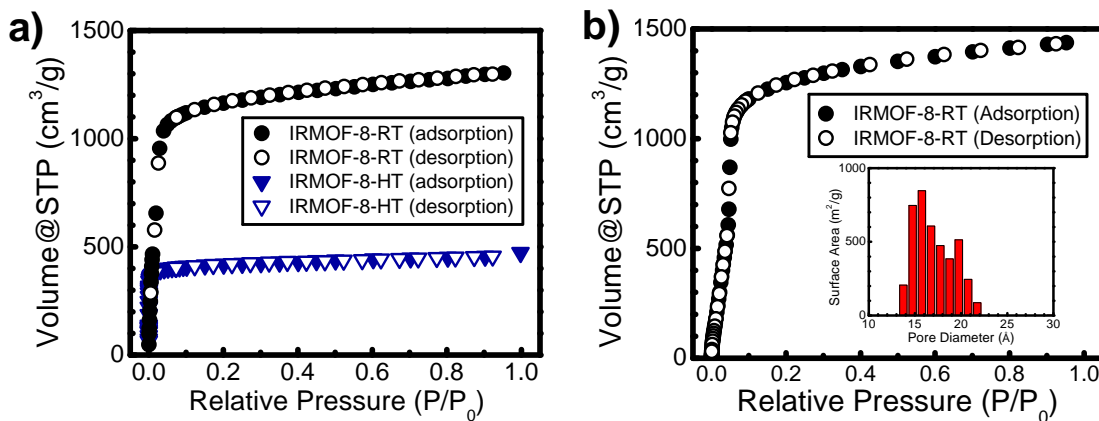
Figure 3.2. a) N_2 isotherms of IRMOF-8-HT (blue triangles) and IRMOF-8-RT (black circles). b) Ar isotherm of IRMOF-8-RT. Inset: Pore size distribution from NLDFT fit.
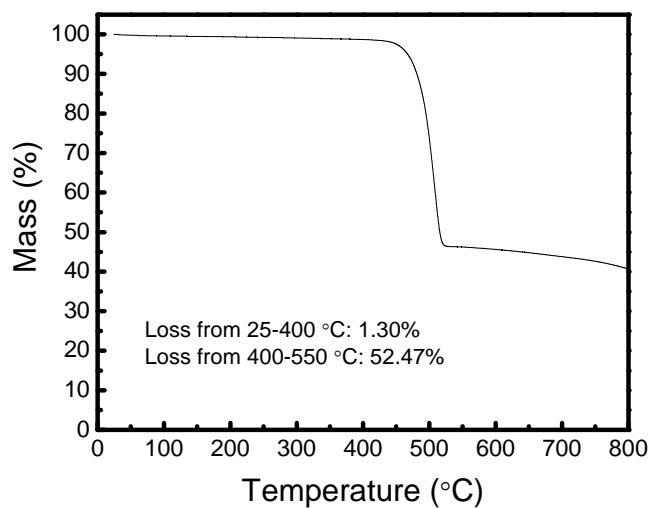
Figure 3.3. Thermogravimetric analysis of IRMOF-8-HT under a N_2 atmosphere after solvent removal.
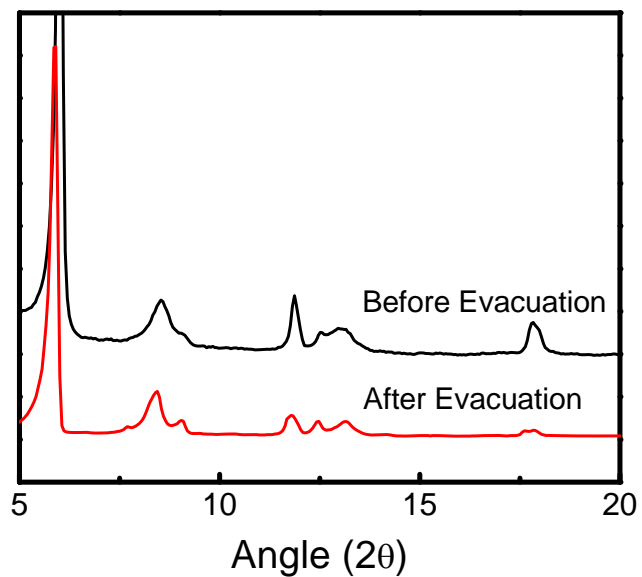
Figure 3.4. PXRD pattern of IRMOF-8-RT immediately before and after evacuation.
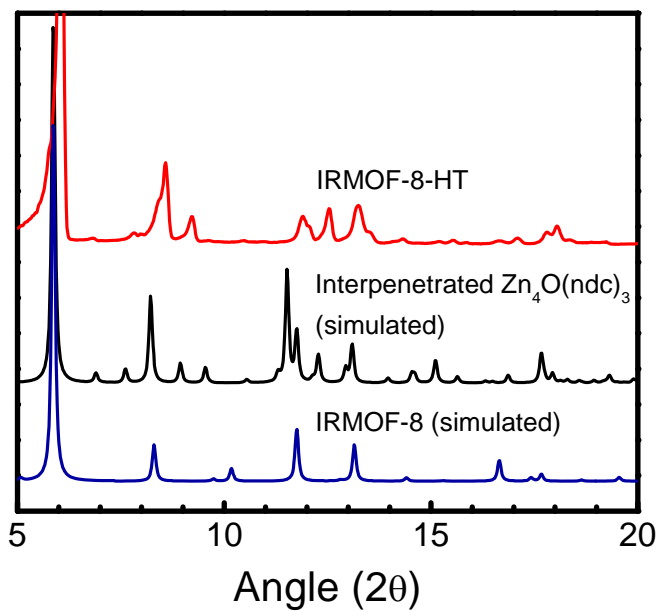
Figure 3.5. PXRD pattern of IRMOF-8-HT compared with the simulated diffractograms of IRMOF-8 and a hypothetical model of interpenetrated IRMOF-8[23] (based on the interpenetration mode of IRMOF-9).
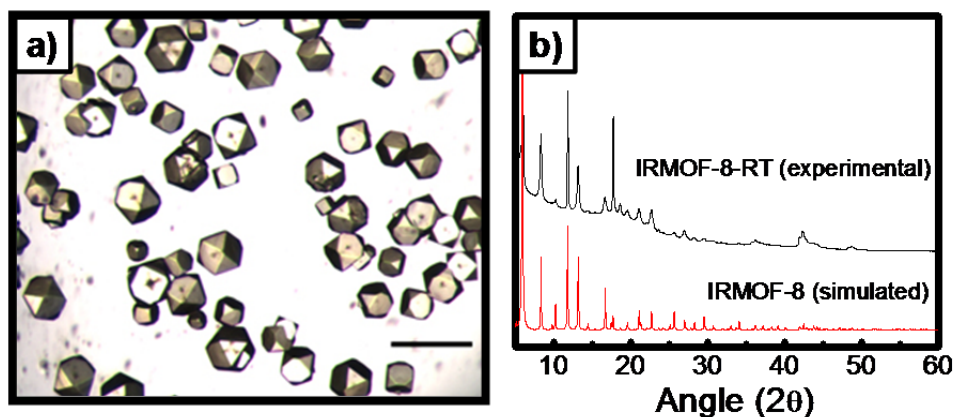
Figure 3.6. a) Optical micrograph of crystals of IRMOF-8-RT immediately after synthesis. Scale bar = 500 μm. b) Powder X-ray diffractogram of IRMOF-8-RT after supercritical CO_2 activation.
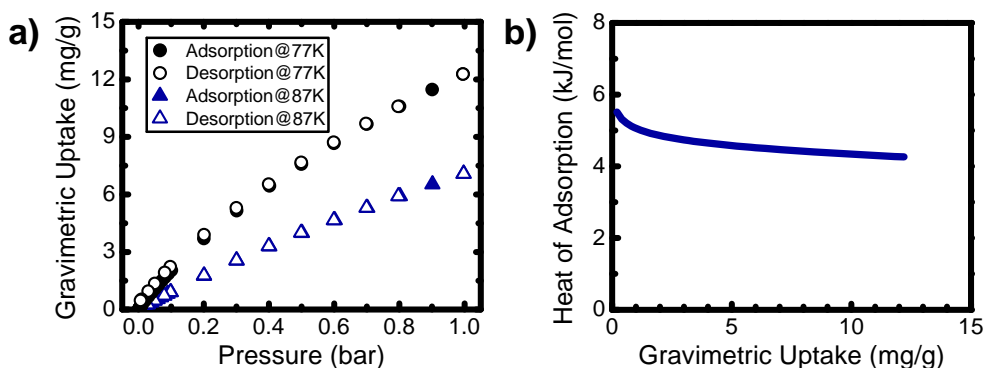
Figure 3.7. a) H_2 isotherms of IRMOF-8-RT at 77 and 87 K. b) Isoteric heat of adsorption for H_2 uptake in IRMOF-8-RT.

Langmuir-Freundlich fit parameters	
77 K	87 K
M = 19.3592	M = 19.3876
B = 0.0010025	B = 0.000361297
t = 1.08266	t = 1.03357
R^2 = 0.999993	R^2 = 0.999995
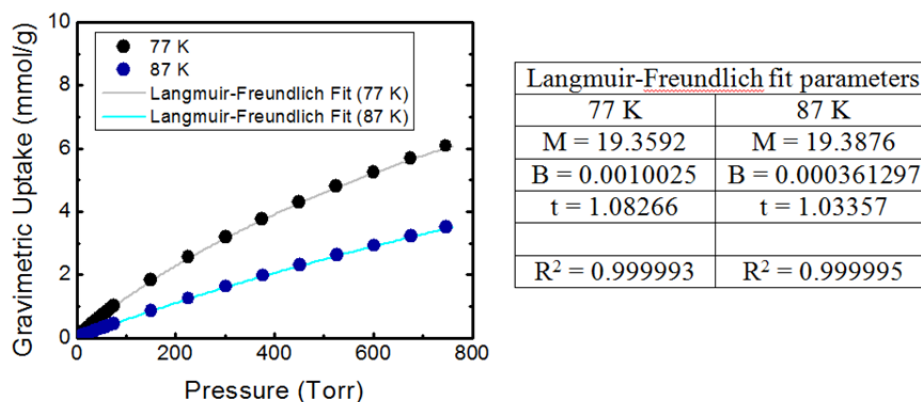
Figure 3.8. Langmuir-Freundlich fits of IRMOF-8-RT H_2 sorption data at 77 and 87 K.
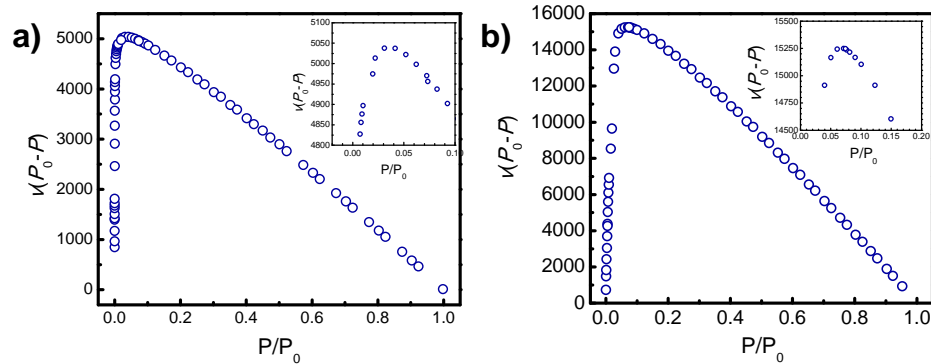
Figure 3.9. Determination of BET plot range for a) IRMOF-8-HT and b) IRMOF-8-RT based on consistency criteria.[42,43]
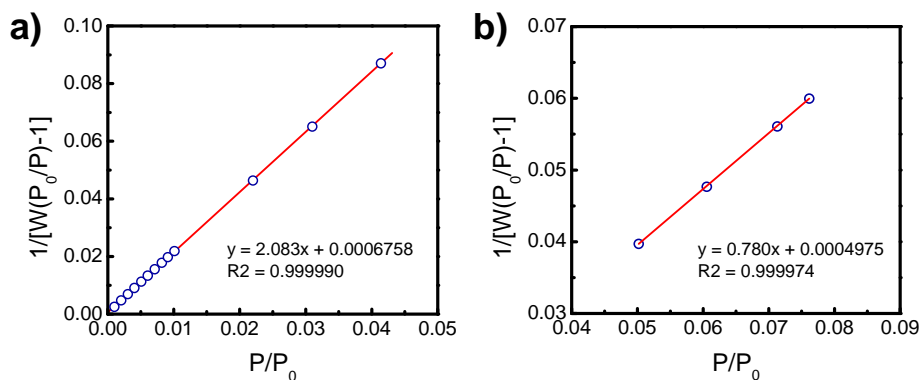
Figure 3.10. a) BET plot for a) IRMOF-8-HT and b) IRMOF-8-RT. The maximum points were chosen by the consistency criteria (Figure 3.9). For IRMOF-8-RT, inclusion of points at P/P_0 values below 0.05 resulted in poorer fits to the data.
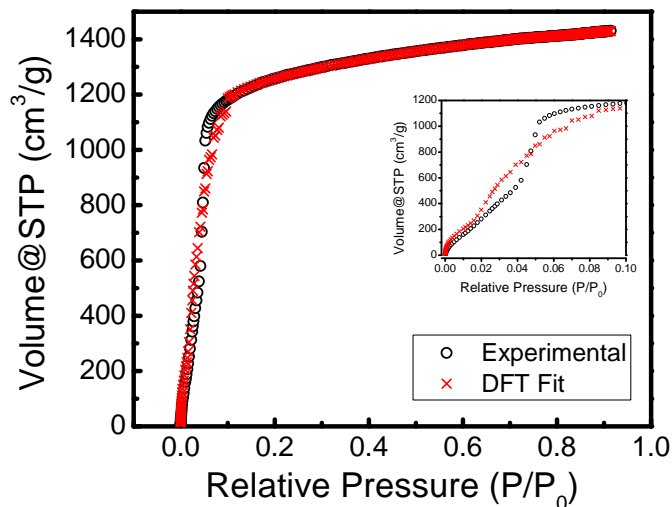
Figure 3.11. NLDFT model of Ar isotherm for IRMOF-8-RT based on a kernel for zeolites and silica with cylindrical pores. Inset shows poor fitting between 0.02 and 0.08 P/P_0, yielding some uncertainty in the pore size distribution (see Figure 3.2, inset). No more accurate NLDFT model was available.

3.6   References

(1)   Furukawa, H.; Ko, N.; Go, Y. B.; Aratani, N.; Choi, S. B.; Choi, E.; Yazaydin, A. Ö.; Snurr, R. Q.; O'Keeffe, M.; Kim, J.; Yaghi, O. M. *Science* **2010**, *329,* 424.

(2)   Koh, K.; Wong-Foy, A. G.; Matzger, A. J. *J. Am. Chem. Soc.* **2009**, *131*, 4184.

(3)   Farha, O. K.; Yazaydin, A. Ö.; Eryazici, I.; Malliakas, C. D.; Hauser, B. G.; Kanatzidis, M. G.; Nguyen, S. T.; Snurr, R. Q.; Hupp, J. T. *Nat. Chem.* **2010**, *2*, 944.

(4)   Yuan, D.; Zhao, D.; Sun, D.; Zhou, H.-C. *Angew. Chem., Int. Ed.* **2010**, *49*, 5357.

(5)   Llewellyn, P. L.; Bourrelly, S.; Serre, C.; Vimont, A.; Daturi, M.; Hamon, L.; De Weireld, G.; Chang, J.-S.; Hong, D.-Y.; Hwang, Y. K.; Jhung, S. H.; Férey, G. *Langmuir* **2008**, *24*, 7245.

(6)   Wade, C. R.; Dincă, M. *Dalton Trans.* **2012**, *41*, 7931.

(7)   Ma, L. Q.; Jin, A.; Xie, Z. G.; Lin, W. B. *Angew. Chem. Int. Ed.* **2009**, *48*, 9905.

(8)   Kitagawa, S.; Kondo, M. *Bull. Chem. Soc. Jpn.* **1998**, *71*, 1739.

(9)   Seo, J.; Bonneau, C.; Matsuda, R.; Takata, M.; Kitagawa, S. *J. Am. Chem. Soc.* **2011**, *133*, 9005.

(10)   Hafizovic, J.; Bjørgen, M.; Olsbye, U.; Dietzel, P. D. C.; Bordiga, S.; Prestipino, C.; Lamberti, C.; Lillerud, K. P. *J. Am. Chem. Soc.* **2007**, *129*, 3612.

(11)   Liu, M.; Wong-Foy, A. G.; Vallery, R. S.; Frieze, W. E.; Schnobrich, J. K.; Gidley, D. W.; Matzger, A. J. *Adv. Mater.* **2010**, *22*, 1598.

(12)   Feldblyum, J. I.; Liu, M.; Gidley, D. W.; Matzger, A. J. *J. Am. Chem. Soc.* **2011**, *133*, 18257.

(13)   Hibbe, F.; Chmelik, C.; Heinke, L.; Pramanik, S.; Li, J.; Ruthven, D. M.; Tzoulaki, D.; Kärger, J. *J. Am. Chem. Soc.* **2011**, *133*, 2804.

(14)   Tsao, C.-S.; Yu, M.-S.; Chung, T.-Y.; Wu, H.-C.; Wang, C.-Y.; Chang, K.-S.; Chen, H.-L. *J. Am. Chem. Soc.* **2007**, *129*, 15997.

(15)   Eddaoudi, M.; Kim, J.; Rosi, N.; Vodak, D.; Wachter, J.; O'Keeffe, M.; Yaghi, O. M. *Science* **2002**, *295*, 469.

(16)   Rowsell, J. L. C.; Millward, A. R.; Park, K. S.; Yaghi, O. M. *J. Am. Chem. Soc.* **2004**, *126*, 5666.

(17)   Rowsell, J. L. C.; Eckert, J.; Yaghi, O. M. *J. Am. Chem. Soc.* **2005**, *127*, 14904.

(18)   Dailly, A.; Vajo, J. J.; Ahn, C. C. *J. Phys. Chem. B* **2006**, *110*, 1099.

(19)   Panella, B.; Hönes, K.; Müller, U.; Trukhan, N.; Schubert, M.; Pütter, H.; Hirscher, M. *Angew. Chem. Int. Ed.* **2008**, *47*, 2138.

(20)   Orefuwa, S. A.; Yang, H.; Goudy, A. J. *Microporous Mesoporous Mater.* **2012**, *153*, 88.

(21)   Wong-Foy, A. G.; Matzger, A. J.; Yaghi, O. M. *J. Am. Chem. Soc.* **2006**, *128*, 3494.

(22)   Schnobrich, J. K.; Koh, K.; Sura, K. N.; Matzger, A. J. *Langmuir* **2010**, *26*, 5808.

(23)   Rowsell, J. L. C. Hydrogen Storage in Metal-Organic Frameworks: An Investigation of Structure-Property Relationships. Ph.D. Dissertation, University of Michigan, Ann Arbor, **2005**.

(24)   Siberio-Pérez, D. Y.; Wong-Foy, A. G.; Yaghi, O. M.; Matzger, A. J. *Chem. Mater.* **2007**, *19*, 3681.

(25)   Yao, Q.; Su, J.; Cheung, O.; Liu, Q.; Hedin, N.; Zou, X. *J. Mater. Chem.* **2012**, *22*, 10345.

(26)   Das, M. C.; Xu, H.; Wang, Z.; Srinivas, G.; Zhou, W.; Yue, Y.-F.; Nesterov, V. N.; Qian, G.; Chen, B. *Chem. Commun.* **2011**, *47*, 11715.

(27)   Perry IV, J. J.; Feng, P. L.; Meek, S. T.; Leong, K.; Doty, F. P.; Allendorf, M. D. *J. Mater. Chem.* **2012**, *22*, 10235.

(28)   Feng, P. L.; Perry, J. J.; Nikodemski, S.; Jacobs, B. W.; Meek, S. T.; Allendorf, M. D. *J. Am. Chem. Soc.* **2010**, *132*, 15487.

(29)   *US Pat.*, 0 192 175, 2005.

(30)   Düren, T.; Millange, F.; Férey, G.; Walton, K. S.; Snurr, R. Q. *J. Phys. Chem. C* **2007**, *111*, 15350.

(31)   Nelson, A. P.; Farha, O. K.; Mulfort, K. L.; Hupp, J. T. *J. Am. Chem. Soc.* **2009**, *131*, 458.

(32)   Koh, K.; Van Oosterhout, J. D.; Roy, S.; Wong-Foy, A. G.; Matzger, A. J. *Chem. Sci.* **2012**, *3*, 2429.

(33)   More generally, many cubic networks are prone to interpenetration or collapse, although these obstacles have been overcome with node desymmetrization as in UMCM-8/UMCM-9[32] or adroit choice of net as in the (3,24)-connected *rht* net, as exemplified in MCPs by Zaworotko,[44] Lah,[45] and Zhou.[4]

(34)   Pore size was determined from an idealized version of CSD deposition number 175579 with Monte Carlo techniques (L. D. Gelb and K. E. Gubbins, *Langmuir*, **1999**, *15*, 305) using PSDSolv (S. Bhattacharya and K. E. Gubbins, *Langmuir*, **2006**, *22*, 7726).

(35)   Rosi, N. L.; Eckert, J.; Eddaoudi, M.; Vodak, D. T.; Kim, J.; O'Keeffe, M.; Yaghi, O. M. *Science* **2003**, *300*, 1127.

(36)   Krawiec, P.; Kramer, M.; Sabo, M.; Kunschke, R.; Fröde, H.; Kaskel, S. *Adv. Eng. Mater.* **2006**, *8*, 293.

(37)   Dincă, M.; Long, J. R. *J. Am. Chem. Soc.* **2005**, *127*, 9376.

(38)   Zhou, W.; Wu, H.; Hartman, M. R.; Yildirim, T. *J. Phys. Chem. C* **2007**, *111*, 16131.

(39)   Bhatia, S. K.; Myers, A. L. *Langmuir* **2006**, *22*, 1688.

(40)   Bae, Y.-S.; Snurr, R. Q. *Microporous Mesoporous Mater.* **2010**, *132*, 300.

(41)   Liu, B.; Wong-Foy, A. G.; Matzger, A. J. *Chem. Commun.* **2013**, *49*, 1419.

(42)   Rouquerol, J.; Llewellyn, P.; Rouquerol, F. In *Characterization of Porous Solids VII - Proceedings of the 7th International Symposium on the Characterization of Porous Solids*; Llewellyn, P. L., Rodriquez Reinoso, F., Rouqerol, J., Seaton, N., Eds. 2007; Vol. 160, p 49.

(43)   Walton, K. S.; Snurr, R. Q. *J. Am. Chem. Soc.* **2007**, *129*, 8552.

(44)   Nouar, F.; Eubank, J. F.; Bousquet, T.; Wojtas, L.; Zaworotko, M. J.; Eddaoudi, M. *J. Am. Chem. Soc.* **2008**, *130*, 1833.

(45)   Zou, Y.; Park, M.; Hong, S.; Lah, M. S. *Chem. Commun.* **2008**, 2340.

Chapter 4

Interpenetration, Porosity, and High-Pressure Gas Adsorption in $Zn_4O(2,6$-naphthalene dicarboxylate$)_3$[†]

4.1   Introduction

The study of microporous coordination polymers (MCPs) has been fueled by the promise of their utility in gas sorption applications, in particular hydrogen/methane storage and delivery[1,2] and carbon dioxide capture.[3] The rational optimization of these materials for sorption applications is made possible due to the relative ease with which they can be designed. The design principles elegantly delineated by Robson and coworkers in their pioneering work of the early 1990's[4] demonstrated that by using organic ligands (typically termed "linkers" in the more recent literature) and metals with geometrically defined preference for assembly, open structures could be produced to mimic known solid-state networks such as diamond[4] or PtS.[5] Shortly thereafter it was demonstrated that chemical functionalization or increasing ligand length would lead to chemically tunable or expanded lattices with identical topology.[5] Indeed, the concept of increasing linker length while maintaining geometry has become a well-known strategy to reduce density and increase surface area of topologically identical coordination polymers.[6,7]

Despite the many successful examples of MCPs-by-design, predicted structures have often proven difficult to obtain experimentally. Obstacles such as interpenetration,[8,9] unexpected or unpredictable coordination geometries,[10] or interference with structure formation by the presence of incompatible functional groups[11-13] or steric bulk[14] can lead

---

to materials with disappointing properties such as lower-than-expected surface areas or low degrees of crystallinity. Arguably, in no set of isostructural MCPs are these obstacles more evident than in the IRMOF-series.[15] This is a set of simple cubic-structured MCPs based on Zn_4O clusters linked together by linear dicarboxylates. IRMOF-1 (originally and more commonly termed MOF-5, $Zn_4O(bdc)_3$, bdc = 1,4-benzene dicarboxylate)[16] exhibits surface areas typically between 3000 and 3500 m^2/g.[15,17] Surface area in MCPs can be related to the mass ratio of organic component to metal cluster and the accessibility of these components by adsorbates.[6] Thus, using a longer p-phenylene-based linker (such as 4,4′-biphenyldicarboxylate as in IRMOF-10 or 4,4″-terphenyldicarboxylate as in IRMOF-16) would be expected to yield a material having higher surface area.[6] In practice, IRMOF-10[18] and IRMOF-16,[19] as well as the extended-linker IRMOF-12[15] and IRMOF-14,[15] have exhibited surface areas significantly lower than those predicted from crystallographic models. IRMOF-8[20-32] also exhibited similarly low surface areas until our recent findings.[33] Obstacles such as interpenetration, pore collapse upon guest removal, or non-volatile occluded guests may be responsible for these inconsistencies between theory and experiment. However, developing a deeper understanding of such inconsistencies is hampered by the use of traditional probes of porous materials such as gas sorption and X-ray diffraction because they are averaging techniques insensitive to defects.

We have recently demonstrated the utility of positron annihilation lifetime spectroscopy (PALS) to probe defects,[34] degradation,[35] and pore architecture during gas sorption[35] in MCPs. PALS operates on the principle that the average annihilation lifetime of positronium (the bound state of a positron and an electron) in an empty pore is directly related to the size of that pore. Positronium is formed throughout a porous solid upon exposing that solid to high-energy positrons that burrow deep within it. Positronium is formed from the interaction between implanted positrons and electrons present within the material, allowing the detection of buried pores and local disorder where other porosimetry methods often fall short. Detailed reviews of the technique are available.[36,37] Given the numerous examples[20-32,38] of a material derived from Zn_4O metal clusters and ndc (ndc = 2,6-naphthalene dicarboxylate) and referred to as IRMOF-8, but having surface areas typically between 1000-2000 m^2/g (significantly lower than the predicted

geometric accessible surface area[39] of 4350 m^2/g), and considering previous speculation that interpenetration led to such deviation from crystallographic expectation,[21,25,40,41] we sought to determine the cause of the low surface area in this material using PALS. During our investigations, we discovered an approach to synthesize and activate high surface area, phase-pure IRMOF-8.[33] In the present work, we provide conclusive evidence that attempts at synthesizing IRMOF-8 under typical solvothermal conditions leads to an interpenetrated analogue. Furthermore, we investigate the high pressure methane and hydrogen storage sorption properties of non-interpenetrated IRMOF-8.

4.2   Experimental Section

Materials. All reagents were obtained from commercial vendors and used as-received unless otherwise noted. *N,N*-Diethylformamide (DEF) was purified by storing over activated carbon for a minimum of 1 month and subsequently passing through a silica gel column before use. Purified DEF was used within one month or until the solvent color changed from colorless to pale yellow by visual inspection. To obtain Zn(NO$_3$)$_2$•4H$_2$O, powdered Zn(NO$_3$)$_2$•6H$_2$O was subjected to reduced pressure (~20 mTorr) for 24 h. Water content was assessed by thermogravimetric analysis (TGA). Both IRMOF-8 and interpenetrated analogues were prepared and activated as previously described[33] unless otherwise noted.

Gas sorption measurements. N$_2$ sorption isotherms were obtained on a NOVA4200E (Quantachrome Instruments) gas sorption analyzer. An activated sample (~40-50 mg) was added to a long-stem glass sample cell in a N$_2$ glove box and subsequently transferred to the sorption apparatus for measurement. Samples were analyzed at 77 K using 99.999% purity N$_2$ (Cryogenic Gases). Ar sorption isotherms were obtained on an Autosorb 1C (Quantachrome) gas sorption analyzer. An activated sample (~30 mg) was charged into a long-stem glass sample cell in a N$_2$ filled glove box and subsequently transferred to the sorption apparatus for measurement. Samples were analyzed at 87 K using 99.999% purity Ar (Cryogenic Gases). Excess H$_2$ sorption isotherms were obtained using a volumetric Sieverts' apparatus (Hy-Energy LLC PCT-Pro 2000). Samples (~200 mg) were cooled to 77 K by immersing the sample cell in a

liquid N_2 bath. He gas (99.999% purity, Airgas Inc.) was used to determine the cell volume and the dead space volume of the sample-filled cell at room temperature. H_2 gas of 99.999% purity (Airgas Inc.) was used for sorption analysis. Excess CH_4 sorption isotherms were collected on an HPA-100 High Pressure Analyzer (VTI Corporation) at 295 K using 99.99% purity CH_4 (Air Products). Activated sample (~250 mg) was charged into a stainless steel sample cell in a N_2 filled glove box and transferred to the sorption apparatus for analysis. The void volume of the cell was determined by He expansion from the dosing manifold into the sample cell. Compression factors of the gases (Z_{He}, Z_{CH4}) both in the dosing manifold and in the sample cell were determined using the NIST Reference Fluid Thermodynamic and Transport Properties (REFPROP version 7.0) incorporated into the HPA-100 software. A CH_4 isotherm was then constructed from adsorption data collected from 0-60 bar and from desorption data from 47-5 bar.

Positron annihilation lifetime spectroscopy (PALS). MCPs were loaded in an inert atmosphere N_2 glove box into a home-built sample holder having a one-sided ~1 μCi ^{22}Na positron source. The sample holder was subsequently sealed and connected to a stainless steel apparatus capable of pressures between 10^{-5} and 2×10^3 psi. Further details on data collection and analysis have been described previously.[34]

Computation. Geometric accessible surface areas were obtained by the method described by Düren et al.[39] A slightly modified version of the originally reported structure of IRMOF-8[15] was used, where solvent was removed and single-site occupancy was assigned to the organic linkers before computational analysis. Pore sizes were determined from guest-free structures using PSDSolv, a Monte Carlo-based method that provides a pore size distribution using spherical probes.[42,43]

4.3   Results and Discussion

The initial objective of this work is to elucidate the origin of the low surface area of $Zn_4O(ndc)_3$ synthesized at elevated temperatures. When synthesized at 85 °C (hereafter denoted IRMOF-8-HT), a precipitate of cubes and cube clusters is formed after 36 h (Figure 4.1). Previous reports on $Zn_4O(ndc)_3$ synthesized solvothermally both in

N,*N*-dimethylformamide (DMF)[22,29,31,32,38] or DEF[24,26-28,30,33] at temperatures ranging from 85 to 130 °C have presented surface areas between 1000 and 2000 m^2/g: values less than half of that expected from the geometric accessible surface area calculated from the originally reported[15] crystal structure. Indeed, when activated under reduced pressure (~20 mTorr) after solvent exchange with CH_2Cl_2, N_2 sorption indicates a relatively low BET surface area of 1606 m^2/g (Figure 4.2). Activation by flowing supercritical CO_2[44] led to a similar BET surface area (Figure 4.3). Examination of the powder X-ray diffraction (PXRD) data (Figure 4.4) of both as-synthesized and evacuated material shows reflections that are not present in the simulated PXRD pattern of the ideal, non-interpenetrated IRMOF-8; furthermore, these reflections do not match those present in the simulated powder patterns of other known Zn/ndc-based systems (Figure 4.5). We do note a significant resemblance between the powder patterns of IRMOF-8-HT after activation under reduced pressure and that of a previously proposed, hypothetical interpenetrated analogue[21] of IRMOF-8 (Figure 4.4, and as discussed previously[33]). As we were not able to obtain crystals suitable for single crystal X-ray diffraction, and no hypothetical model was found to provide a better-matching simulated PXRD pattern, we sought other methods that might lend insight into the potentially interpenetrated nature of IRMOF-8-HT.

Ar sorption of IRMOF-8-HT activated under reduced pressure indicates a fairly broad pore size distribution in the range of 0.7-1.5 nm (Figure 4.6). The pore diameter[42,43] calculated for the hypothetical interpenetrated IRMOF-8 analogue proposed by Rowsell[21] (based on the interpenetration mode of IRMOF-9) is 0.87 nm, at the low end of the range determined by NLDFT fitting of the 87 K Ar sorption isotherm. Although the small pores of the pore size distribution are in agreement with a hypothetical interpenetrated structure, the presence of pores up to 1.5 nm in diameter suggests that this specific interpenetrated framework model used cannot wholly account for the sorption characteristics of the bulk sample analyzed.

To assess the presence and extent of interpenetration in IRMOF-8-HT, PALS analysis was applied; this technique provides information on the size and population of pores in a material, even if those pores are inaccessible or otherwise undetected by gas sorption methods. The PALS spectrum of IRMOF-8-HT in vacuum is shown in Figure

4.7. Average lifetimes of 8.31 ± 0.12 and 16.48 ± 1.33 ns, derived from ortho-positronium (*o*-Ps) sampling the MCP, were obtained by fitting the PALS spectrum to a linear combination of exponential decays. A third lifetime of ~90 ns, arising from annihilation in the intergranular space between crystals, was also observed, indicative of *o*-Ps escaping from the interior of the analyte crystals (less precision is used for this third lifetime as it is variable depending on factors such as crystal grain size, and does not provide direct information on the pore characteristics of the analyte).[45] The two lifetimes observed for IRMOF-8-HT reveal the presence of two pores of different sizes. Since *o*-Ps readily diffuses throughout these materials (as evidenced by the presence of annihilation from the intergranular region), and as *o*-Ps tends to annihilate from the largest available pores,[36] the large and small pores must exist in spatially separated regions. If these pores were spatially well-mixed, only a single average lifetime would be observed. Pore sizes of 1.01 ± 0.01 and 1.41 ± 0.05 nm can be determined for the small and large pores, respectively, applying an extended[46,47] Tau-Eldrup[48,49] model and assuming[50] channel-like pores. These pore sizes may represent a lower limit of the true pore size, as the longest-lived *o*-Ps diffuses out of the crystal grains as evidenced by the ~10% of formed *o*-Ps annihilating in the intergranular space. The smaller of the two pore diameters determined from PALS is within 12% of the computationally determined pore diameter based on the largest *sphere* that can fit in the IRMOF-8-HT pores. This agreement is quite good given the assumptions in both the extended Tau-Eldrup model and in our determination of theoretical pore size. The larger MCP lifetime is likely due to the presence of some quantity of non-interpenetrated pores of the type proposed in the model of IRMOF-8[15] (discussed further below). The annihilation intensity, the relative contribution to the PALS spectrum of each lifetime component, provides an estimate of the relative population of each pore. The intensity is weighted toward larger pores, in which *o*-Ps is both more likely to form and more likely to diffuse into.[51] The intensities of 19.3% and 2.9% for small and large pores, respectively, are therefore consistent with a predominantly interpenetrated sample. As the Ar sorption isotherm of IRMOF-8-HT (and the resultant pore size distribution) shows little agreement with that of $Zn_4O(ndc)_3$ synthesized at room temperature (hereafter denoted IRMOF-8-RT), the minor component

of larger pores detected by PALS can be rationalized by incomplete interpenetration within otherwise interpenetrated grains.

The PALS spectrum of IRMOF-8-RT activated via flowing supercritical CO_2[44] (Figure 4.8) is strikingly different from that of IRMOF-8-HT (Figure 4.7). In this case, only one MCP lifetime is observed, 18.45 ± 0.26 ns. This lifetime corresponds to a channel-pore size of 1.49 ± 0.01 nm, in excellent agreement with the 1.50 nm cubic pore diameter determined geometrically from the original[15] crystal structure. Noting that detailed comparison of extended Tau-Eldrup-derived pore size and crystallographic dimension is a subject of ongoing investigation,[50] a conclusion consistent with the available data is that IRMOF-8-RT is free of interpenetration. An additional contribution from o-Ps annihilating in the intergranular space was detected, as expected given the open and interconnected pore space of the non-interpenetrated material.

Given the high BET surface area of IRMOF-8-RT (~4400 m^2/g[33]), the H_2 and CH_4 sorption properties of the material are of interest. Figure 4.9 shows the excess H_2 uptake of IRMOF-8-RT at 77 K and pressure up to 80 bar. We previously proposed[33] that the higher surface area, yet lower H_2 uptake at 1 bar and 77 K of IRMOF-8-RT compared with its (presumed) interpenetrated analogue meant that the maximum excess uptake *must* be higher in IRMOF-8-RT since maximum excess H_2 uptake has been shown to correlate well with the BET specific surface area.[17] Indeed, the maximum uptake is 6.36 wt% at 40.2 bar, nearly twice that of the maximum uptake previously observed (3.6 wt%) for what is likely an interpenetrated IRMOF-8 analogue.[24]

As we[33,52] and others[53-56] have previously emphasized, critical for the practical use of MCPs as sorbents for hydrogen fuels is the *deliverable* H_2 uptake. This value reflects the difference in uptake between the maximum excess and minimum practical operating pressure. The deliverable excess H_2 uptake for IRMOF-8-RT is given in Table 4. 1 along with that of a subset of representative MCPs for which data were available. The minimum pressure used for calculation of deliverable H_2 uptake vary widely in the literature; typical values for this lower limit are between 1-5 bar,[53-66] but values as high as 10 bar[67] have been used. Although the US Department of Energy target value is 3 bar,[68] data at this value is not available for most of the materials discussed herein, and hence, we were only able to make comparisons using a minimum deliverable pressure of 1 bar.

For future comparison, the deliverable uptakes of H_2 in IRMOF-8-RT using minima of 1 bar, 1.5 bar, 3 bar, and 5 bar are 5.13 wt%, 4.46 wt%, 3.51 wt%, and 2.70 wt%, respectively, resulting in deliverable fractions of maximum excess uptake of 81%, 70%, 55%, and 42%, respectively. These values were calculated using interpolation when necessary. IRMOF-8-RT shares similar excess H_2 sorption characteristics with the isostructural IRMOF-20; the higher surface area MOF-177 has a greater deliverable capacity, although the deliverable fraction of the maximum excess uptake (f_{deliv}) is similar for each of these materials. Likewise, the higher surface area, isostructural, Zn_4O-based SNU-70' has a nearly identical f_{deliv}.

Materials with higher affinity for H_2 due to the presence of coordinatively unsaturated metal sites or interpenetration show significantly lower f_{deliv} (for the specific (P, T) operating conditions discussed above) in comparison with IRMOF-8-RT. For MCPs with coordinatively unsaturated metal sites, most telling is the example of PCN-66;[7] despite having a higher maximum excess uptake than IRMOF-8-RT, the deliverable uptake is in fact *lower*. In NOTT-101,[69] the deliverable uptake is 30% lower than that of IRMOF-8-RT, despite having a maximum excess uptake only 5% less than that of the Zn-based MCP. Although in many cases high affinity does lead to low f_{deliv}, we now consider the case of the isostructural series of materials PCN-61, PCN-66, and PCN-68.[7] Each of these materials is constructed from hexatopic linkers connected by Cu paddlewheel clusters having coordinatively unsaturated metal sites. As maximum excess H_2 uptake (and surface area) increase, so does f_{deliv}, approaching the values more typical for the aforementioned low-affinity zinc-based MCPs. We rationalize this trend by considering the successively larger linkers of PCN-61, PCN-66, and PCN-68. The volumetric density of high-affinity coordinatively unsaturated metal sites in PCN-68 is smaller than that of PCN-61; hence, it behaves more as a low-affinity material in that f_{deliv} is quite high. Accordingly, the volumetric density of coordinatively unsaturated metal sites in PCN-66 lies in between those of PCN-61 and PCN-68, as does its f_{deliv}. Taken together, the isostructural series of PCN-61, PCN-66, and PCN-68 provides clear evidence that a higher f_{deliv} can be achieved by lowering the volumetric density of such high-affinity sorption sites. Finally, the interpenetrated IRMOF-11 illustrates the influence of catenation on deliverable excess H_2 uptake. Increased van der Waals

interactions due to the confined pore space enhances uptake below the deliverable minimum, resulting in a very low f_{deliv}. IRMOF-8-RT and related, non-interpenetrated Zn_4O-based materials, composed of low-affinity sorption sites throughout, have high f_{deliv}.

The excess CH_4 sorption isotherm for IRMOF-8-RT between 1 and 60 bar and 298 K is presented in Figure 4.10. The excess CH_4 uptake at 35 bar is 193 cm^3/g, corresponding to a volumetric uptake of 87 v/v, calculated with the crystal density of 0.448 g/cm^3. As in the case for H_2, minimum pressures for calculating deliverable CH_4 uptake vary, but are typically between 1-5 bar.[70-79] The deliverable gravimetric uptakes of CH_4 in IRMOF-8-RT using minima of 1 bar, 1.5 bar, 3 bar, and 5 bar and assuming a maximum working pressure of 35 bar are 185 cm^3/g, 182 cm^3/g, 171 cm^3/g, and 159 cm^3/g, respectively, resulting in deliverable fractions of 96%, 94%, 87%, and 82%, respectively. Corresponding deliverable volumetric uptakes at these pressures are 83 v/v, 81 v/v, 77 v/v, and 71 v/v, resulting in deliverable fractions of 95%, 93%, 89%, and 82%, respectively. These values were calculated by interpolation when necessary. Despite the high gravimetric uptake, the modest volumetric uptake at 35 bar is expected for a material with relatively large pores, given that the optimal pore size for volumetric storage is generally understood to be either 0.4 or 0.8 nm (dimensions allowing the adsorption of exactly one or exactly two CH_4 molecules, respectively[80,81]), and that optimal surface areas have empirically been estimated to lie in the 2500-3000 m^2/g range.[81]

To understand how CH_4 fills the pore space of the large-pore IRMOF-8-RT, we analyzed the material with PALS during CH_4 sorption at pressures ranging from 0 to 89.4 bar (Figure 4.11). The two datasets shown in Figure 4.11a are as-fitted o-Ps lifetime data and lifetime data corrected for the effects of collisional annihilation due to gas present within the pore, but not adsorbed to the pore walls. The corrected lifetime data shows how the o-Ps lifetime is influenced solely by CH_4 adsorbed within the pores, decreasing with increasing CH_4 pressure as would be expected for CH_4 adsorbed to the pore walls (the slight increase in lifetime at 0.76 bar is attributable to reduced escape of the longest-lived o-Ps from the MCP due to scattering from CH_4 gas, before reduction in o-Ps lifetime due to CH_4 adsorption overtakes this effect as at higher pressures[45]). The fraction

60

of the pore volume filled by CH_4 on increasing gas pressure, determined by subtracting the measured void volume at a given pressure from the void volume measured in vacuum, is given in Figure 4.11b. The exact fraction of occupied volume depends on the model (2D or 3D confinement of *o*-Ps) used to convert lifetime to pore diameter (and hence, volume), as discussed previously for the case of CO_2 adsorption in MOF-5.[35] At 35 bar, only 33-48% of the volume in the pores is utilized for adsorption. The volume filled by a single monolayer of CH_4 is estimated to be ~60%; consequently, adsorption at 35 bar in IRMOF-8-RT occurs at sub-monolayer coverage. This finding explains previous observations that specific surface area (which is defined at complete monolayer coverage) does not necessarily correlate with CH_4 uptake at 35 bar in MCPs.[7] At the highest pressures analyzed, only 50-64% of the pore volume is filled by adsorbed gas, and CH_4 uptake seems to level off at higher pressures. These data may suggest that at room temperature, and potentially at *any* temperature above the critical temperature, only monolayer coverage is achievable irrespective of pressure (within reasonable pressure limits for storage and delivery).

4.4   Conclusions

In this work we have shown that attempts at synthesizing IRMOF-8 at high temperatures in fact yield an interpenetrated analogue of the material. Analysis of bulk samples by PXRD, gas sorption, and PALS reveals data consistent with the presence of near-complete interpenetration. The high pressure H_2 and CH_4 sorption properties of high surface area, non-interpenetrated $Zn_4O(ndc)_3$ were also examined. H_2 uptake was determined to be consistent with expectations based on other Zn_4O-based materials. Importantly, the fraction of *deliverable* H_2 uptake was found to be above 80%, having a value shared by other MCPs with minimal H_2-sorbent interaction and in contrast to the low deliverable fraction calculated for MCPs with significant contributions from binding at coordinatively unsaturated metal sites or those displaying interpenetration. Despite high gravimetric CH_4 sorption, volumetric sorption in IRMOF-8-RT was low, a finding further illuminated by PALS. Only 33-48% of the pore volume is occupied by CH_4 at 35 bar, corresponding to sub-monolayer coverage. Even at pressures up to 90 bar, uptake

levels off and only monolayer coverage is achieved, suggesting that multi-layer adsorption of CH_4 is not operative in this material at room temperature. Taken together, these data suggest that successful synthesis and activation of IRMOFs with yet longer linkers and higher surface areas such as IRMOF-10 or IRMOF-16 may be possible, although even partial interpenetration may be an obstacle in maximizing the porosity of these materials. Given the low volumetric uptake of light gases expected for such materials having high gravimetric surface areas,[81] a combination of both linker extension and linker functionalization may be necessary to simultaneously maximize both gravimetric and volumetric uptake.

4.5   Figures
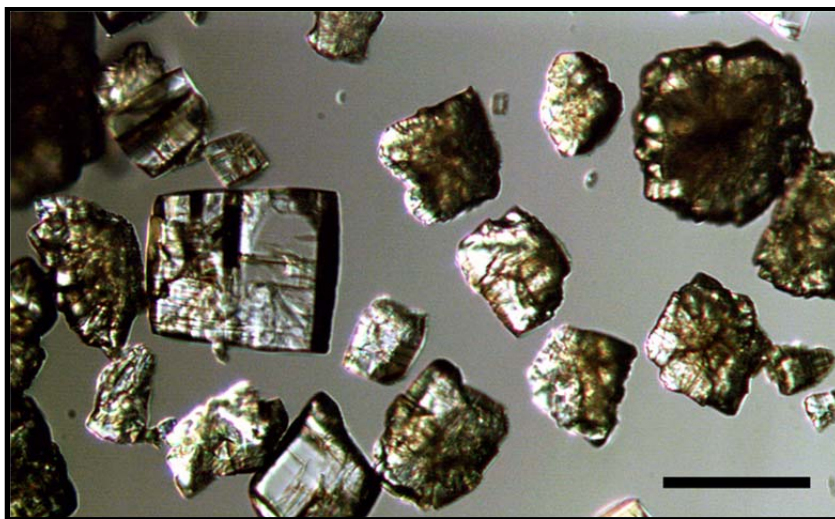
Figure 4.1. Optical micrograph of IRMOF-8-HT after cooling and rinsing three times with fresh *N,N*-dimethylformamide. Scale bar = 100 μm.
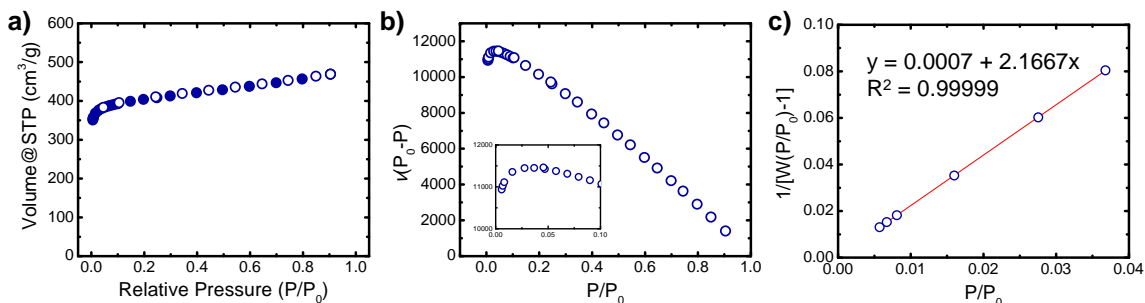
Figure 4.2. a) N_2 sorption isotherm of IRMOF-8-HT activated under reduced pressure (~20 mTorr). Filled and open circles represent adsorption and desorption, respectively. b) Consistency criterion plot[82,83] for determining P/P_0 range for BET analysis of IRMOF-8-HT based on isotherm in (a). Inset: detail of consistency criterion plot between 0 and 0.1 P/P_0. c) BET plot of IRMOF-8-HT using points below P/P_0 = 0.037. The BET surface area was determined to be 1606 m^2/g.
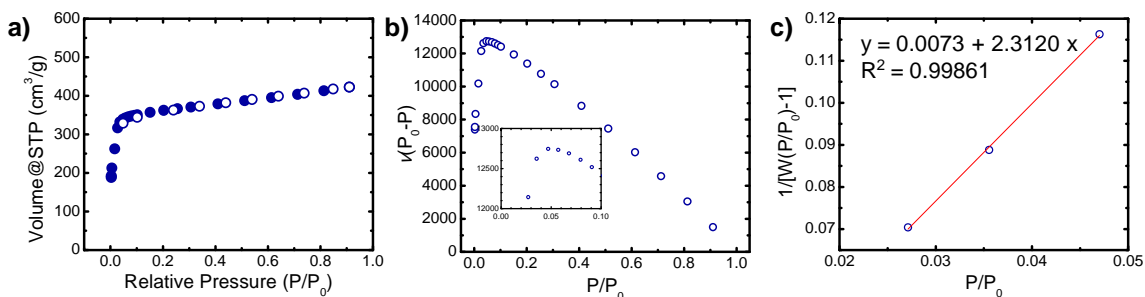
Figure 4.3. a) N_2 sorption isotherm of IRMOF-8-HT activated with supercritical CO_2. Filled and open circles represent adsorption and desorption, respectively. b) Consistency criterion plot to determine pressure range for BET analysis. Inset: pressure region between P/P_0 = 0 and 0.1. c) BET plot between P/P_0 = 0.27 and 0.47. Inclusion of lower pressure points led to poorer linear fits. The BET surface area was determined to be 1501 m^2/g.
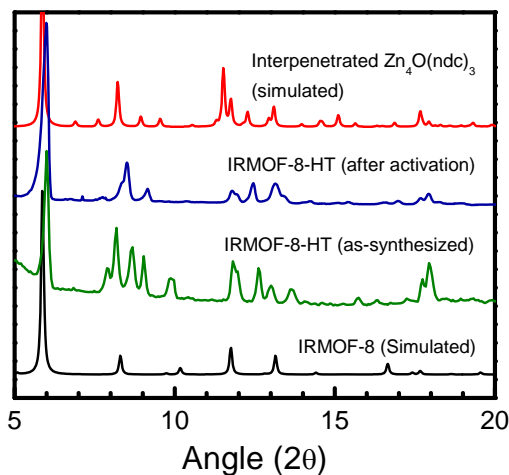
Figure 4.4. Powder X-ray diffractogram of IRMOF-8-HT as-synthesized and after activation under reduced pressure (~20 mTorr) compared with diffractogram simulated from the originally reported[15] crystal structure. The simulated interpenetrated $Zn_4O(ndc)_3$

diffractogram is from a hypothetical interpenetrated analogue of IRMOF-8 (see main text).
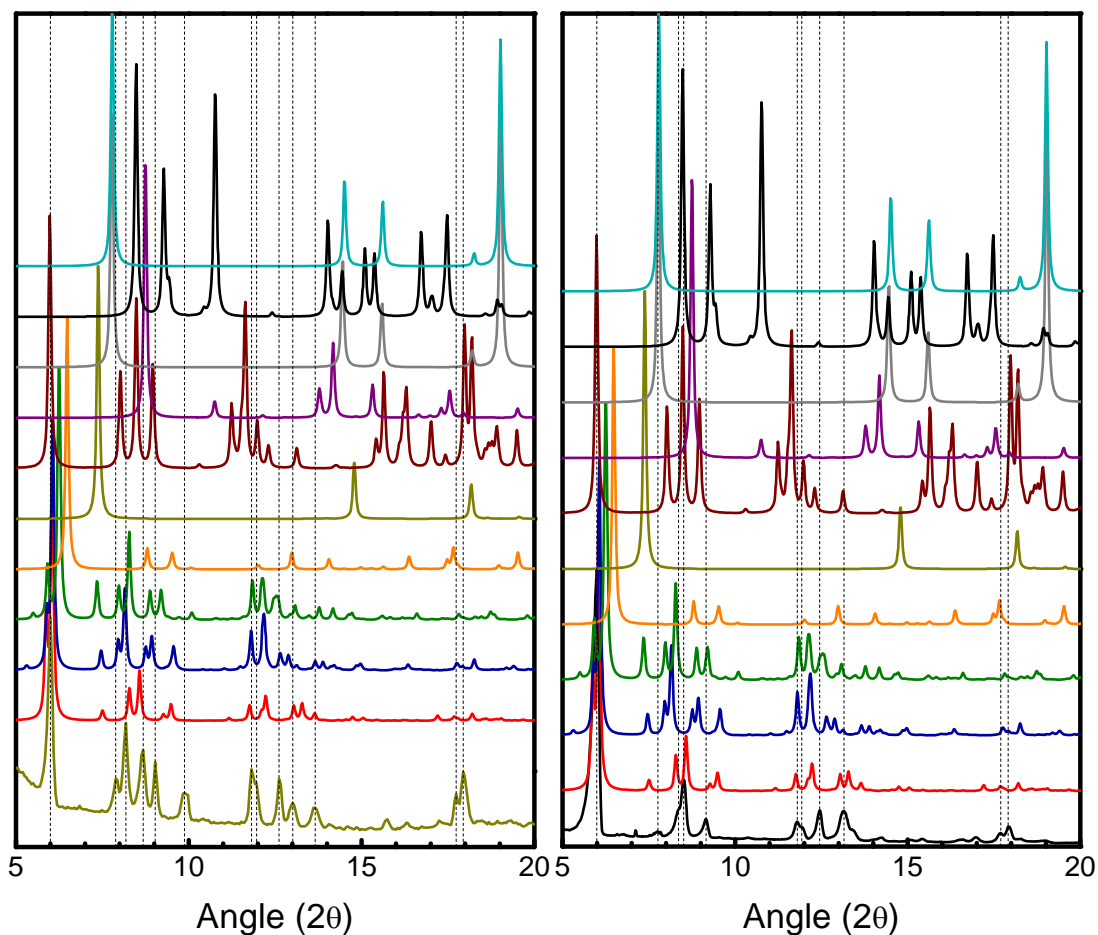
Figure 4.5. Comparison of simulated powder X-ray diffractograms of IRMOF-8-HT activated under reduced pressure (~20 mTorr) and all other known Zn/ndc-based coordination polymers. Dotted lines correspond to highest peaks and shoulders of IRMOF-8-HT diffractogram and serve to simplify visual comparison with other diffractograms. Diffractograms from top to bottom are $Zn(ndc) \cdot H_2O$,[84] $Zn_3(ndc)_3(CH_3OH)_2 \cdot 2DMF \cdot H_2O$,[85] CPO-1,[86] MOF-105,[87] MOF-37,[88] CPO-6,[89] MOF-69b,[90] UTSA-38,[91] SUMOF-3,[92] $\{[Zn_4O(ndc)_3(CH_3OH)(H_2O)]\}_n$,[93] and either IRMOF-8-HT as-synthesized (left figure) or IRMOF-8-HT after activation under reduced pressure (right figure), from this work.
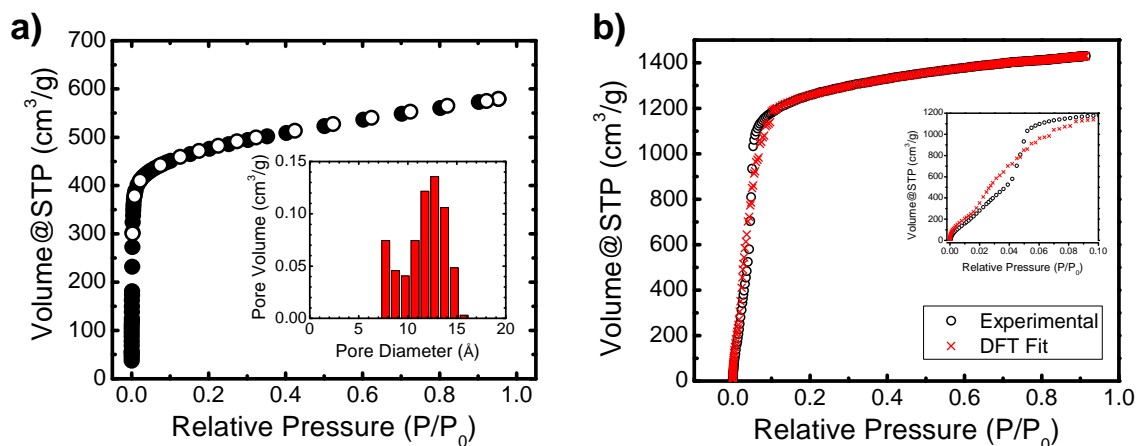
Figure 4.6. a) Ar sorption isotherm of IRMOF-8-HT activated under reduced pressure (~20 mTorr) obtained at 87 K (●, adsorption; ○, desorption). Inset: pore size distribution determined from NLDFT fit. b) NLDFT fit of IRMOF-8-HT Ar sorption data determined in NovaWin 9.0.[94] A fit error of 0.114 % was achieved using a model optimized for spherical and cylindrical pores in zeolites and silica. The adsorption branch of the isotherm was used for fitting. Inset: pressure range between 0-0.10 P/P_0 showing inexactness of fit in the P/P_0 = 0.02-0.08 pressure region. ○, experimental data. ×, NLDFT fit.
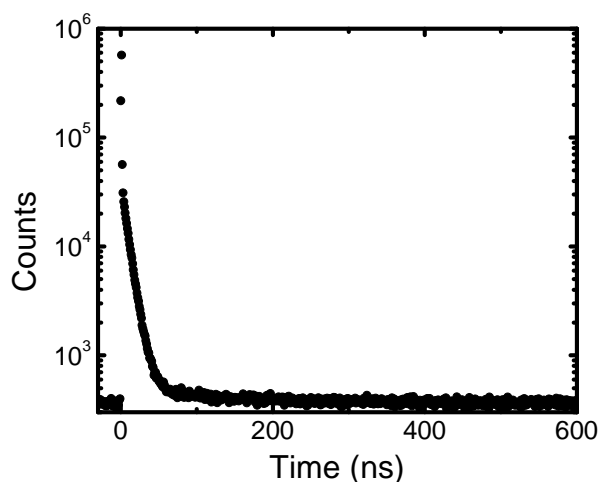
Figure 4.7. PALS spectrum of IRMOF-8-HT. The calculated lifetimes are 8.31 ± 0.12 ns, 16.48 ± 1.33 ns, and 90 ns, with intensities of 19.32 ± 0.53%, 2.88 ± 0.48%, and 2.47 ± 0.04%, respectively.
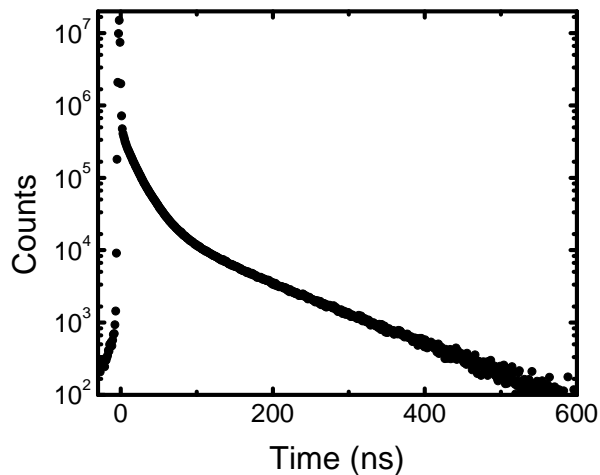
Figure 4.8. PALS spectrum of IRMOF-8-RT activated via flowing supercritical CO_2. The calculated lifetimes are 18.45 ± 0.26 ns and 90 ns, with intensities of $22.52 \pm 0.23\%$ and $2.69 \pm 0.14\%$, respectively.
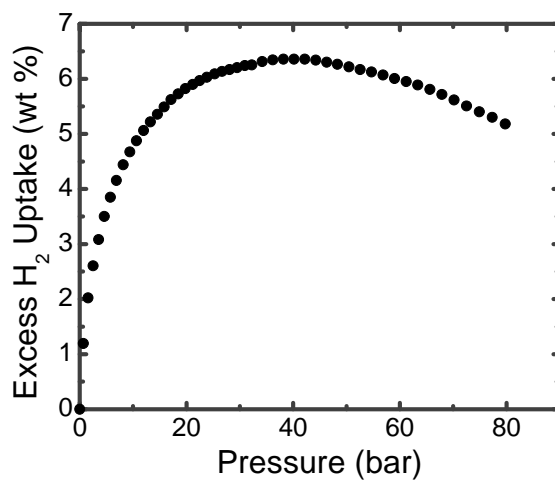
Figure 4.9. High pressure excess H_2 adsorption isotherm at 77 K of IRMOF-8-RT activated via flowing supercritical CO_2.
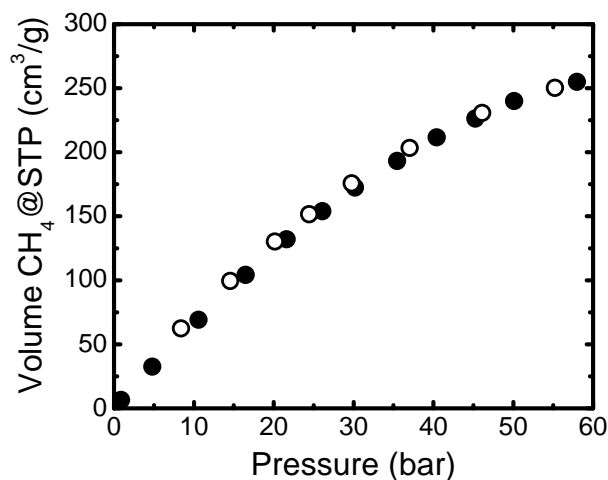
Figure 4.10. High pressure excess CH_4 sorption isotherm of IRMOF-8-RT at 298 K activated via flowing supercritical CO_2 (●, adsorption; ○, desorption).
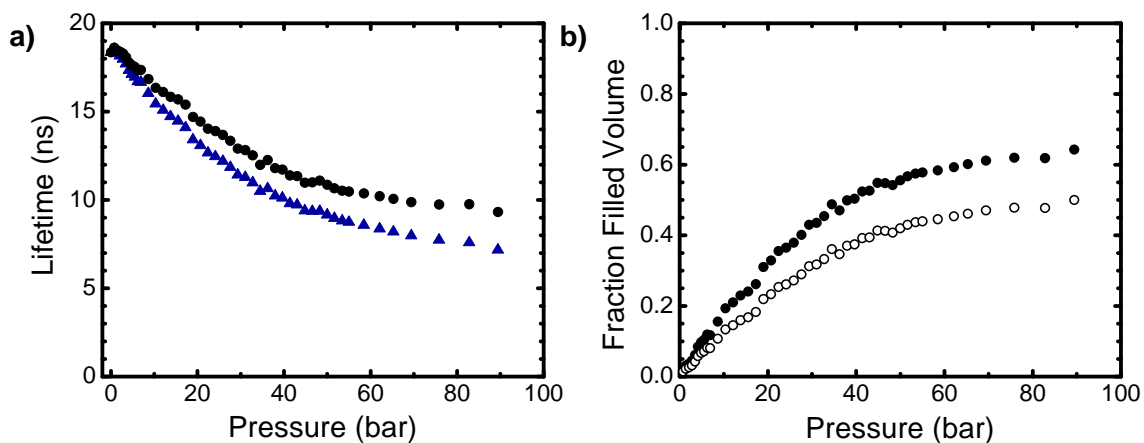
Figure 4.11. PALS analysis of IRMOF-8-RT as a function of CH_4 pressure at room temperature. a) *o*-Ps lifetime corrected (●) and uncorrected (▲) for *o*-Ps pickoff annihilation with free, unadsorbed methane gas in the IRMOF-8-RT pores. b) Fraction of pore volume filled by *adsorbed* methane estimated using models of 2D Ps confinement (●) and 3D Ps confinement (○) as discussed in the main text.

4.6   Tables

Table 1. Deliverable excess H_2 uptake at 77 K of select MCPs[a]

MCP	H_2@1 bar (wt %)	H_2 max (wt %)	Deliverable H_2 (wt%)	% Deliverable[b]	Ref.
IRMOF-8-RT	1.23	6.36	5.13	81	33, this work
IRMOF-20	1.35	6.67	5.32	80	17
SNU-70'	1.24	7.38	6.14	83	9
MOF-177	1.25	7.3	6.05	83	17,20
NOTT-101	2.52	6.06	3.54	58	69
PCN-68	1.87	7.32	5.45	74	7
PCN-66	1.79	6.65	4.86	73	7
PCN-61	2.25	6.24	3.99	64	7
IRMOF-11	1.62	3.52	1.90	54	17,20

Table 4. 1. Deliverable excess H_2 uptake at 77 K of select MCPs[a]

[a] Deliverable excess H_2 sorption calculated as the difference between the maximum excess H_2 uptake at 77 K and the excess uptake at 1 bar, the pressure at which most data were available.

[b] Fraction of maximum excess H_2 uptake (f_{deliv}) that is adsorbed above 1 bar.

4.7   References

(1)   Suh, M. P.; Park, H. J.; Prasad, T. K.; Lim, D.-W. *Chem. Rev.* **2012**, *112*, 782.
(2)   Makal, T. A.; Li, J.-R.; Lu, W.; Zhou, H.-C. *Chem. Soc. Rev.* **2012**, *41*, 7761.
(3)   Sumida, K.; Rogow, D. L.; Mason, J. A.; McDonald, T. M.; Bloch, E. D.; Herm, Z. R.; Bae, T.-H.; Long, J. R. *Chem. Rev.* **2012**, *112*, 724.
(4)   Hoskins, B. F.; Robson, R. *J. Am. Chem. Soc.* **1990**, *112*, 1546.
(5)   Abrahams, B. F.; Hoskins, B. F.; Michail, D. M.; Robson, R. *Nature* **1994**, *369*, 727.
(6)   Schnobrich, J. K.; Koh, K.; Sura, K. N.; Matzger, A. J. *Langmuir* **2010**, *26*, 5808.
(7)   Yuan, D.; Zhao, D.; Sun, D.; Zhou, H.-C. *Angew. Chem., Int. Ed.* **2010**, *49*, 5357.
(8)   Batten, S. R.; Robson, R. *Angew. Chem., Int. Ed.* **1998**, *37*, 1460.
(9)   Prasad, T. K.; Suh, M. P. *Chem.–Eur. J.* **2012**, *18*, 8673.
(10)   Robson, R. *Dalton Trans.* **2008**, 5113.

(11)   Deshpande, R. K.; Minnaar, J. L.; Telfer, S. G. *Angew. Chem. Int. Ed.* **2010**, *49*, 4598.

(12)   Yamada, T.; Kitagawa, H. *J. Am. Chem. Soc.* **2009**, *131*, 6312.

(13)   Tanabe, K. K.; Allen, C. A.; Cohen, S. M. *Angew. Chem. Int. Ed.* **2010**, *49*, 9730.

(14)   Ma, S.; Wang, X.-S.; Collier, C. D.; Manis, E. S.; Zhou, H.-C. *Inorg. Chem.* **2007**, *46*, 8499.

(15)   Eddaoudi, M.; Kim, J.; Rosi, N.; Vodak, D.; Wachter, J.; O'Keeffe, M.; Yaghi, O. M. *Science* **2002**, *295*, 469.

(16)   Li, H.; Eddaoudi, M.; O'Keeffe, M.; Yaghi, O. M. *Nature* **1999**, *402*, 276.

(17)   Wong-Foy, A. G.; Matzger, A. J.; Yaghi, O. M. *J. Am. Chem. Soc.* **2006**, *128*, 3494.

(18)   Kim, J.; Yang, S. T.; Choi, S. B.; Sim, J.; Ahn, W. S. *J. Mater. Chem.* **2011**, *21*, 3070.

(19)   Bae, Y.-S.; Dubbeldam, D.; Nelson, A.; Walton, K. S.; Hupp, J. T.; Snurr, R. Q. *Chem. Mater.* **2009**, *21*, 4768.

(20)   Rowsell, J. L. C.; Millward, A. R.; Park, K. S.; Yaghi, O. M. *J. Am. Chem. Soc.* **2004**, *126*, 5666.

(21)   Rowsell, J. L. C. Hydrogen Storage in Metal-Organic Frameworks: An Investigation of Structure-Property Relationships. Ph.D. Dissertation, University of Michigan, Ann Arbor, **2005**.

(22)   Mueller, U.; Schubert, M.; Teich, F.; Puetter, H.; Schierle-Arndt, K.; Pastré, J. *J. Mater. Chem.* **2006**, *16*, 626.

(23)   Li, Y.; Yang, R. T. *J. Am. Chem. Soc.* **2006**, *128*, 726.

(24)   Dailly, A.; Vajo, J. J.; Ahn, C. C. *J. Phys. Chem. B* **2006**, *110*, 1099.

(25)   Panella, B.; Hönes, K.; Müller, U.; Trukhan, N.; Schubert, M.; Pütter, H.; Hirscher, M. *Angew. Chem. Int. Ed.* **2008**, *47*, 2138.

(26)   Miller, M. A.; Wang, C.-Y.; Merrill, G. N. *J. Phys. Chem. C* **2009**, *113*, 3222.

(27)   Tsao, C.-S.; Yu, M.-S.; Wang, C.-Y.; Liao, P.-Y.; Chen, H.-L.; Jeng, U.-S.; Tzeng, Y.-R.; Chung, T.-Y.; Wu, H.-C. *J. Am. Chem. Soc.* **2009**, *131*, 1404.

(28)   Wang, C.-Y.; Tsao, C.-S.; Yu, M.-S.; Liao, P.-Y.; Chung, T.-Y.; Wu, H.-C.; Miller, M. A.; Tzeng, Y.-R. *J. Alloys Compd.* **2010**, *492*, 88.

(29)   Orefuwa, S. A.; Yang, H.; Goudy, A. J. *Microporous Mesoporous Mater.* **2012**, *153*, 88.

(30)   Ardelean, O.; Blanita, G.; Borodi, G.; Mihet, M.; Coros, M.; Lupu, D. *Int. J. Hydrog. Energy* **2012**, *37*, 7378.

(31)   Yang, S. J.; Im, J. H.; Nishihara, H.; Jung, H.; Lee, K.; Kyotani, T.; Park, C. R. *J. Phys. Chem. C* **2012**, *116*, 10529.

(32)   Yang, S. J.; Kim, T.; Im, J. H.; Kim, Y. S.; Lee, K.; Jung, H.; Park, C. R. *Chem. Mater.* **2012**, *24*, 464.

(33)   Feldblyum, J. I.; Wong-Foy, A. G.; Matzger, A. J. *Chem. Commun.* **2012**, *48*, 9828.

(34)   Feldblyum, J. I.; Liu, M.; Gidley, D. W.; Matzger, A. J. *J. Am. Chem. Soc.* **2011**, *133*, 18257.

(35)   Liu, M.; Wong-Foy, A. G.; Vallery, R. S.; Frieze, W. E.; Schnobrich, J. K.; Gidley, D. W.; Matzger, A. J. *Adv. Mater.* **2010**, *22*, 1598.

(36)   Jean, Y. C. *Microchem. J.* **1990**, *42*, 72.

(37)   Gidley, D. W.; Peng, H. G.; Vallery, R. S. *Ann. Rev. Mater. Res.* **2006**, *36*, 49.

(38)   Nguyen, L. T. L.; Nguyen, C. V.; Dang, G. H.; Le, K. K. A.; Phan, N. T. S. *J. Mol. Catal. A-Chem.* **2011**, *349*, 28.

(39)   Düren, T.; Millange, F.; Férey, G.; Walton, K. S.; Snurr, R. Q. *J. Phys. Chem. C* **2007**, *111*, 15350.

(40)   Siberio-Pérez, D. Y.; Wong-Foy, A. G.; Yaghi, O. M.; Matzger, A. J. *Chem. Mater.* **2007**, *19*, 3681.

(41)   Prosenjak, C.; Banu, A.-M.; Gellan, A. D.; Düren, T. *Dalton Trans.* **2012**, *41*, 3974.

(42)   Gelb, L. D.; Gubbins, K. E. *Langmuir* **1999**, *15*, 305.

(43)   Bhattacharya, S.; Gubbins, K. E. *Langmuir* **2006**, *22*, 7726.

(44)   Liu, B.; Wong-Foy, A. G.; Matzger, A. J. *Chem. Commun.* **2013**, *49*, 1419.

(45)   Dutta, D.; Feldblyum, J. I.; Gidley, D. W.; Imirzian, J.; Liu, M.; Matzger, A. J.; Vallery, R. S.; Wong-Foy, A. G. *Phys. Rev. Lett.* **2013**, *110*, 197403.

(46)   Dull, T. L.; Frieze, W. E.; Gidley, D. W.; Sun, J. N.; Yee, A. F. *J. Phys. Chem. B* **2001**, *105*, 4657.

(47)   Jasińska, B.; Dawidowicz, A. L.; Goworek, T.; Wawryszczuk, J. *Opt. Appl.* **2003**, *33*, 7.

(48)   Tao, S. J. *J. Chem. Phys.* **1972**, *56*, 5499.

(49)   Eldrup, M.; Lightbody, D.; Sherwood, J. N. *Chem. Phys.* **1981**, *63*, 51.

(50)   The channel-like pore assumption has been used previously and in this work to interpret PALS data for non-interpenetrated MCPs. Strictly speaking, the PALS lifetime is related to the mean free path of o-Ps in a pore of arbitrary shape, although quantum mechanical effects can complicate data interpretation in highly ordered porous materials. While we have found that the pore size derived in this manner tends to match that expected from crystallographic pore dimension, a rigorous physical link between PALS-derived pore size and crystallographic pore size has not yet been established. We have begun to address these points in a recently published manuscript (Ref. 45), and intend to further elucidate them in additional forthcoming work.

(51)   The volume fraction of small pores in a material with large and small pores (such as IRMOF-8-HT) can be estimated by assuming that the probability of o-Ps formation in a pore increases linearly with the surface area of the pore. Since intensity is a measure of relative population (*number* fraction), it must be weighed by the pore volume to determine the *volume* fraction of a given pore. With these considerations in mind, we can estimate that the small pores in IRMOF-8-HT comprise roughly 80% of the total pore volume. This estimate neglects considerations such as the spatial distribution of small and large pores, the diffusion length of o-Ps in these materials, and differences in the likelihood of o-Ps formation in small and large pores that may be influenced by chemistry as well as by pore volume. Thus, while our data suggest that the material is predominantly interpenetrated, the exact degree of interpenetration cannot be precisely determined given that all factors contributing to the intensity cannot be quantified.

(52)   Caskey, S. R.; Matzger, A. J. Selected Applications of Metal-Organic Frameworks in Sustainable Energy Technologies. *Materials Matters*, **2009**, 4.4, 111. Sigma-Aldrich: St. Louis, MO.

(53)   Furukawa, H.; Miller, M. A.; Yaghi, O. M. *J. Mater. Chem.* **2007**, *17*, 3197.

(54)   Ma, S.; Eckert, J.; Forster, P. M.; Yoon, J. W.; Hwang, Y. K.; Chang, J.-S.; Collier, C. D.; Parise, J. B.; Zhou, H.-C. *J. Am. Chem. Soc.* **2008**, *130*, 15896.

(55)   Bae, Y.-S.; Snurr, R. Q. *Microporous Mesoporous Mater.* **2010**, *132*, 300.

(56)   Han, S. S.; Choi, S.-H.; Goddard, W. A. *J. Phys. Chem. C* **2011**, *115*, 3507.

(57)   Kuchta, B.; Firlej, L.; Pfeifer, P.; Wexler, C. *Carbon* **2010**, *48*, 223.

(58)   Bonilla, M. R.; Bae, J.-S.; Nguyen, T. X.; Bhatia, S. K. *J. Phys. Chem. C* **2010**, *114*, 16562.

(59)   Cao, D.; Feng, P.; Wu, J. *Nano Lett.* **2004**, *4*, 1489.

(60)   Gigras, A.; Bhatia, S. K.; Kumar, A. V. A.; Myers, A. L. *Carbon* **2007**, *45*, 1043.

(61)   Firlej, L.; Roszak, S.; Kuchta, B.; Pfeifer, P.; Wexler, C. *J. Chem. Phys.* **2009**, *131*, 164702.

(62)   Henwood, D.; Carey, J. D. *Phys. Rev. B* **2007**, *75*, 245413.

(63)   Getman, R. B.; Miller, J. H.; Wang, K.; Snurr, R. Q. *J. Phys. Chem. C* **2011**, *115*, 2066.

(64)   Ghoufi, A.; Deschamps, J.; Maurin, G. *J. Phys. Chem. C* **2012**, *116*, 10504.

(65)   Purewal, J.; Liu, D.; Sudik, A.; Veenstra, M.; Yang, J.; Maurer, S.; Müller, U.; Siegel, D. J. *J. Phys. Chem. C* **2012**, *116*, 20199.

(66)   Kumar, K. V.; Salih, A.; Lu, L.; Müller, E. A.; Rodríguez-Reinoso, F. *Adsorption Science & Technology* **2011**, *29*, 799.

(67)   Bastos-Neto, M.; Patzschke, C.; Lange, M.; Möllmer, J.; Möller, A.; Fichtner, S.; Schrage, C.; Lässig, D.; Lincke, J.; Staudt, R.; Krautscheid, H.; Gläser, R. *Energy Environ. Sci.* **2012**, *5*, 8294.

(68)   US Department of Energy: DOE Targets for Onboard Hydrogen Storage Systems for Light-Duty Vehicles, rev. 4.0. http://www1.eere.energy.gov/hydrogenandfuelcells/storage/pdfs/targets_onboard_hydro_storage_explanation.pdf. (Accessed Nov. 24, 2012.)

(69)   Lin, X.; Telepeni, I.; Blake, A. J.; Dailly, A.; Brown, C. M.; Simmons, J. M.; Zoppi, M.; Walker, G. S.; Thomas, K. M.; Mays, T. J.; Hubberstey, P.; Champness, N. R.; Schröder, M. *J. Am. Chem. Soc.* **2009**, *131*, 2159.

(70)   Matranga, K. R.; Myers, A. L.; Glandt, E. D. *Chem. Eng. Sci.* **1992**, *47*, 1569.

(71)   Sircar, S.; Golden, T. C.; Rao, M. B. *Carbon* **1996**, *34*, 1.

(72)   Perrin, A.; Celzard, A.; Albiniak, A.; Kaczmarczyk, J.; Marêché, J. F.; Furdin, G. *Carbon* **2004**, *42*, 2855.

(73)   Celzard, A.; Albiniak, A.; Jasienko-Halat, M.; Marêché, J. F.; Furdin, G. *Carbon* **2005**, *43*, 1990.

(74)   Mendoza-Cortés, J. L.; Han, S. S.; Furukawa, H.; Yaghi, O. M.; Goddard, W. A. *The Journal of Physical Chemistry A* **2010**, *114*, 10824.

(75)   Lyubchyk, A.; Esteves, I. A. A. C.; Cruz, F. J. A. L.; Mota, J. P. B. *J. Phys. Chem. C* **2011**, *115*, 20628.

(76)   Mendoza-Cortes, J. L.; Pascal, T. A.; Goddard, W. A. *The Journal of Physical Chemistry A* **2011**, *115*, 13852.

(77)   Mahdizadeh, S.; Tayyari, S. *Journal of Molecular Modeling* **2012**, *18*, 2699.

(78)   Bhatia, S. K.; Myers, A. L. *Langmuir* **2006**, *22*, 1688.

(79)   U.S. Department of Energy, Advanced Research Projects Agency - Energy (ARPA-E): Methane Opportunities for Vehicular Energy. https://arpa-e-foa.energy.gov/FileContent.aspx?FileID=13088dca-1cf6-4591-8cfc-ea81edfa786e. (Accessed Apr. 7, 2013.)

(80)   Cracknell, R. F.; Gordon, P.; Gubbins, K. E. *J. Phys. Chem.* **1993**, *97*, 494.

(81)   Wilmer, C. E.; Leaf, M.; Lee, C. Y.; Farha, O. K.; Hauser, B. G.; Hupp, J. T.; Snurr, R. Q. *Nat Chem* **2012**, *4*, 83.

(82)   Rouquerol, J.; Llewellyn, P.; Rouquerol, F. In *Characterization of Porous Solids VII - Proceedings of the 7th International Symposium on the Characterization of Porous Solids*; Llewellyn, P. L., Rodriquez Reinoso, F., Rouqerol, J., Seaton, N., Eds. 2007; Vol. 160, p 49.

(83)   Walton, K. S.; Snurr, R. Q. *J. Am. Chem. Soc.* **2007**, *129*, 8552.

(84)   Min, D.; Yoon, S. S.; Lee, C.; Lee, C. Y.; Suh, M.; Hwang, Y.-J.; Han, W. S.; Lee, S. W. *Bull. Korean Chem. Soc.* **2001**, *22*, 531.

(85)   Dincă, M.; Long, J. R. *J. Am. Chem. Soc.* **2005**, *127*, 9376.

(86)   Kongshaug, K. O.; Fjellvåg, H. *Solid State Sci.* **2002**, *4*, 443.

(87)   Eddaoudi, M.; Kim, J.; Vodak, D.; Sudik, A.; Wachter, J.; O'Keeffe, M.; Yaghi, O. M. *Proc. Natl. Acad. Sci. U. S. A.* **2002**, *99*, 4900.

(88)   Kim, J.; Chen, B.; Reineke, T. M.; Li, H.; Eddaoudi, M.; Moler, D. B.; O'Keeffe, M.; Yaghi, O. M. *J. Am. Chem. Soc.* **2001**, *123*, 8239.

(89)   Kongshaug, K. O.; Fjellvåg, H. *J. Solid State Chem.* **2004**, *177*, 1852.

(90)   Rosi, N. L.; Eddaoudi, M.; Kim, J.; O'Keeffe, M.; Yaghi, O. M. *Angew. Chem., Int. Ed.* **2002**, *41*, 284.

(91)   Das, M. C.; Xu, H.; Wang, Z.; Srinivas, G.; Zhou, W.; Yue, Y.-F.; Nesterov, V. N.; Qian, G.; Chen, B. *Chem. Commun.* **2011**, *47*, 11715.

(92)   Yao, Q.; Su, J.; Cheung, O.; Liu, Q.; Hedin, N.; Zou, X. *J. Mater. Chem.* **2012**, *22*, 10345.

(93)   Perry IV, J. J.; Feng, P. L.; Meek, S. T.; Leong, K.; Doty, F. P.; Allendorf, M. D. *J. Mater. Chem.* **2012**, *22*, 10235.

(94)   NovaWin 9.0; Quantachrome Instruments: Boynton Beach, FL. 2007.

Chapter 5

Conclusions and Future Perspectives

The studies herein represent only a glimpse of the possible challenges encountered during the discovery and characterization of new microporous coordination polymers (MCPs). Interpenetration and collapse on guest removal are common, and while localized defects such as the surface collapse in Zn-HKUST-1 has not yet been reported explicitly in other materials, all of these phenomena represent obstacles that can remain undetected and limit the utility of MCPs as high-performance sorbents. While PALS has proven an indispensable tool for elucidating the structural characteristics of MCPs, future work must also develop methods to circumvent structural defects limiting porosity in these materials.

Interpenetration may be one of the most common obstacles to achieving large pores in MCPs. A number of approaches have been demonstrated to achieve non-interpenetrated materials, including those outlined earlier in this thesis. Changing solvent,[1-3] temperature,[4,5] or reactant concentration[5] have in some cases proven viable strategies to eliminate interpenetration. However, these approaches often require laborious screening of reaction conditions before interpenetration is eliminated. The use of bulky substituents to frustrate interpenetration has shown some success,[6-8] but this strategy by its nature still reduces porosity in the resulting MCP. Furthermore, bulky substituents can sometimes change the net topology of the resulting framework entirely.[9] The use of bulky photolabile[10] or thermolabile[11-13] substituents improves on this approach, allowing the revelation of near-ideal porosity after a non-interpenetrated material is formed. Wöll and coworkers showed that non-interpenetrated MOF-508a could be synthesized by step-by-step growth off of a surface, the surface serving to eliminate translational symmetry in the MCP, thereby frustrating interpenetration.[14]

While a clever approach, this has not yet been demonstrated to apply to other materials. A curious result was obtained by Ahn and coworkers, who discovered that sonochemical synthesis of $Cu_3(tatb)_2$ (tatb = 4,4′,4″-s-triazine-2,4,6-tryl-tribenzoate) or $Zn_4O(bpdc)$ (4,4′-biphenyl dicarboxylate) reduced interpenetration in these materials.[15] Very recently, post-synthetic ligand exchange was used to expand the porosity of a pre-synthesized, smaller-pore MCP, circumventing interpenetration that occurred in the direct synthesis of the target material. An interesting result reported by Zhou and coworkers showed that the inclusion of a small amount of oxalic acid in the MCP synthesis solution eliminated interpenetration in $Cu_3(tatb)_2$;[16] this strategy has not been developed further. The "infinite SBU" approach was espoused by Yaghi in the early 2000s;[17] however, the closely-packed metal atoms in these materials lead to MCPs of relatively high density. Finally, MCPs of certain net topology cannot interpenetrate, such as the **rht** net, which has been utilized in the MCP with the highest surface area to date.[18]

Introducing small amounts of linkers of smaller or larger size as "impurities" to frustrate interpenetration (as in the aforementioned work of Zhou and coworkers[16]) may be a promising approach to achieve non-interpenetrated MCPs of the desired structure. Preliminary results in our laboratory show the success of this strategy for at least one material. An added advantage to this approach is that the host framework may tolerate typically incompatible linker functionality in the impurity linker. Our group previously showed that carboxylic acid functionality could be imparted to MOF-5 in this manner.[19] It remains to be seen how much non-structural ligand can be tolerated in an MCP before its long-range order is modified or eliminated; this avenue of research is certainly underexplored and deserves greater scrutiny.

Collapse on guest removal is an issue that has been directly addressed by the research groups of Lin and Hupp. Lin and coworkers used freeze-drying to improve the activation of a copper-based MCP.[20] Hupp used supercritical CO_2 activation to enhance porosity in $Zn_4O(tpdc)_3$ (tpdc = p-terphenyl-4,4″-dicarboxylate) and other materials;[21] this approach quickly gained traction, and inspired our own improved flowing supercritical CO_2 activation method.[22] While further methods may be developed in the future, it is unlikely that MCPs unstable toward supercritical CO_2 activation will be stable after other means of guest removal; it is probable that such MCPs are unstable in the

absence of guests in their pores. Structural collapse has been avoided by the inclusion of molecular "struts" to bolster the porous structure.[23] However, this often entails the deliberate introduction of interpenetration,[16] which is counterproductive to achieving high porosity in the first place. The removal of generally insoluble, non-volatile guests such as metal oxides from MCP pores can also prove quite challenging.[24] Harsh conditions to remove these guests can dissolve the MCP as well. In such cases, synthesis conditions must be developed to bypass the formation of these species in the first place.

The characterization of disorder in MCPs requires techniques beyond those necessary for standard assessment of crystallinity and porosity. Furthermore, the challenges faced in describing disorder are often unique to the particular material in question. This dissertation has focused on the use of PALS to elucidate the nature of such disorder. Due to the nature of *ortho*-positronium (*o*-Ps) diffusion in an MCP, *o*-Ps localizes in non-interconnected ("buried") pores, allowing the detection of such defects. Depth-profiling also allows examination of a sample's pore characteristics at the surface with high (nm) depth resolution. The studies discussed in this thesis have shown the utility of PALS in detecting surface barriers, interpenetration, thermal degradation, and pore characteristics on gas adsorption. This work also led to conclusive evidence that *o*-Ps assumes a Bloch state in highly ordered and interconnected MCP pores (see Appendix A).

Looking ahead, PALS will serve as an invaluable tool to examine pore evolution during gas adsorption and chemical/thermal perturbation. We are currently examining water adsorption and water-induced degradation of MCPs; preliminary results suggest that water *condensation* is necessary to irreparably damage Zn_4O-based MCPs. Below a threshold value (dependent on pore size) of relative humidity, materials such as MOF-5 appear to be stable. There remains much opportunity to examine the influence of pore structure on this phenomenon. Extending this work to materials having multiple pore sizes such as UMCM-2[25] and UMCM-3[26] could help to elucidate the factors governing pore collapse on exposure to water in these materials. UMCM-1,[27] with long, open, 3.2 nm diameter channels flanked by smaller, more constricted pores, might show distinct degradation characteristics in the presence of H_2O vapor. Finally, chemical

functionalization may reveal enhanced or diminished propensity for water condensation in MCP pores; PALS presents an ideal platform with which to study these subjects.

A significant challenge in PALS is the study of materials having unpaired electrons. Unpaired electrons (such as those in Cu^{2+}, commonly used to form MCPs) can rapidly accelerate the annihilation of o-Ps in a process called "conversion," whereby the electron in o-Ps exchanges with the unpaired electron in the surrounding environment, converting o-Ps to p-Ps, which annihilates ~1000 times more rapidly.[28] Reduction of observable o-Ps formation by the presence of bromine has also been seen to occur;[29] the cause for this effect is not currently understood, but may be due to chemical quenching, as has been observed for o-Ps annihilation in bromine-impregnated silica gel.[30] While the presence of coordinatively unsaturated metal sites (UMCs) in archetypal MCPs such as HKUST-1[31] drastically reduces the measured intensity of o-Ps annihilation from the pores, it may be possible to explore chemical passivation techniques which would enable o-Ps annihilation intensity adequate to study the pore characteristics of such materials. It is conceivable that physically blocking UMCs or heavy atoms (such as bromine) with a strongly adsorbed gas may also enable PALS studies in materials exhibiting low annihilation intensities under vacuum. Not only would this enable the study of the structural pore characteristics of such materials, but it may also provide a route to directly examine the interaction of adsorbed species with atoms or chemical groups known to quench o-Ps or suppress its formation.

Finally, the work discussed herein may pave the way for examining the fundamental physics of o-Ps in ordered, porous materials. We have already discovered that o-Ps assumes a Bloch state in MOF-5 and IRMOF-8.[32] Future work can proceed in a number of directions. The energy of emitted o-Ps from MCPs is currently being studied by velocity spectroscopy;[33] it appears that o-Ps can thermalize in an MCP lattice and subsequently be emitted with an energy gain directly related to the size of the MCP pores. This may be an approach to obtaining monoenergetic o-Ps having energies higher than thermal energy. o-Ps trapping phenomena have been observed in functionalized IRMOFs[34] at cryogenic temperature. It is possible that pendant groups on linkers may orient toward the center of the pore, forming a smaller space that can disrupt the o-Ps Bloch state and serve as an energy well from which o-Ps cannot easily escape. More

work needs to be carried out to explain such phenomena and explore the generality to other MCPs of different structure and functionality.

(1)   Ma, L.; Lin, W. *J. Am. Chem. Soc.* **2008**, *130*, 13834.

(2)   Bureekaew, S.; Sato, H.; Matsuda, R.; Kubota, Y.; Hirose, R.; Kim, J.; Kato, K.; Takata, M.; Kitagawa, S. *Angew. Chem., Int. Ed.* **2010**, *49*, 7660.

(3)   Guo, M.; Sun, Z.-M. *J. Mater. Chem.* **2012**, *22*, 15939.

(4)   Feldblyum, J. I.; Wong-Foy, A. G.; Matzger, A. J. *Chem. Commun.* **2012**, *48*, 9828.

(5)   Zhang, J.; Wojtas, L.; Larsen, R. W.; Eddaoudi, M.; Zaworotko, M. J. *J. Am. Chem. Soc.* **2009**, *131*, 17040.

(6)   Go, Y. B.; Wang, X.; Jacobson, A. J. *Inorg. Chem.* **2007**, *46*, 6594.

(7)   Farha, O. K.; Malliakas, C. D.; Kanatzidis, M. G.; Hupp, J. T. *J. Am. Chem. Soc.* **2009**, *132*, 950.

(8)   He, H.; Yuan, D.; Ma, H.; Sun, D.; Zhang, G.; Zhou, H.-C. *Inorg. Chem.* **2010**, *49*, 7605.

(9)   Ma, S.; Wang, X.-S.; Collier, C. D.; Manis, E. S.; Zhou, H.-C. *Inorg. Chem.* **2007**, *46*, 8499.

(10)   Deshpande, R. K.; Waterhouse, G. I. N.; Jameson, G. B.; Telfer, S. G. *Chem. Commun.* **2012**, *48*, 1574.

(11)   Yamada, T.; Kitagawa, H. *J. Am. Chem. Soc.* **2009**, *131*, 6312.

(12)   Deshpande, R. K.; Minnaar, J. L.; Telfer, S. G. *Angew. Chem. Int. Ed.* **2010**, *49*, 4598.

(13)   Lun, D. J.; Waterhouse, G. I. N.; Telfer, S. G. *J. Am. Chem. Soc.* **2011**, *133*, 5806.

(14)   Shekhah, O.; Wang, H.; Paradinas, M.; Ocal, C.; Schupbach, B.; Terfort, A.; Zacher, D.; Fischer, R. A.; Wöll, C. *Nat. Mater.* **2009**, *8*, 481.

(15)   Kim, J.; Yang, S. T.; Choi, S. B.; Sim, J.; Ahn, W. S. *J. Mater. Chem.* **2011**, *21*, 3070.

(16)   Ma, S.; Sun, D.; Ambrogio, M.; Fillinger, J. A.; Parkin, S.; Zhou, H.-C. *J. Am. Chem. Soc.* **2007**, *129*, 1858.

(17)   Rosi, N. L.; Eddaoudi, M.; Kim, J.; O'Keeffe, M.; Yaghi, O. M. *Angew. Chem., Int. Ed.* **2002**, *41*, 284.

(18)   Farha, O. K.; Eryazici, I.; Jeong, N. C.; Hauser, B. G.; Wilmer, C. E.; Sarjeant, A. A.; Snurr, R. Q.; Nguyen, S. T.; Yazaydın, A. Ö.; Hupp, J. T. *J. Am. Chem. Soc.* **2012**, *134*, 15016.

(19)   Park, T.-H.; Hickman, A. J.; Koh, K.; Martin, S.; Wong-Foy, A. G.; Sanford, M. S.; Matzger, A. J. *J. Am. Chem. Soc.* **2011**, *133*, 20138.

(20)   Ma, L. Q.; Jin, A.; Xie, Z. G.; Lin, W. B. *Angew. Chem. Int. Ed.* **2009**, *48*, 9905.

(21)   Nelson, A. P.; Farha, O. K.; Mulfort, K. L.; Hupp, J. T. *J. Am. Chem. Soc.* **2009**, *131*, 458.

(22)   Liu, B.; Wong-Foy, A. G.; Matzger, A. J. *Chem. Commun.* **2013**, *49*, 1419.

(23)   Bezzu, C. G.; Helliwell, M.; Warren, J. E.; Allan, D. R.; McKeown, N. B. *Science* **2010**, *327*, 1627.

(24)   Hafizovic, J.; Bjørgen, M.; Olsbye, U.; Dietzel, P. D. C.; Bordiga, S.; Prestipino, C.; Lamberti, C.; Lillerud, K. P. *J. Am. Chem. Soc.* **2007**, *129*, 3612.

(25)   Koh, K.; Wong-Foy, A. G.; Matzger, A. J. *J. Am. Chem. Soc.* **2009**, *131*, 4184.

(26)   Koh, K.; Wong-Foy, A. G.; Matzger, A. J. *J. Am. Chem. Soc.* **2010**, *132*, 15005.

(27)   Koh, K.; Wong-Foy, A. G.; Matzger, A. J. *Angew. Chem. Int. Ed.* **2008**, *47*, 677.

(28)   Hyodo, T.; Nakayama, T.; Saito, H.; Saito, F.; Wada, K. *physica status solidi (c)* **2009**, *6*, 2497.

(29)   Gidley, D. W. *Unpublished results*.

(30)   Chuang, S. Y.; Tao, S. J. *Appl. Phys.* **1974**, *3*, 199.

(31)   Chui, S. S.-Y.; Lo, S. M. F.; Charmant, J. P. H.; Orpen, A. G.; Williams, I. D. *Science* **1999**, *283*, 1148.

(32)   Dutta, D.; Feldblyum, J. I.; Gidley, D. W.; Imirzian, J.; Liu, M.; Matzger, A. J.; Vallery, R. S.; Wong-Foy, A. G. *Phys. Rev. Lett.* **2013**, *110*, 197403.

(33)   Mariazzi, S.; Bettotti, P.; Brusa, R. S. *Phys. Rev. Lett.* **2010**, *104*, 243401.

(34)   Eddaoudi, M.; Kim, J.; Rosi, N.; Vodak, D.; Wachter, J.; O'Keeffe, M.; Yaghi, O. M. *Science* **2002**, *295*, 469.

Appendix A

Evidence of Positronium Bloch States in Porous Crystals of Zn$_4$O-Coordination Polymers[†]

A.1   Introduction

Positronium (Ps) is the hydrogenlike bound state of an electron with its antiparticle, the positron. Its ground state consists of spin singlet (*p*-Ps) and triplet states (*o*-Ps) that annihilate into two and three photons, respectively, with mean lifetimes of 0.125 and 142 ns.[1] Ps readily forms by electron capture when positrons are stopped in matter. In gases the Ps is free, interacting with the gas molecules only during collisions. In condensed matter Ps does not form in metals due to electron screening. In amorphous insulators Ps forms, localizes, and decays in open volume regions and is a well-known probe to characterize such ''free'' volume.[2] In some crystalline materials and within certain temperature limits *p*-Ps is observed in a delocalized Bloch state[3-6] but this is relatively rare and strong many-body effects can distort Ps and complicate interpretation. Such a novel quantum state of a single atom in a crystalline solid has also been observed for the heavier exotic atom of muonium,[7] but only at very low temperatures (<10 mK). Recently a new class of crystalline materials called microporous coordination polymers, MCPs,[8,9] has been synthesized that has nanometer-sized open volume networks that promote copious Ps formation.[10] We will show that triplet Ps in an MCP can be in a completely delocalized state consistent with a Bloch state throughout the temperature range from 77 to 650 K, thus enabling the exploration of Ps Bloch state decay and dynamics or transport using simple lifetime techniques.

MCPs are formed from the self-assembled linking together of metals or metal-oxide clusters and organic ligands (''linkers'') of controllable nanometer lengths to form rigid, highly porous (open volumes up to 93%[11]) lattices with record-setting specific surface areas (>5000 m^2/g^{11-16}). Development of MCPs over the last decade has attracted intense interest from both academic and industrial researchers[17] because of the transformative impact of this sorbent class for applications such as gas storage[15,17], separation[18] and catalysis.[19] O-Ps shows great promise as a unique, *in situ* probe[10,20] of these new crystals. O-Ps lifetimes measured in MCPs are nominally consistent with the standard Tao-Eldrup model[21,22] and its extensions[23,24] in terms of deducing a mean free path in the porous network, but these models inherently treat Ps *localized* in at least two dimensions (e.g., confined radially in a very long cylindrical pore). By ignoring the regularity of the highly open lattice the mobility of the Ps Bloch state and the startlingly long diffusion lengths that result and affect how Ps probes the material are lost. To realize its promising potential it is crucial to understand the quantum state in which Ps exists in MCPs.

A.2   Experimental Section

We focus this study on two MCPs called IRMOF-1 and IRMOF-8 (IRMOF refers to "isoreticular metal-organic framework," a MOF having the same net topology; see Figure A.1). The IRMOF series[25] consists of cubic-structured materials comprised of octahedral Zn_4O clusters linked together by linear dicarboxylates of variable length and chemical functionality. IRMOF-1 and IRMOF-8 are characterized for specific surface area, 3100 and 4200 m^2/g, respectively, and crystallinity (sharp X-ray diffraction pattern matching patterns simulated from previously published crystallographic models). Both have individual grains that are transparent cubic single crystals with average side length of 300 μm. MCPs are analyzed by stopping positrons in them and measuring the lifetimes of o-Ps that annihilates both in and between the grains. The timing apparatus is similar to that reported in Ref. 10. We have two standard bulk PALS spectrometers and a variety of vacuum tight holders that permit vacuum and high pressure gas exposure, resistive heating, and liquid nitrogen sample cooling. A ^{22}Na positron source of ~10 μCi is

deposited on a tungsten foil and placed at the bottom of a well containing about 0.1 cm^3 of MCP crystals. The fraction of all positrons emitted from the source that annihilate as *o*-Ps is 35-40%.

A.3   Results and Discussion

The annihilation lifetime spectrum is generally well fitted with 3 lifetimes: a short lifetime less than 0.5 ns due to positron and *p*-Ps annihilation; a predominant *o*-Ps lifetime around 13.5 (IRMOF-1) or 18.5 ns (IRMOF-8) due to *o*-Ps annihilation within the crystal framework (72%–90% of the *o*-Ps); and a long lifetime (roughly 80 ns in evacuated MCP) comprising 10-28% of all *o*-Ps decays. These framework lifetimes correspond in extended Tao-Eldrup annihilation models[23] to *o*-Ps mean free paths for annihilation of 1.3 and 1.5 nm, respectively, close to the mean free paths (1.5 and 1.8 nm) calculated from $4V/S$ where V and S are specific free volume and surface area from adsorption data.[25] Based on the same annihilation models Liu et al.[10] suggested that the 80 ns lifetime component in evacuated IRMOF-1 was due to *o*-Ps trapping in widely spaced 6 nm diameter crystal defects. We will show that it is instead due to *o*-Ps diffusing out and escaping from the crystal grains and annihilating in the intergranular open volume. This escape is both very surprising and revealing for two reasons: (i) It is surprising that *o*-Ps in such open interparticle volume with void size comparable to the 300 μm particle size, has such a *short* lifetime of 80 ns and not a value[23] much closer to that of *o*-Ps in free-space vacuum, 142 ns; and (ii) grain escape would require an extraordinarily long *o*-Ps diffusion length ℓ within the MCP grain of ~10 μm. This implies a diffusion constant D of order 100 cm^2/s, two orders of magnitude larger than *o*-Ps or positron diffusion constants reported for condensed matter.[26-29] We will have to abandon the classical model of *o*-Ps diffusion in favor of a quantum mechanical treatment similar to that for treating electron conductivity and its temperature dependence in metals.

To show that the 80 ns component is due to *o*-Ps escaping from the IRMOF-1 grains, PALS spectra were acquired with the MCP exposed to helium and hydrogen gas pressures ranging from vacuum to 110 bar. Our focus is on the decay rate (1/lifetime) and

relative intensity of the long-lived o-Ps component (the effect of gas exposure or adsorption on o-Ps annihilating in the framework will be presented elsewhere). Figure A.2 shows this decay rate for He and H_2 gases at 296 and 77 K as a function of gas density measured in amagat (1 amagat corresponds to the number density of Avogadro's number of molecules in the STP molar volume, 1.08 bar at 296 K). At densities >0.1 amagat the decay rate is consistent with that of o-Ps in pure gas (curves in Figure A.2). These decay rates extrapolate to nominally the vacuum o-Ps value, 0.007 ns^{-1} (1/142 ns). Were o-Ps annihilating in gas-filled, 6 nm lattice defects the gas dependent decay rates would extrapolate to 1/80 ns. The decay rates above 0.1 amagat are completely consistent with o-Ps annihilating in the very large intergranular volume while undergoing temperature (T) independent pick-off annihilation with the specific gas. However, the question remains: what is happening below 0.1 amagat?

The unexpected rise in the fitted o-Ps decay rate at the very lowest gas densities is expanded in the bottom graph of Figure A.2. After scaling the H_2 density by a multiplicative factor of 2.5 *for both temperatures*, the H_2 results then agree with the He results (to be discussed). Furthermore, if we scale the two 77 K curves by a factor of 3.3 ($\sim T$, not shown in figure) then all four curves would merge to a universal result. This unusual gas and temperature dependence can be explained by assuming that nominally thermalized o-Ps within the MCP grain diffuses to and escapes from the grain receiving an energy boost of E_0 so its total energy outside the grain is $E_0 + k_B T$ (E_0, on the scale of a zero point energy, might be 0.1-0.3 eV[30,31]). Unhindered, such o-Ps would travel 20–30 mm making ~100 grain collisions and occasionally reenter a grain where annihilation occurs with higher rate corresponding to the 13 ns lifetime deep within the IRMOF-1 framework. The observed 80 ns o-Ps lifetime is then a time-weighted average of o-Ps subject to annihilation both inside (13 ns) and outside a grain (142 ns). The role of the gas is simply to degrade the o-Ps energy by an amount $k_B T$ or more to below the E_0 *threshold* for grain reentry leaving o-Ps trapped in the intergranular space. We assume the energy lost per collision with a gas molecule of mass M_g is $\sim(m/M_g)E_0$ where m is the o-Ps mass, and hence the energy loss rate in a gas of density n_g is

$$\frac{dE}{dt} = \frac{m}{Mg} E_0 n_g \sigma_g v_0,$$

where σ_g is the collision cross section for o-Ps with the particular gas molecule and v_0 is the o-Ps velocity corresponding to E_0. To eliminate grain reentry after some time t (10 ns, the time we begin fitting the spectrum) we require the gas density to be high enough so that $(dE/dt)t \approx k_B T$ and therefore the required density, n_g^*, to decrease the fitted decay rate to that in the pure gas depends on temperature and gas as $n_g^* \sim (M_g/\sigma_g)T$. This linear dependence on T is evident in Figure A.2 (right), the 77 K results scaled by 3.3 (close to $296/77 = 3.8$) merge with the 296 K results. The factor of 2.5 scaling in density of the H_2 data indicates

$$\frac{M_{He}}{\sigma_{He}} = 2.5 \frac{M_{H_2}}{\sigma_{H_2}},$$

and, after accounting for the masses, we conclude $\sigma_{H_2} = 1.25\ \sigma_{He}$ at energy E_0. Based on direct cross section measurements[32] at energies >5 eV this ratio is plausible. Indeed, given the difficulty in measuring o-Ps collision cross sections at sub-eV energies[33] it might be useful to use this new MCP-based method for accurately determining *relative o-Ps momentum transfer cross sections* for different gases.

The long-lived component in the PALS spectrum is thus the result of o-Ps escaping from the MCP grains and sometimes reentering them if there is no buffer gas to slow down the o-Ps. As a lower limit on the fraction of o-Ps escaping from the grains, F_{esc}, we can simply use the fitted relative o-Ps intensity of this long-lived component which ranges in IRMOF-1 from ~16% at 296 K to 28% at 77 K (in vacuum). Assuming o-Ps is formed uniformly throughout a cubic particle of side length L the fractional volume within diffusion length ℓ of a surface is $F_{esc} \sim 6\ell/L$. F_{esc} of 16% and 28% correspond to $\ell = 8\text{-}14$ μm for particles with $L = 300$ μm. It is straightforward to calculate the diffusion constant $D = (l^2/\tau)$ since $\tau = 13.5$ ns. Thus, $D(77\text{ K}) \sim 150$ cm^2/s and $D(296$ K$) \sim 50$ cm^2/s. Such large values for l and D in concert with longer diffusion at lower temperature are not consistent with classical diffusion. The argument for quantum

diffusion in a Bloch state is compelling if we deduce the mean free path for o-Ps scattering with the lattice, $\mathcal{L}$, and compare with the value of 1.5 nm determined from IRMOF-1 structure. Since $D = v\mathcal{L}/3$ we can deduce $\mathcal{L}$ if the average o-Ps diffusion velocity, v, is known. If we make the unsubstantiated assumption that o-Ps is thermalized then we deduce $\mathcal{L}(77\ K) = 1100$ nm and $\mathcal{L}(296\ K) = 190$ nm. Even if v is 10 times higher (unphysical o-Ps energy of 1-4 eV) $\mathcal{L}$ is still 1-2 orders of magnitude larger than 1.5 nm.

To test this assertion of very long mean free paths for lattice scattering we again use He gas as an inert source of o-Ps scattering *within* the MCP framework to variably impede o-Ps diffusion and promote o-Ps thermalization. We consider F_{esc} vs gas number density, n_{He}, at 77 and 296 K. Actually, we have plotted in Figure A.3 F_{esc} vs $n_{He}\sigma_{He}$ where we have assumed a reasonable value[33] (within a factor of 2) for $\sigma_{He} = 0.07$ nm^2 in order to provide an absolute length scale ($1/n_{He}\sigma_{He}$ is the mean free path for o-Ps between gas collisions). We can fit most of the data in Figure A.3 if we assume $\mathcal{L}$ depends only on temperature, v is constant over the fitted gas density range, and gas collisions shorten the total o-Ps mean free path such that

$$F_{esc} \sim \frac{6l}{L} = \frac{6}{L}\sqrt{\frac{v\tau/3}{\frac{1}{\mathcal{L}} + n_{He}\sigma_{He}}}.$$

We exclude data below 0.001 nm^{-1} which correspond to the low density (<0.1 amagat) results shown in Figure A.2 that involve grain reentry (not a simple diffusion model). The fitted values of $\mathcal{L}$ are 200 ± 25 nm at 296 K and 425 ± 50 nm at 77 K. The important point here is that $\mathcal{L}(T)$ is primarily determined by the gas scattering dependence (the shape of the curve) and not the absolute normalization term of $\sqrt{v\tau/3}$. We do find that this fitted velocity term is the same for 77 and 296 K which suggests that o-Ps is only able to approach room temperature thermalization in the lattice. The agreement of this value of $\mathcal{L}(296\ K)$ with the earlier value of 190 nm assuming thermal velocity supports this claim. Depending on our choice of σ_{He} these values could change by a factor of 2, but the inescapable fact is that the mean free path for scattering by lattice *imperfections* is 2 orders of magnitude larger than the 1.3 nm cell size of IRMOF-1. This unhindered

propagation due to the coherent constructive interference of the scattered waves by a perfect lattice is a hallmark of Bloch states.

The temperature dependence of o-Ps escaping from the grains, F_{esc}, is shown for IRMOF-1 and IRMOF-8 in Figure A.4. The o-Ps lattice mean free path $\mathcal{L}$ should be the combined result of temperature dependent phonon scattering ($\mathcal{L}_{ph}$) and temperature independent defect scattering ($\mathcal{L}_{def}$);

$$\frac{1}{\mathcal{L}(T)} = \frac{1}{\mathcal{L}_{ph}(T)} + \frac{1}{\mathcal{L}_{def}}.$$

Assuming the phonon density n_{ph} will increases $\sim$ linearly with T (the high temperature limit of the Bose-Einstein phonon distribution) the o-Ps-phonon scattering mean free path $\mathcal{L}_{ph} = 1/n_{ph}\sigma_{ph} \sim 1/T$. The curves shown in the figure are fits with this model that ignores any temperature dependence in the velocity term in F_{esc} (no o-Ps thermalization). This increase in the already long mean free path of o-Ps at low temperatures further illustrates the similarity with metallic electrical conductivity governed by phonon or defect scattering of Bloch electrons.

A.4   Conclusions

By way of temperature dependent gas exposure measurements in two MCPs we have shown that $D \sim 100$ cm^2/s and the deduced mean free paths for o-Ps scattering with lattice phonons and defects are hundreds of nanometers. On the other hand, o-Ps annihilation determined by wave function overlap is perfectly consistent with the lattice scale lengths of $\sim$1.5 nm. The simplest conclusion is that o-Ps is in a Bloch state manifested by a mean free path for scattering limited only by lattice imperfections. This is the first unambiguous experimental evidence of the existence of o-Ps in a Bloch state, the study of which is enabled by the recent availability of controllable nanometer lattice constant crystals and is simplified by the minimal complexity of bulk lifetime techniques. Bloch state o-Ps annihilation will be influenced significantly by the degree of crystalline imperfection of synthesized due to o-Ps diffusing and (not) thermalizing in the

framework (fitted lifetime and intensity reduced by escape from the grain) and *o*-Ps moving amongst and reentering the grains (the lifetime and intensity of the long-lived *o*-Ps component). Further understanding of Bloch state *o*-Ps may enable the use of PALS to quantify local defects that reduce (but do not eliminate) guest diffusion in MCPs.

Contributions to fundamental physics may also be enabled by the discoveries enumerated in this appendix. It would be interesting to perform angular correlation measurements on *p*-Ps annihilating in MCPs to determine if the distinctive umklapp phonon peaks can be resolved.[34] Velocity spectroscopy[30] of the *o*-Ps emitted from the grains of varying IRMOF samples could check the lattice size dependence of the emission energy E_0. Relative *o*-Ps-gas collision cross sections for E_0 in the sub-eV range could help constrain divergent absolute measurements.[33] Further experiments on *o*-Ps Bloch state scattering from gases in the framework are also warranted to examine the applicability of plane wave cross sections determined in the pure gas. Finally, we need to improve our understanding of how this delocalized state of *o*-Ps is probing this important new class of MCP crystals.
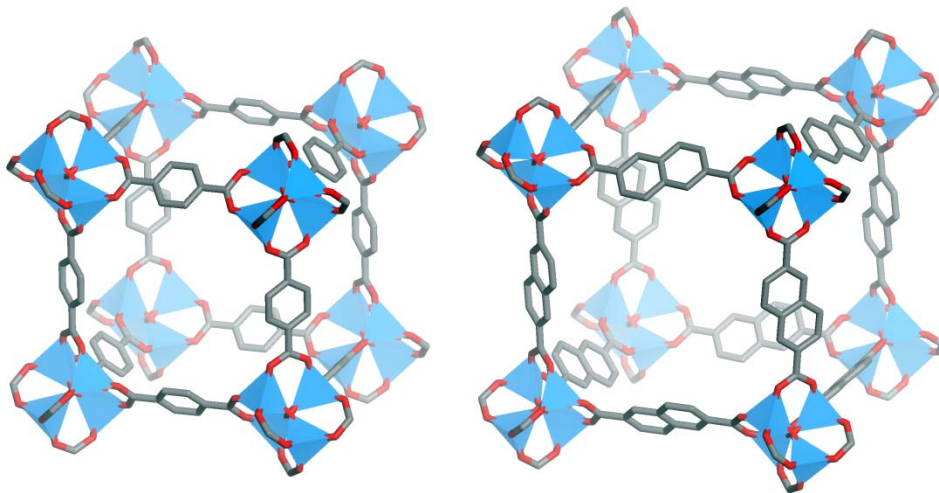
A.5   Figures

Figure A.1. Models of IRMOF-1 (left) and IRMOF-8 (right). Zn, blue tetrahedra; O, red; C, gray. H atoms omitted for clarity. The center-to-center distances of the closest Zn_4O clusters are 1.292 nm and 1.505 nm for IRMOF-1 and IRMOF-8, respectively.
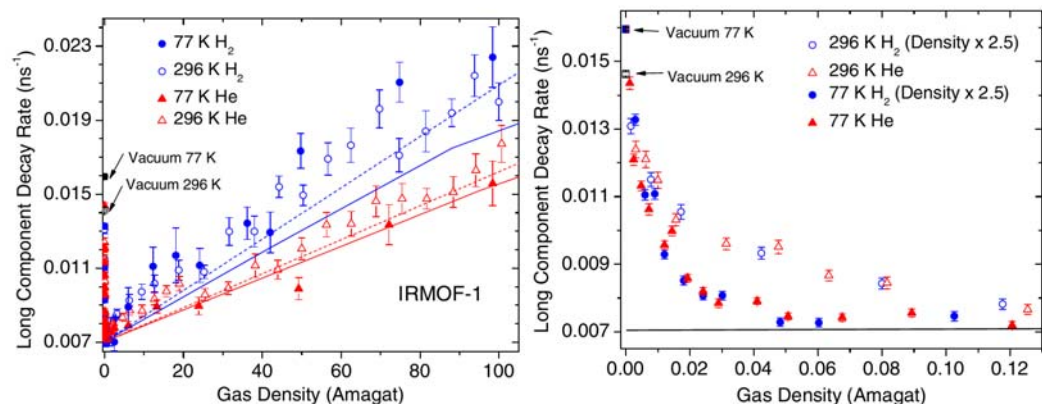
Figure A.2. (Left) Long-lived component decay rate in IRMOF-1 for He and H_2 gas at 77 and 296 K. The solid and dashed curves are the o-Ps decay rates measured in the respective pure gases at 77 and 296 K. The 77 K data continue the same trend to 400 amagat. The unusual drop in the decay rate to that in the pure gases (solid line) at the lowest 0.1% of density are expanded in the lower graph. Both sets of H_2 data have been scaled by a multiplicative factor of 2.5 in density to account for its faster energy loss per collision than He.
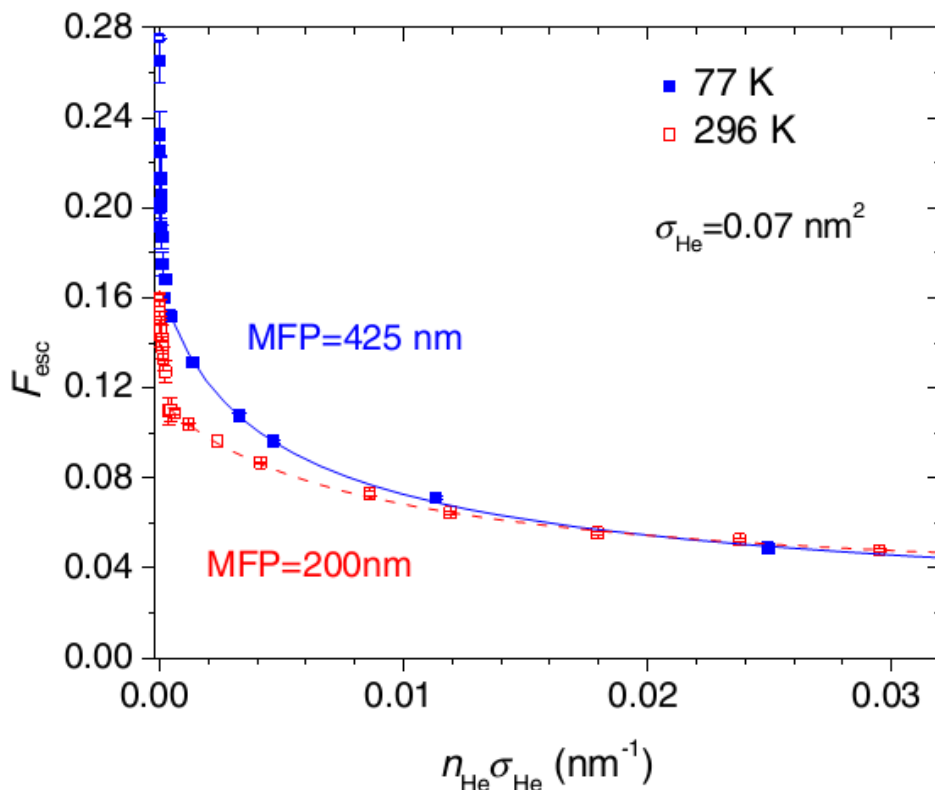

Figure A.3. The fraction of Ps escaping the IRMOF-1 grain vs gas density (multiplied by a nominal value for the Ps-He cross section, $\sigma_{He} = 0.07$ nm^2). The smooth curves are fits to a simple diffusion model that incorporates the variable gas scattering mean free path, $1/n_{He}\sigma_{He}$, with a temperature dependent mean free path for scattering with the lattice. Points on the far left are excluded from fitting as discussed in text.
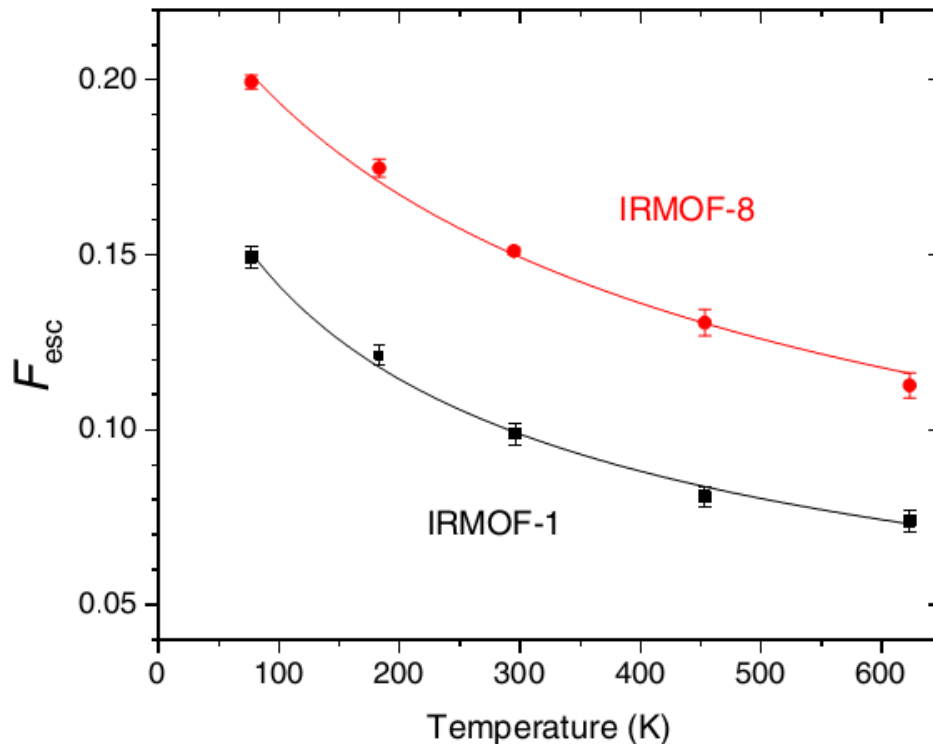
Figure A.4. The temperature dependence of Ps escaping evacuated IRMOF-1 and IRMOF-8 grains. For IRMOF-8 F_{esc} has been divided by a factor of 2.3 = 300 µm / 130 µm to account for its enhanced escape from smaller 130 µm grains. The smooth curves are fits to a diffusion model with a Ps-phonon mean free path that varies as $1/T$ and with a Ps-defect mean free path that is constant.

A.6   References

(1)   Schultz, P. J.; Lynn, K. G. *Reviews of Modern Physics* 1988, *60*, 701.

(2)   Jean, Y. C. *Microchem. J.* 1990, *42*, 72.

(3)   Brandt, W.; Coussot, G.; Paulin, R. *Phys. Rev. Lett.* 1969, *23*, 522.

(4)   Greenberger, A.; Mills, A. P.; Thompson, A.; Berko, S. *Phys. Lett. A* 1970, *32*, 72.

(5)   Inoue, K.; Suzuki, N.; Bondarev, I. V.; Hyodo, T. *Phys. Rev. B* 2007, *76*, 024304.

(6)   Barbiellini, B.; Platzman, P. M. *physica status solidi (c)* 2009, *6*, 2523.

(7)   Kadono, R.; Higemoto, W.; Nagamine, K.; Pratt, F. L. *Phys. Rev. Lett.* 1999, *83*, 987.

(8)   Hoskins, B. F.; Robson, R. *J. Am. Chem. Soc.* 1989, *111*, 5962.

(9)   Férey, G. *Chem. Soc. Rev.* 2008, *37*, 191.

(10)   Liu, M.; Wong-Foy, A. G.; Vallery, R. S.; Frieze, W. E.; Schnobrich, J. K.; Gidley, D. W.; Matzger, A. J. *Adv. Mater.* 2010, *22*, 1598.

(11)   Farha, O. K.; Eryazici, I.; Jeong, N. C.; Hauser, B. G.; Wilmer, C. E.; Sarjeant, A. A.; Snurr, R. Q.; Nguyen, S. T.; Yazaydın, A. Ö.; Hupp, J. T. *J. Am. Chem. Soc.* 2012, *134*, 15016.

(12)   Koh, K.; Wong-Foy, A. G.; Matzger, A. J. *J. Am. Chem. Soc.* 2009, *131*, 4184.

(13)   Yuan, D.; Zhao, D.; Sun, D.; Zhou, H.-C. *Angew. Chem., Int. Ed.* 2010, *49*, 5357.

(14)   Furukawa, H.; Ko, N.; Go, Y. B.; Aratani, N.; Choi, S. B.; Choi, E.; Yazaydin, A. Ö.; Snurr, R. Q.; O'Keeffe, M.; Kim, J.; Yaghi, O. M. *Science* 2010, *329*, 424.

(15)   Sumida, K.; Rogow, D. L.; Mason, J. A.; McDonald, T. M.; Bloch, E. D.; Herm, Z. R.; Bae, T.-H.; Long, J. R. *Chem. Rev.* 2012, *112*, 724.

(16)   Prasad, T. K.; Suh, M. P. *Chem.–Eur. J.* 2012, *18*, 8673.

(17)   Suh, M. P.; Park, H. J.; Prasad, T. K.; Lim, D.-W. *Chem. Rev.* 2012, *112*, 782.

(18)   Li, J.-R.; Sculley, J.; Zhou, H.-C. *Chem. Rev.* 2011, *112*, 869.

(19)   Lee, J.; Farha, O. K.; Roberts, J.; Scheidt, K. A.; Nguyen, S. T.; Hupp, J. T. *Chem. Soc. Rev.* 2009, *38*, 1450.

(20)   Feldblyum, J. I.; Liu, M.; Gidley, D. W.; Matzger, A. J. *J. Am. Chem. Soc.* 2011, *133*, 18257.

(21)   Tao, S. J. *J. Chem. Phys.* 1972, *56*, 5499.

(22)   Eldrup, M.; Lightbody, D.; Sherwood, J. N. *Chem. Phys.* 1981, *63*, 51.

(23)   Dull, T. L.; Frieze, W. E.; Gidley, D. W.; Sun, J. N.; Yee, A. F. *J. Phys. Chem. B* 2001, *105*, 4657.

(24)   Jasińska, B.; Dawidowicz, A. L.; Goworek, T.; Wawryszczuk, J. *Opt. Appl.* 2003, *33*, 7.

(25)   Eddaoudi, M.; Kim, J.; Rosi, N.; Vodak, D.; Wachter, J.; O'Keeffe, M.; Yaghi, O. M. *Science* 2002, *295*, 469.

(26)   Ito, K.; Kobayashi, Y. *Mater. Sci. Forum* 2004, *445-446*, 307.

(27)   Eldrup, M.; Vehanen, A.; Schultz, P. J.; Lynn, K. G. *Phys. Rev. B* 1985, *32*, 7048.

(28)   Van Petegem, S.; Dauwe, C.; Van Hoecke, T.; De Baerdemaeker, J.; Segers, D. *Phys. Rev. B* 2004, *70*, 115410.

(29)   Wu, Y. C.; Jiang, J.; Wang, S. J.; Kallis, A.; Coleman, P. G. *Phys. Rev. B* 2011, *84*, 064123.

(30)   Mariazzi, S.; Bettotti, P.; Brusa, R. S. *Phys. Rev. Lett.* 2010, *104*, 243401.

(31)   Cassidy, D. B.; Crivelli, P.; Hisakado, T. H.; Liszkay, L.; Meligne, V. E.; Perez, P.; Tom, H. W. K.; Mills, A. P., Jr. *Phys. Rev. A* 2010, *81*, 012715.

(32)   Brawley, S. J.; Armitage, S.; Beale, J.; Leslie, D. E.; Williams, A. I.; Laricchia, G. *Science* 2010, *330*, 789.

(33)   Skalsey, M.; Engbrecht, J. J.; Nakamura, C. M.; Vallery, R. S.; Gidley, D. W. *Phys. Rev. A* 2003, *67*, 022504.

(34)   Nagai, Y.; Kakimoto, M.; Hyodo, T.; Fujiwara, K.; Ikari, H.; Eldrup, M.; Stewart, A. T. *Phys. Rev. B* 2000, *62*, 5531.